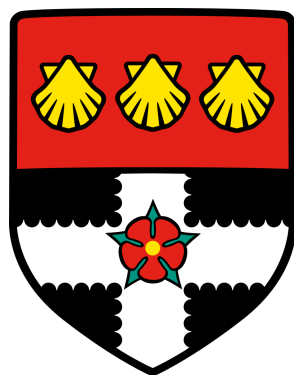


UNIVERSITY OF READING

Department of Meteorology



**Linking Weather Forecast Errors
with the Physical Processes
Responsible**

Leo Saffin

A thesis submitted for the degree of Doctor of Philosophy

May 2017

Declaration

I confirm that this is my own work and the use of all material from other sources has been properly and fully acknowledged.

Leo Saffin

Abstract

Progress in numerical weather prediction (NWP) is made through better understanding of the physical processes represented in numerical models and their impacts on the dynamics of large-scale weather systems. Here, potential vorticity (PV) tracer diagnostics are used to investigate the representation of processes in the Met Office Unified Model (MetUM).

An exact budget of the PV tracers is derived and a “dynamics-tracer inconsistency” diagnostic implemented to quantify non-conservation of PV by the dynamical core which was not previously accounted for. It is shown that non-conservation of PV by the dynamical core can have comparable tendencies to the dominant physical processes implying that non-conservation of PV by a dynamical core can, and should, be quantified alongside PV modification by physical processes.

Recent work has shown that the sharpness of the extratropical tropopause declines with lead time in NWP models. In the MetUM, the advection scheme is shown to result in an exponential decay of tropopause sharpness and non-conservative processes are shown to sharpen the tropopause. The systematic errors in tropopause-level PV are comparable to the tendencies associated with physical processes, suggesting that the systematic error in tropopause sharpness could be significantly reduced through realistic adjustments to the model physics.

Turbulent mixing within the boundary layer has been previously shown to produce positive PV anomalies that can be advected into cyclones and reduce growth rates through an increase in static stability; however, it is unclear whether NWP models correctly represent this mechanism. In the MetUM, the generation of these positive PV anomalies is found to be less clear due to large cancellations with other physical processes in the cold sector. Front-relative compositing is used to separate the cold and warm sectors, providing the basis for investigating PV generation in the boundary layer systematically by compositing over many fronts.

Acknowledgements

I would like to thank my supervisors, John Methven, Sue Gray and Keith Williams, for all their support throughout this project. Thank you to my committee members, Remi Tailleux and Michaela Hegglin, for keeping me on track and motivated every six months. Also thank you to, Jeff Chagnon, Oscar Martínez-Alvarado, Claudio Sanchez and Ben Harvey, the research staff who have helped out with my work over the course of my PhD (usually the PV tracers).

Thanks to all the people in the Met department I have got to know over the past few years. Thanks to the fellow boardgamers on Lyle 3, Jon, James and Chris, for providing a welcome distraction every lunchtime. Obviously, thanks to Donald X. Vaccarino for creating Dominion. Finally, thank you to Hannah for buying me dominion . . . and generally being awesome.

Thanks guys. Thuys

Acronyms and Notation

Acronyms

Acronym	Full Name
PV	Potential Vorticity
PVU	Potential Vorticity Units
MetUM	Met Office Unified Model
NAE	North Atlantic and European (MetUM limited-area domain configuration)
NWP	Numerical Weather Prediction
DIAMET	Diabatic Influences on Mesoscale Structures in Extratropical Storms (project)
IOP	Intensive Observing Period
TIL	Tropopause Inversion Layer
WCB	Warm Conveyor Belt

Meteorological variables

Notation	Description
q	Potential vorticity
θ	Potential temperature
θ_e	Equivalent potential temperature
$\mathbf{u} = (u, v, w)$	3D wind vector
ρ	Density
λ, ϕ	Latitude and longitude

MetUM notation

Notation	Description
θ -level	Model levels where θ and w are stored in the MetUM's hybrid-height coordinates following the Charney-Phillips staggering
\mathbf{X}	The set of prognostic variables in the MetUM
$\mathbf{X}^{(j)}$	The set of prognostic variables after step j within a single timestep of the MetUM following the predictor-corrector method
$\mathbf{X}^{(sl)}$	The set of prognostic variables after the semi-Lagrangian dynamics step in the MetUM
d	A subscript “ d ” denotes evaluation at departure points in the MetUM’s semi-Lagrangian scheme
mic	Microphysics
sw	Short-wave radiation
lw	Long-wave radiation
con	Convection
tm	Turbulent mixing
$cloud$	Cloud balancing
sl	Semi-Lagrangian dynamics
$solver$	Pressure solver
sp, fp	“Slow physics” ($mic/sw/lw/gwd$) and “Fast physics” ($conv/bl$). Two groups of physics parametrizations in the MetUM

PV tracers

Notation	Description
q_{adv}	Advection-only PV tracer
q_i	PV tracer for physical process i (<i>mic/sw/lw/gwd/conv/bl/cloud</i>)
Δq_i	Increment in PV due to a physical (<i>mic/sw/lw/gwd/conv/bl/cloud</i>) or dynamical (<i>sl/solver</i>) process i within a single timestep
$\sum q_{phys}$	The sum of physics PV tracers
ε	PV not previously accounted for by the PV tracers
ε_I	Dynamics-tracer inconsistency
ε_r	Residual PV

Diagnostics

Notation	Description
$q=2$	2-PVU surface of PV
$q_{adv}=2$	2-PVU surface of the advection-only PV tracer
ϕ_e	Equivalent latitude
θ_b	Background state θ on 2 PVU
θ'	θ anomaly from the background state
Δq_{adv}	Contrast in q_{adv} across a 2-PVU surface

Contents

1	Introduction	1
1.1	Thesis Overview	1
1.2	The Governing Equations	3
1.3	Potential Vorticity	6
1.3.1	Conservation	6
1.3.2	Impermeability Theorem	7
1.3.3	Balance	9
1.4	Mid-Latitude Weather	13
1.4.1	Rossby Waves	13
1.4.2	Baroclinic Waves	16
1.4.3	Extratropical Cyclones	19
1.4.4	Air Streams	21
1.4.5	Diabatic Processes	23
1.5	Numerical Weather Prediction	30
1.5.1	Predictability	30
1.5.2	Model Errors	32
2	Methods	37
2.1	Met Office Unified Model	37
2.1.1	Grid	37
2.1.2	Parametrisation Schemes	38
2.1.3	Formulation of the Unified Model	46
2.2	PV Tracers	49
2.2.1	Method	49
2.2.2	Formulation in the MetUM	49
2.3	Case Studies	52
2.3.1	IOP5	52
2.3.2	IOP8	55
2.4	Winter Season	58
3	Dynamics-tracer Inconsistency	63
3.1	Introduction	63
3.2	Results	64

3.2.1	PV Budget	65
3.2.2	Dynamics-tracer Inconsistency	68
3.2.3	Non-conservation of PV by the Dynamical Core	69
3.2.4	Tropopause Dipole	73
3.3	Conclusions	75
4	Processes Maintaining Tropopause Sharpness	79
4.1	Introduction	79
4.2	Processes Affecting Tropopause Sharpness	80
4.3	Objective Definition of Ridges and Troughs	82
4.4	Results	85
4.4.1	Tropopause-Relative Composites	85
4.4.2	Tropopause PV Contrast	89
4.4.3	Tracer Advection	89
4.4.4	Dynamics-tracer Inconsistency	92
4.4.5	Parametrized Physical Processes	94
4.5	Conclusions	97
5	Potential Vorticity Structure Near Lower Tropospheric Air Mass Boundaries	103
5.1	Introduction	103
5.2	Ground-relative Composites	104
5.3	The Boundary Layer	108
5.4	Fronts	117
5.5	Conclusions	123
6	Conclusions	129
6.1	Conclusions	129
6.2	Future work	133
Bibliography		134

Chapter 1

Introduction

1.1 Thesis Overview

Weather and climate prediction is achieved by integrating numerical models of the atmosphere. Over the past 40 years, weather forecast skill has continuously improved due to increasing computing power, better understanding of atmospheric processes and higher quality and coverage of observations ([Bauer *et al.*, 2015](#)). The increased computing power allows for more resources to be allocated to model resolution, representation of physical processes and deriving the initial model state. There is no such thing as a perfect model of the atmosphere; however, there is room for improvement. [Bauer *et al.* \(2015\)](#) identified improvement in the parametrization of physical processes as one of the key areas contributing to increased skill in numerical weather prediction but also as a key area for further improvements. For climate modelling, [Bony *et al.* \(2015\)](#) identified the parametrization of cloud processes and convection, as well as their impacts on the large-scale circulation, as a key area for future research.

The scientific contribution to improving numerical models of the atmosphere can be thought of as a continuous iteration of the question: **what changes should be made to a numerical model to reduce systematic forecast errors?** This is the overarching question being asked in this thesis. The first step to answering this question is to identify and characterise forecast errors. The next step is to trace these forecast errors back to the processes responsible and understand how these processes result in systematic forecast errors. One way to answer this question is through diagnostics that can isolate and quantify the effects of the various processes represented within a numerical model of the atmosphere.

In this thesis, potential vorticity (PV) tracers, based on the method of [Davis *et al.* \(1993\)](#), are used to diagnose the effects of different processes within a numerical model. The properties of PV, described in further detail in section [1.3](#), suggest a PV-based

diagnostic of model errors would be insightful. The conservation of PV following air masses ([Ertel, 1942](#)) makes PV a useful tracer diagnostic that can isolate the effects of different physical processes. The invertibility principle of PV ([Hoskins *et al.*, 1985](#)) allows for diagnosed PV changes to be linked with theoretical understanding of atmospheric dynamics: many aspects of the large-scale dynamics of the atmosphere can be understood in terms of the PV distribution. With a suitable balance approximation it is possible to infer the changes in wind and temperature associated with changes in PV.

The research contained in this thesis is split into three chapters (chapters 3-5) that can be summarized as addressing a set of science questions.

1. What are the sources of PV non-conservation in numerical models?

For the PV tracers to be used to link forecast errors with the processes responsible they must accurately quantify the sources of PV non-conservation. In chapter [3](#) the budget of PV described by the PV tracers is assessed. It is shown that there is a large residual in the PV tracers. An exact budget of the PV tracers is used to derive and implement a “dynamics-tracer inconsistency” diagnostic and is shown to account for the majority of the residual. The sources of dynamics-tracer inconsistency and importance within a numerical model are discussed. The content of this chapter is taken from [Saffin *et al.* \(2016\)](#).

2. Why does tropopause sharpness reduce with forecast lead time?

A shortcoming of current numerical weather prediction models is that the sharpness of the midlatitude tropopause declines with forecast lead time ([Gray *et al.*, 2014](#)). The reduction in tropopause sharpness rapidly saturates within the first few days of forecasts ([Gray *et al.*, 2014](#)) and will result in a systematic bias in the representation of teleconnections within the atmosphere ([Harvey *et al.*, 2016](#)). A poor representation of teleconnections will subsequently hinder the usefulness of numerical models on longer timescales ([Palmer *et al.*, 2008](#)).

Since the tropopause can be described as an air-mass boundary between high-PV and low-PV air ([Reed, 1955](#)) and the sharpness of the tropopause can be measured by the PV gradient (e.g. [Gray *et al.* \(2014\)](#)), PV tracers will be a useful method for quantifying the effects of different processes on the tropopause. Using the PV tracers, [Chagnon *et al.* \(2013\)](#) showed that parametrized physical processes acted to sharpen the tropopause. In chapter [4](#) the systematic effects of different processes on the tropopause, over many

forecasts, are quantified. The dominant mechanisms affecting the tropopause sharpness, and potential causes of model error, are then discussed. The content of the chapter is taken from [Saffin *et al.* \(2017\)](#).

3. What are the systematic effects of parametrized physical processes across other air-mass boundaries?

In chapter [4](#), by producing composites relative to the air-mass boundary of the tropopause, the effects of different processes acting in dynamically distinct regions could be diagnosed. In chapter [5](#), the effects of different processes across air-mass boundaries in the lower atmosphere, the boundary-layer top and fronts, are investigated.

Chapter [6](#) summarises the key conclusions related to the science questions. Open questions and future work related to this thesis are also discussed. In chapter [2](#) the main methods used in this thesis are described. The model used throughout this thesis is the Met Office’s unified model (MetUM) ([Davies *et al.*, 2005](#)) and is described. The PV tracers, which were applied to the MetUM by [Gray \(2006\)](#), are also defined. The forecasts run with the MetUM with online integration of the PV tracers are also introduced.

The rest of this chapter covers the scientific background for the thesis. Section [1.2](#) describes the governing equations of the atmosphere. Section [1.3](#) describes the important principles of PV. Section [1.4](#) describes features of midlatitude weather starting at large scales with Rossby waves, to synoptic scales of baroclinic cyclones and features embedded in cyclones and finally small-scale frictional and diabatic processes. The basics of numerical weather prediction are introduced in section [1.5](#) with a focus on forecast errors.

1.2 The Governing Equations

This section outlines the governing equations for the atmosphere, the set of equations that are solved by the dynamical cores of atmospheric models. This set of equations can also be considered the starting point for producing simplified equations by including further approximations. The starting approximations are that the atmosphere is an ideal gas forming a layer of fluid surrounding the rotating, and approximately spherical, Earth.

Newton’s second law tells us that the rate of change of momentum of an object is equal to the sum of external forces acting on that object. When applied to a parcel of

fluid in a rotating reference frame it gives the momentum equation,

$$\frac{D\mathbf{u}}{Dt} = -2\boldsymbol{\Omega} \times \mathbf{u} - \mathbf{g} - \frac{1}{\rho} \nabla p + \mathbf{F}, \quad (1.1)$$

where $\mathbf{u} = (u, v, w)$ is the three dimensional wind vector (momentum per unit mass). The derivative of the wind tells us we are following an air parcel (Lagrangian form) this can be related to the partial derivative at a fixed location (Eulerian form) as $\frac{D}{Dt} = \frac{\partial}{\partial t} + \mathbf{u} \cdot \nabla$. The terms on the right hand side give the various forces acting on the fluid parcel. The first term ($-2\boldsymbol{\Omega} \times \mathbf{u}$, where $\boldsymbol{\Omega}$ is Earth's rotation vector) is the Coriolis force related to the acceleration in a rotating reference frame. The second term ($-\mathbf{g}$) is the effective gravity and is a combination of the Earth's gravitational acceleration and the centrifugal force. The third term ($-\frac{1}{\rho} \nabla p$) is the pressure gradient force, where p is pressure and ρ is density. The last term (\mathbf{F}) is a generic vector representing frictional forces which can be further broken down. This includes external friction, such as the interaction between the atmosphere and the Earth's surface, and internal friction associated with fluid viscosity.

The internal friction can be represented as $\nu \nabla^2 \mathbf{u}$, where ν is the kinematic viscosity. The internal friction is a result of the molecular viscosity, a macroscopic property of the fluid due to the microscopic fluid constituents. If the air parcels are considered at a certain scale then unresolved fluid motions are also often represented in terms of an “eddy viscosity” which has the same mathematical form but a much larger coefficient of viscosity.

It is important to consider the governing equations in spherical polar coordinates (longitude (λ), latitude (ϕ) and radius from the Earth centre (r)) which separates out important forces for each direction of motion. If the Earth is assumed to be a spheroid the effective gravity can be replaced by a constant that only appears in the vertical component of the momentum equation. If the atmosphere is assumed to be shallow relative to the Earth radius then the Coriolis force, appearing in the momentum equation, can be simplified to just the vertical component, $-f\hat{\mathbf{k}} \times \mathbf{u}$, where $f = 2\Omega \sin(\phi)$ is the Coriolis parameter. The omission of the horizontal component of the Coriolis force when the atmosphere is shallow is required when eliminating metric terms associated with the spherical coordinates to retain key conservation principles (White *et al.*, 2005). This set of approximations result in what is referred to as the “shallow-atmosphere equations” as opposed to the “deep-atmosphere equations” when these approximations are not included.

The mass continuity equation,

$$\frac{\partial \rho}{\partial t} + \nabla \cdot (\rho \mathbf{u}) = 0, \quad (1.2)$$

tells us that the changes in mass per unit volume must equal the sum of mass fluxes into and out of the volume. The equation can also be written in Lagrangian form, giving

$$\frac{1}{\rho} \frac{D\rho}{Dt} = -\nabla \cdot \mathbf{u}, \quad (1.3)$$

which tells us that the changes in density following a fluid parcel are due to divergence and convergence of winds.

The other aspect to the governing behaviour of the atmosphere is the thermodynamics. The equation of state for the dry atmosphere is given by the ideal gas equation,

$$p = \rho RT, \quad (1.4)$$

where R is the specific gas constant for dry air and T is the temperature. The evolution of the thermodynamics is best described by the potential temperature,

$$\theta = T \left(\frac{p_0}{p} \right)^{\frac{R}{c_p}}, \quad (1.5)$$

where c_p is the heat capacity at constant pressure and p_0 is a reference pressure value (typically 1000 hPa corresponding to a typical surface pressure). The potential temperature is the temperature an air parcel would have if brought adiabatically to the reference pressure. The evolution of potential temperature is then given by the thermodynamic equation,

$$\frac{D\theta}{Dt} = \frac{\theta}{c_p T} Q, \quad (1.6)$$

where Q is the diabatic heating rate per unit mass. The definition and evolution of potential temperature emphasises a conceptual separation between diabatic and adiabatic processes: the adiabatic changes in temperature are related to changes in pressure of the air parcels. The diabatic processes can, like friction, be considered separate from the basic fluid dynamics; heat transfers due to the effects of radiation and chemical reactions occur because the fluid consists of atoms and molecules. The separation of adiabatic and diabatic processes can be incorporated in to the coordinate system by using isentropic coordinates (constant θ) where adiabatic motions are purely horizontal and the vertical velocity is a result of diabatic heating.

1.3 Potential Vorticity

Potential vorticity (PV) is a useful variable in dynamical meteorology. In this section some of the key motivations for PV and thinking in terms of PV are described. In the absence of diabatic heating and friction, PV is advected like a tracer ([Ertel, 1942](#)). In the presence of diabatic heating and friction, the impermeability theorem of [Haynes and McIntyre \(1987\)](#) and [Haynes and McIntyre \(1990\)](#) describes how PV behaves differently to a passive tracer and gives an alternative view for interpreting PV budgets. The PV distribution provides a complete description of the dynamics when a balance approximation can be used to determine the winds, temperature and density through PV inversion (the invertibility principle ([Hoskins *et al.*, 1985](#))). Conceptually, a balance model is stepped forward in time by advecting the PV field like a tracer given the diagnosed winds and then inverting the updated PV distribution to diagnose the wind field and so on. The invertibility principle provides the theoretical backing for describing features in terms of PV ([Hoskins *et al.*, 1985](#)).

1.3.1 Conservation

The conservation of PV can be shown to be a combination of the dynamics, thermodynamics and mass conservation described by the governing equations ([Ertel, 1942](#)). The PV derived by [Ertel \(1942\)](#) is a generalisation of the PV derived by [Rossby \(1940\)](#). There are multiple ways of deriving the conservation of PV (e.g. [Vallis \(2006\)](#)), in this section the conservation of PV will be described in terms of Kelvin's circulation theorem. The first step is to describe the evolution of vorticity by taking the curl of Eq. 1.1 which gives the vorticity equation,

$$\frac{D\zeta}{Dt} = \frac{\nabla\rho \times \nabla p}{\rho^2} + (\zeta \cdot \nabla)\mathbf{u} - \zeta(\nabla \cdot \mathbf{u}) + \nabla \times \mathbf{F}, \quad (1.7)$$

where $\zeta = \xi + 2\Omega$ is the absolute vorticity vector which combines the relative vorticity (ξ) and the planetary vorticity from the Earth's rotation (2Ω). The terms in the vorticity equation can be understood in terms of circulation changes. The circulation around a closed loop is defined by,

$$C_a = \oint \mathbf{u}_a \cdot d\mathbf{r} = \int_S \zeta \cdot d\mathbf{S}, \quad (1.8)$$

where the a subscript denotes the absolute (non-rotating) reference frame. Combining Eqs. 1.1 and 1.7 with the definition of circulation gives Kelvin's circulation theorem,

$$\frac{DC_a}{Dt} = - \oint \left(\frac{1}{\rho} \nabla p + \mathbf{F} \right) \cdot d\mathbf{r} = \int_S \left(\frac{\nabla \rho \times \nabla p}{\rho^2} + \nabla \times \mathbf{F} \right) \cdot d\mathbf{S}. \quad (1.9)$$

The Coriolis term has been eliminated because we are considering the absolute circulation. Vortex tilting ($(\zeta \cdot \nabla) \mathbf{u}$) and vortex stretching ($\zeta(\nabla \cdot \mathbf{u})$) both modify the vorticity while conserving the circulation. The solenoidal term ($\frac{\nabla \rho \times \nabla p}{\rho^2}$) is due to the pressure gradient force not cancelling out around a circuit. For isentropic circulation the solenoidal term can be eliminated, because $\theta = \theta(\rho, p)$, by setting $d\mathbf{S} = \mathbf{n} \cdot \delta A$ where $\mathbf{n} = \frac{\nabla \theta}{|\nabla \theta|}$ is the unit vector normal to the isentropic surface and δA is the area element. Considering an air parcel bounded by two isentropic surfaces gives

$$\mathbf{n} \delta A = \frac{1}{\rho} \frac{\delta M}{\delta \theta} \nabla \theta, \quad (1.10)$$

because $\delta A = \frac{\delta V}{\delta h}$, $\delta h = \frac{\delta \theta}{|\nabla \theta|}$ and $\delta M = \rho \delta V$ (see Fig. 4.9 in [Vallis \(2006\)](#)). This gives

$$\frac{D}{Dt} \left(\frac{\delta M}{\rho \delta \theta} \zeta \cdot \nabla \theta \right) = \frac{\delta M}{\rho \delta \theta} (\nabla \times \mathbf{F}) \cdot \nabla \theta. \quad (1.11)$$

Since mass is conserved following an air parcel, the term δM can be eliminated. For adiabatic motion, the term $\delta \theta$ can also be eliminated which shows that PV,

$$q = \frac{1}{\rho} \zeta \cdot \nabla \theta, \quad (1.12)$$

is conserved following adiabatic ($\dot{\theta}=0$) and frictionless ($\mathbf{F}=0$) flow (i.e. $\frac{Dq}{Dt} = 0$). Retaining the $\delta \theta$ term and separating out the Lagrangian tendency of PV gives

$$\frac{Dq}{Dt} = \frac{1}{\rho} \left(\zeta \cdot \nabla \dot{\theta} + \nabla \theta \cdot \nabla \times \mathbf{F} \right), \quad (1.13)$$

which quantifies how the PV of an air parcel is modified by diabatic and frictional processes.

1.3.2 Impermeability Theorem

The conservation of PV following an air mass allows us to consider PV as an air mass tracer to the extent that the motion is adiabatic and frictionless. The impermeability theorem arises from considering the Eulerian form of PV evolution with diabatic and frictional processes included and has important implications for the evolution of PV and

considerations of PV as tracer (Haynes and McIntyre, 1987, 1990). Haynes and McIntyre (1987) showed that the evolution of PV could be expressed as

$$\frac{\partial(\rho q)}{\partial t} + \nabla \cdot (\rho q \mathbf{u} - \dot{\theta} \boldsymbol{\zeta} - \mathbf{F} \times \nabla \theta) = 0. \quad (1.14)$$

The important conclusion from Eq. 1.14 is that the changes in mass-weighted PV can be written as the divergence of a flux, which is equivalent to stating that there are no net sources or sinks of PV. This can be seen by comparing Eq. 1.14 to the equivalent form for a trace substance with mass mixing ratio χ ,

$$\frac{\partial(\rho \chi)}{\partial t} + \nabla \cdot (\rho \chi \mathbf{u} + \mathbf{J}_\chi) = \rho S_\chi, \quad (1.15)$$

where $\rho \chi \mathbf{u}$ is the advective flux of the tracer, \mathbf{J}_χ is a non-advective flux term and S_χ is a source/sink term. In this analogy, PV is equivalent to the mass mixing ratio of a tracer (“PV substance” (Haynes and McIntyre, 1987)). In the absence of diabatic heating and friction the PV fluxes are purely advective with the diabatic heating and frictional processes acting as non-advective fluxes. Importantly there is no source/sink term to the PV; it is misleading to describe the material tendencies of PV due to diabatic and frictional processes as sources and sinks although it may appear to be a reasonable description from the Lagrangian form of the PV equation (Eq. 1.13) (Haynes and McIntyre, 1990).

In isentropic coordinates Eq. 1.14 can be expressed as,

$$\frac{\partial(\rho q)}{\partial t} + \nabla \cdot (\rho q \mathbf{v}) + \nabla \cdot \mathbf{J}, \quad (1.16)$$

where $\mathbf{v} = (u, v, 0)$ is the isentropic wind and $\mathbf{J} = (J_x, J_y, 0)$ is the non-advective fluxes in isentropic coordinates (Haynes and McIntyre, 1987). The key conclusion is that there is no cross-isentropic flux of PV substance even in the presence of non-conservative processes: there can be no net transport of PV across isentropic surfaces (Haynes and McIntyre, 1987). In the analogy of PV as a tracer, the isentropic surfaces act as membranes permeable to mass but impermeable to PV substance. The material changes in PV are described as result of mass fluxes across isentropes resulting in dilution/concentration of PV substance.

The response of a stationary, stratified atmosphere to a region of diabatic heating can illustrate the way the different perspectives arrive at consistent conclusions. A local increase of θ means a lowering of the isentropic surface above; $\frac{\partial \theta}{\partial z}$ has increased below the heating and decreased above which results in a dipole of PV anomalies with a negative

PV anomaly above the heating and a positive PV anomaly below. This is immediately obvious from the Lagrangian evolution of PV (Eq. 1.13) where the tendency of PV is proportional to the gradient in diabatic heating. From the perspective of the PV impermeability theorem, a localised region of latent heating will cause a mass flux across an isentrope. Since the isentrope is impermeable to PV substance there will be a dilution of PV substance above the isentrope and concentration of PV substance below the isentrope which gives the equivalent result of a dipole in PV anomalies.

1.3.3 Balance

The concept of balanced flow is key to the PV perspective; the invertibility principle of PV, as described by [Hoskins *et al.* \(1985\)](#), states that the distribution of PV and boundary conditions are sufficient to infer the balanced flow. The ideas of balanced conditions originally stemmed from the need to suppress unrealistic inertia-gravity waves from being generated in numerical models of the atmosphere ([Charney, 1955](#)) and balanced models are considered to be equations which filter out the fast motions from inertia-gravity and sound waves ([McIntyre and Norton, 2000](#)).

The simplest balances in the atmosphere can be derived by considering the dominant terms in the momentum equations. Neglecting the accelerations of air parcels as well as frictional forces the vertical momentum equation gives hydrostatic balance,

$$\frac{\partial p}{\partial z} = -\rho g, \quad (1.17)$$

where the gravitational pull of the Earth on the atmosphere is balanced by vertical pressure gradients. If an air parcel is adiabatically displaced in the vertical from a background state in hydrostatic balance then it will oscillate with the Brunt-Väisälä frequency,

$$N = \sqrt{\frac{g}{\theta} \frac{d\theta}{dz}}. \quad (1.18)$$

This wave solution has two modes: for $N^2 > 0$ ($\frac{d\theta}{dz} > 0$) the growth rate is imaginary and results in an oscillation; for $N^2 < 0$ ($\frac{d\theta}{dz} < 0$) the growth rate is real and results in an exponential increase as the air parcel is accelerated due to being increasingly more buoyant relative to its surroundings (increasingly less buoyant if the initial displacement is downwards). The latter is a simple example of instability and adjustment to a balanced state. The atmosphere will rapidly rearrange itself to a stably stratified state which is essential to using θ as a vertical coordinate.

Neglecting local accelerations of air parcels and frictional forces in the horizontal momentum equations gives geostrophic balance,

$$f\mathbf{k} \times \mathbf{v}_g = -\frac{1}{\rho} \nabla_h p, \quad (1.19)$$

where the pressure gradient force balances the Coriolis force giving a balanced geostrophic wind (\mathbf{v}_g). If the atmosphere is described in terms of perturbations to a reference state that only varies vertically (anelastic approximation) then the hydrostatic and geostrophic balances can be described in terms of a geostrophic streamfunction,

$$\psi_g = \frac{p'}{\rho_r f_0}, \quad (1.20)$$

where p' is the pressure perturbation to the reference state, ρ_r is the reference profile for density and f_0 is constant Coriolis parameter. Geostrophic balance becomes

$$\mathbf{v}_g = -\hat{\mathbf{k}} \times \nabla \psi_g, \quad (1.21)$$

and hydrostatic balance becomes,

$$f_0 \frac{\partial \psi_g}{\partial z} = b', \quad (1.22)$$

where $b' = g \frac{\theta'}{\theta_r}$ is a buoyancy anomaly, with θ_r and θ' denoting the reference profile of θ and the anomaly field respectively. The combination of hydrostatic and geostrophic balances gives the thermal wind balance relation,

$$f_0 \frac{\partial \mathbf{v}_g}{\partial z} = \mathbf{k} \times \nabla b'. \quad (1.23)$$

The simplest balances are equivalent to the zeroth order asymptotic expansions, in small Froude number ($\text{Fr} = \frac{U}{NH}$) for stratified flow and in small Rossby number ($\text{Ro} = \frac{U}{fL}$) for rapidly rotating flow (Vallis, 1996). A well known balance model is the quasi-geostrophic equations which have been used to explain large-scale flow patterns in the midlatitudes (e.g. Charney and Stern (1962)). The quasi-geostrophic equations can be considered as a first order expansion in Rossby number (Vallis, 1996). Expanding the velocity in terms of Rossby number the velocity is considered as the combination of the zeroth-order geostrophic wind (\mathbf{v}_g) and the first order ageostrophic wind (\mathbf{v}_a), with higher orders neglected, such that

$$\mathbf{v} = \mathbf{v}_g + \mathbf{v}_a, \quad (1.24)$$

and

$$\mathbf{v}_a \propto \text{Ro} \cdot \mathbf{v}_g. \quad (1.25)$$

The quasi-geostrophic equations can be described by the conservation of quasi-geostrophic PV following the geostrophic flow,

$$\frac{D_g q_g}{Dt} = 0, \quad (1.26)$$

where $\frac{D_g}{Dt} = \frac{\partial}{\partial t} + \mathbf{v}_g \cdot \nabla_h$ is advection by the geostrophic wind and the quasi-geostrophic PV is given by,

$$q_g = f + \nabla_h^2 \psi_g + \frac{1}{\rho_r} \frac{\partial}{\partial z} \left(\rho_r \frac{f^2}{N^2} \frac{\partial \psi_g}{\partial z} \right), \quad (1.27)$$

The quasi-geostrophic PV equation (Eq. 1.27) gives a linear relation between the PV and the geostrophic streamfunction which is the basis of the invertibility principle (Hoskins *et al.*, 1985); equation. 1.27 can be inverted to determine the geostrophic streamfunction, and hence the geostrophic winds, given the distribution of q_g , specification of the reference profile (ρ_r) and boundary conditions. This can be seen by writing Eq. 1.27 as $q = f + \mathcal{L}(\psi_g)$ where \mathcal{L} represents a linear elliptic operator. The equation is then inverted ($\psi_g = \mathcal{L}^{-1}(q - f)$) so that the streamfunction can be determined from the PV distribution. The linearity of Eq. 1.27 means the PV field can be separated into multiple PV anomalies and parts of the full flow can be attributed to the individual PV anomalies unambiguously (Bishop and Thorpe, 1994). This way we can view individual anomalies of PV as inducing a certain amount of rotation and stratification; Figure. 1.1 shows the rotation and stratification associated with an isolated PV anomaly.

When inverting PV, the boundary conditions can have large impacts on the solution. The boundary conditions are θ anomalies (Bretherton, 1966b) which act like PV anomalies exterior to the boundaries (Bishop and Thorpe, 1994). At the ground θ anomalies act like PV anomalies of the same sign whereas at upper boundaries, such as a rigid tropopause, θ anomalies act like PV anomalies of the opposite sign. This can be seen by considering the displacement of isentropes by θ anomalies: at the ground a positive θ anomaly means the isentropes bend towards the anomaly and there is an associated balanced flow response which can be reproduced by placing a boundary above the positive PV anomaly in Fig. 1.1; for the tropopause a negative θ anomaly means the isentropes bend towards the anomaly which can be reproduced by placing the boundary below the positive PV anomaly in Fig. 1.1.

The accuracy of PV inversion can be improved by using more accurate balance relations and extending quasi-geostrophic PV thinking to the full PV (Thorpe and Bishop,

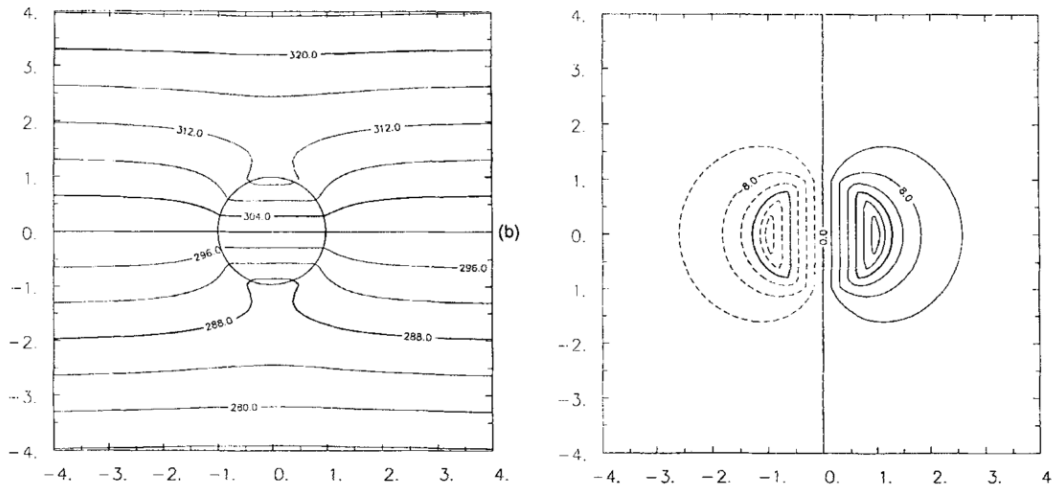


Figure 1.1: Figure 1b from Thorpe and Bishop (1995). A vertical cross section showing the stratification and rotation induced by an isolated quasi-geostrophic PV anomaly with magnitude $\frac{q'}{f_0} = 4$. The left panel shows θ (contour interval 4 K) and the right panel shows normal velocity (contour interval 4 m s⁻¹). The distances are relative to the radius of the PV anomaly with the vertical using a stretched coordinate.

1995). Davis and Emanuel (1991) introduced a PV inversion method using the nonlinear balance equations of Charney (1955) that separated individual anomalies of PV and attributed separate flow patterns to each anomaly (piecewise PV inversion). The accuracy of piecewise PV inversion is improved by using the more accurate balance equations at the expense of ambiguity in attribution of the flow to individual PV anomalies due to the nonlinearity of the balance relation used (Davis and Emanuel, 1991). Spatial separation of PV anomalies reduces the ambiguity in the attribution due to a decreasing importance of the nonlinear interaction of PV anomalies in the inversion operator with increasing spatial separation (Birkett and Thorpe, 1997).

The combination of eqs. 1.26 and 1.27 gives a prognostic model based on the assumptions of quasi-geostrophy. PV is advected then inverted to obtain the balanced flow at the next timestep so that the evolution is entirely determined by the PV and its associated balanced winds. As with the diagnostic PV inversion the prognostic balance models can be extended to higher orders. McIntyre and Norton (2000) tested the ultimate limits of the accuracy of balanced flow by comparing a hierarchy of PV-based balanced models of increasing accuracy with the full primitive equations for shallow water flow initialised with low gravity-wave activity. McIntyre and Norton (2000) showed that the accuracy of

the higher order balanced models compared to the primitive equation run was “remarkably” close with the highest order models being nearly indistinguishable at 15 days lead time. This suggests that the dynamical information encoded only in the PV distribution is very close to the true dynamics of the system. [McIntyre and Norton \(2000\)](#) showed that, although these PV-based models were very accurate, none of them conserved mass locally. They conjectured that the lack of local mass conservation is a necessary trade-off to obtain the high accuracy. [Mohebalhojeh and McIntyre \(2007\)](#) showed that this was not the case and constructed PV-based balanced models that could conserve mass explicitly without a compromise in accuracy. Although this did not always improve the accuracy, it demonstrated that no trade off with important conservation principles was required for accurate PV inversions.

1.4 Mid-Latitude Weather

This section describes the important features of midlatitude weather starting at the largest scale and moving to increasingly smaller scales with increasing detail and complexity. At the large scale the midlatitude dynamics are dominated by Rossby-waves on a westerley jet. Coupling of Rossby waves in the vertical leads to baroclinic instability/waves. Consideration of the nonlinear evolution of baroclinic waves leads to distinctive life cycles and Rossby wave breaking. The individual cyclones in baroclinic life cycles are associated with the majority of clouds, precipitation and strong winds. The evolution of cyclones can be better understood by considering the important air streams within cyclones. At the smallest scale diabatic and frictional processes can have important impacts by systematically modifying larger-scale weather.

1.4.1 Rossby Waves

In the midlatitudes the dominant features of the planetary scale can be described by Rossby waves ([Rossby, 1940](#)). The variation in the Coriolis force with latitude is key to the features of Rossby waves. The simplest description of a latitudinally varying Coriolis force is achieved by taking the first two terms in a Taylor expansion of the Coriolis parameter ($f = 2\Omega \sin(\phi)$) about a reference latitude ϕ_0 which gives the β -plane approximation,

$$f \approx 2\Omega \sin(\phi_0) + \frac{2\Omega \cos(\phi_0)}{r}y = f_0 + \beta y. \quad (1.28)$$

The single layer dynamics of Rossby waves can be described by applying the quasi-geostrophic approximation to the shallow-water equations (Vallis, 2006). The shallow-water approximation integrates the 3-dimensional equations over a small vertical layer and is applicable when vertical scales of motion are much smaller than horizontal scales. Considering adiabatic motions conserve θ , this single layer evolution can be considered as an approximation to the evolution of PV in isentropic layers. In this case the dynamics are described by the evolution of the quasi-geostrophic shallow-water PV (q_{qgsw}),

$$\frac{Dq_{qgsw}}{Dt} = \frac{D(\nabla^2\psi + \beta y - 1/L_R^2)}{Dt} = 0, \quad (1.29)$$

where $L_R = \sqrt{gH}/f_0$ is the Rossby radius of deformation. Note that, compared to Eq. 1.27, the constant planetary rotation (f_0) has been eliminated because it is a constant that can be subtracted without affecting the conservation. The PV can be considered as a combination of a background planetary PV ($q_{qgsw,b} = \beta y$) and a perturbation PV ($q'_{qgsw} = \nabla^2\psi - 1/L_R^2$).

Equation. 1.29 contains all the dynamics required for the Rossby wave mechanism. Conceptually this can be seen in Fig. 1.2 in terms of vortex interactions. If we take Fig. 1.2 to depict a θ surface with initially zero perturbation PV everywhere then the PV linearly increases with y following the β plane approximation. In this simple model if an air parcel is displaced equatorward its perturbation PV will increase because PV is conserved and the parcel therefore has higher PV than the surrounding fluid. The PV anomaly will induce a cyclonic circulation around this displaced air parcel resulting in a poleward displacement of air to the east and an equatorward displacement of air to the west. The opposite happens for a poleward displacement and we see the westward propagating pattern of positive and negative PV anomalies depicted in Fig. 1.2.

The properties of the Rossby waves can be derived from Eq. 1.29 (e.g. Vallis (2006)). Starting from a background state with a uniform zonal flow with speed (U) and applying a small perturbation to the streamfunction and linearising Eq. 1.29 gives wave-like solutions with phase velocity,

$$\frac{\omega}{k} = U - \frac{\beta + U/L_R^2}{k^2 + l^2 + 1/L_R^2}, \quad (1.30)$$

and group velocity,

$$\frac{\partial\omega}{\partial k} = U + \frac{(\beta + U/L_R^2)(k^2 - l^2 - 1/L_R^2)}{(k^2 + l^2 + 1/L_R^2)^2}, \quad (1.31)$$

where ω is frequency and k and l are the zonal and meridional wavenumbers. A key feature

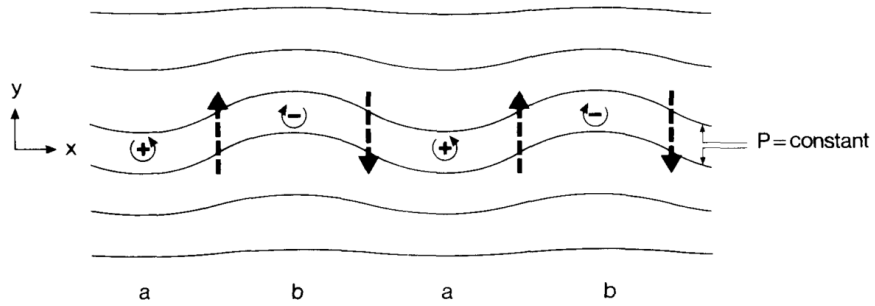


Figure 1.2: Figure 17 from [Hoskins et al. \(1985\)](#) showing a conceptual picture of a Rossby wave on an isentrope. Contours are of constant PV showing a background equator-to-pole PV gradient. The + and - signs indicate the cyclonic and anticyclonic PV anomalies respectively and the dashed arrows indicate the induced velocities which cause a westward propagation of the wave pattern.

of Rossby waves is that relative to the background flow Rossby waves have a westward phase velocity (Eq. 1.30) and an eastward group velocity (Eq. 1.31 for $k^2 > l^2 + 1/L_d^2$). This means that, in the midlatitudes, Rossby waves propagate information upstream and Rossby wave packets propagate information downstream. In the limit of balanced flow, Rossby waves provide the only form of upstream and downstream development: Rossby waves are an important source of teleconnections for large-scale dynamics (e.g. [Hoskins and Ambrizzi \(1993\)](#)).

Figure 1.2 depicts Rossby waves on a smooth equator to pole PV gradient; however, the gradient of PV in the atmosphere is usually focused in a narrow band associated with a sharp distinction between the stratosphere and troposphere at the tropopause. Since the tropopause coincides with a sharp gradient of PV a single value of PV between $1.5 - 5$ PVU ($\text{PVU} = 10^{-6} \text{ m}^2 \text{K} \text{ Kg} \text{ s}^{-1}$) can be taken to represent the “dynamical” tropopause ([Reed, 1955](#); [Hoskins et al., 1985](#)). The sharp gradient of PV, which coincides with localised jet streams, acts as a waveguide for Rossby waves ([Hoskins and Ambrizzi, 1993](#)). Since PV is conserved for adiabatic and frictionless flow the dynamical tropopause can be thought of as a material surface and stratosphere-troposphere exchange is achieved by diabatic processes and small-scale mixing (e.g. [Lamarque and Hess \(1994\)](#)). Maps of θ on the tropopause can give a useful overview of the large-scale dynamics because they indicate the location of the tropopause on each isentrope that intersects the tropopause ([Hoskins and Berrisford, 1988](#); [Nielsen-Gammon, 2001](#)).

1.4.2 Baroclinic Waves

The interaction of Rossby waves on different vertical levels leads to baroclinic instability ([Hoskins *et al.*, 1985](#)). A useful simple model of baroclinic instability which allows for analytic solutions of the stability criteria and growth rates is the Eady model ([Eady, 1949](#)). The Eady model describes the linear growth of small perturbations on an initially balanced state. The simplified model used by [Eady \(1949\)](#) has a similar set of assumptions to the quasi-geostrophic equation set with additional constraints on the background flow. The atmosphere is considered to have rigid upper and lower boundaries corresponding to the tropopause and the ground. The background wind is a zonally constant jet that increases with height ($u = u_0 + \Lambda z$), consistent with a pole to equator temperature gradient by thermal-wind balance. The static stability, Coriolis parameter and density are also assumed to be constant. The solutions to the Eady model are a set of growing normal modes. The modes are unstable for long waves with a “short-wave cut off” beyond which the modes do not grow. The fastest growing mode has been used as an explanation for the typical size and growth rate of extratropical cyclones. The growth rate of the fastest growing mode is found to be $\sigma = 0.31 \frac{f}{N} \frac{\partial u}{\partial z}$ and can be used as a diagnostic of baroclinic instability.

The background state of the Eady model has no internal PV gradient and the perturbations can be described by two boundary Rossby waves: one at the ground and one on the rigid-lid tropopause ([Hoskins *et al.*, 1985](#)). The PV anomalies associated with the ridges and troughs of the two waves induce winds on the opposite boundary. The induced winds can act to phase-lock the Rossby waves resulting in mutual amplification of the wave structure.

Prior to the discovery of the Eady model a more complex setup that includes variations in the Coriolis force (β effect) and density but no tropopause was introduced by [Charney \(1947\)](#). The fastest growing mode for the Charney model is remarkably similar to the Eady model. The Charney model does not have a short-wave cut off because the β effect gives the interior of the domain a non-zero PV gradient and therefore the boundary Rossby waves can induce and amplify Rossby waves in the interior of the domain rather than requiring an influence on the opposite boundary ([Bretherton, 1966b](#)). The interpretation of the Eady and Charney model in terms of counter-propagating Rossby-waves has been successfully applied for general zonal flows ([Heifetz *et al.*, 2004a](#)) and used to interpret

Charney model solutions in [Heifetz et al. \(2004b\)](#).

As Rossby waves grow and propagate, the nonlinear evolution becomes more important, leading to Rossby wave breaking. It is common to see streamers and cut-off features of PV ([Appenzeller and Davies, 1992](#)). Numerical simulations have been used to extend the analytical solutions of early stage baroclinic instability of [Eady \(1949\)](#), The result is two distinct baroclinic life cycles resulting from modifying the initial background jet ([Thorncroft et al., 1993](#)). Figure. 1.3 shows a schematic of the two extreme cases of a baroclinic life cycle where the deformation of the tropopause is dominated by anticyclonic (LC1) or cyclonic (LC2) wrapping. [Methven et al. \(2005\)](#) showed that the nonlinear evolution of the baroclinic waves could still be described in terms of a pair of counter-propagating Rossby waves.

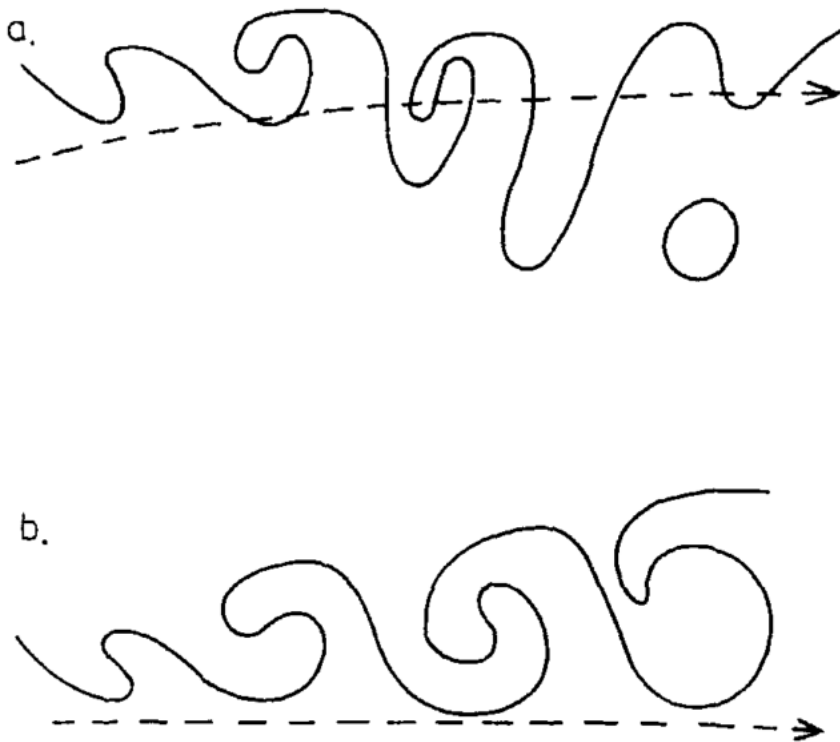


Figure 1.3: Figure 12 from [Thorncroft et al. \(1993\)](#) showing a schematic of a contour of PV on θ (or θ on the tropopause) for the (a) anticyclonic and (b) cyclonic life cycles. The dashed line indicates the typical mean position of the jet. The evolution from left to right is intended to be time evolution but can also be visualised as a zonal coordinate.

The breaking of Rossby waves in the atmosphere can often lead to flow configurations that oppose the midlatitude jet ([Pelly and Hoskins, 2003](#)). This is known as blocking and

can often be explained in terms of a “dipole block” where an anticyclone lies poleward of a cyclone with combined circulations in between the two vortices acting to block the jet ([Rex, 1950](#)). This blocking action can often be persistent and criteria for identifying blocking use persistence thresholds of 3-5 days to identify blocks ([Tibaldi and Molteni, 1990](#)). Figure. 1.4 shows the different types of block that can form: (a) and (b) show a classical wave breaking shape where (a) cyclonic or (b) anticyclonic wrapping results in a warm (cyclonic) anomaly poleward of a cold (anticyclonic) anomaly; (c) demonstrates how the blocking can also often look more like an amplified ridge with an Ω shape with the large amplitude warm (anticyclonic) anomaly having two cold (cyclonic) anomalies equatorward on its flanks ([Pelly and Hoskins, 2003](#)). Blocking results in stationary cyclones which can result in large accumulations of precipitation or persistent strong winds. The stationary anticyclones of the blocking can cause warm temperature extremes in summer due to a continuous radiative heating over the same region ([Pfahl and Wernli, 2012a](#)).

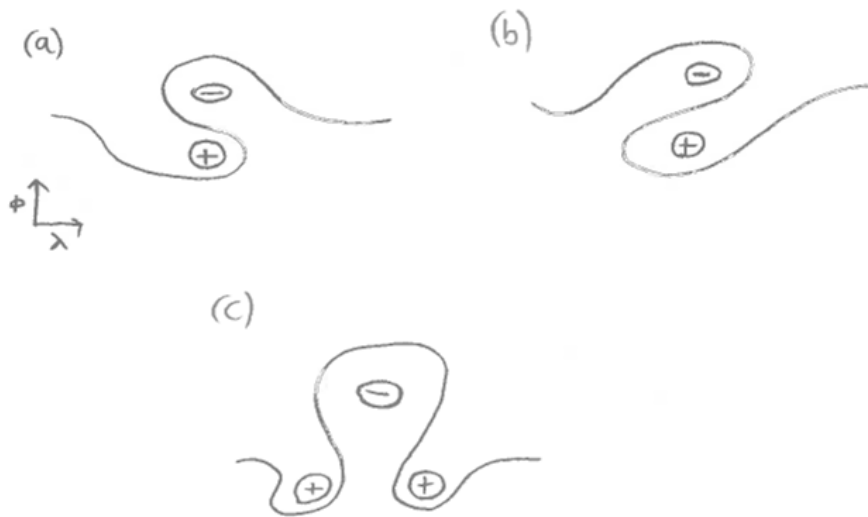


Figure 1.4: Schematic of different types of blocking. The solid contour indicates the intersection of a PV surface, representing the tropopause, with an isentropic surface. The signs of the associated PV anomalies are indicated.

1.4.3 Extratropical Cyclones

Extratropical cyclones are an important component of baroclinic waves. Extratropical cyclones are responsible for the majority of extreme wind and precipitation in the mid-latitudes ([Pfahl and Wernli, 2012b](#); [Hawcroft *et al.*, 2012](#)). Climatologically extratropical cyclones develop and propagate in distinct regions of the midlatitudes known as the storm tracks ([Hoskins and Hodges, 2002](#)). Figure 1.5 shows the Northern Hemisphere storm tracks, as measured by the track density of cyclonic features, and demonstrates the distinct concentration of storms in the North Atlantic and North Pacific.

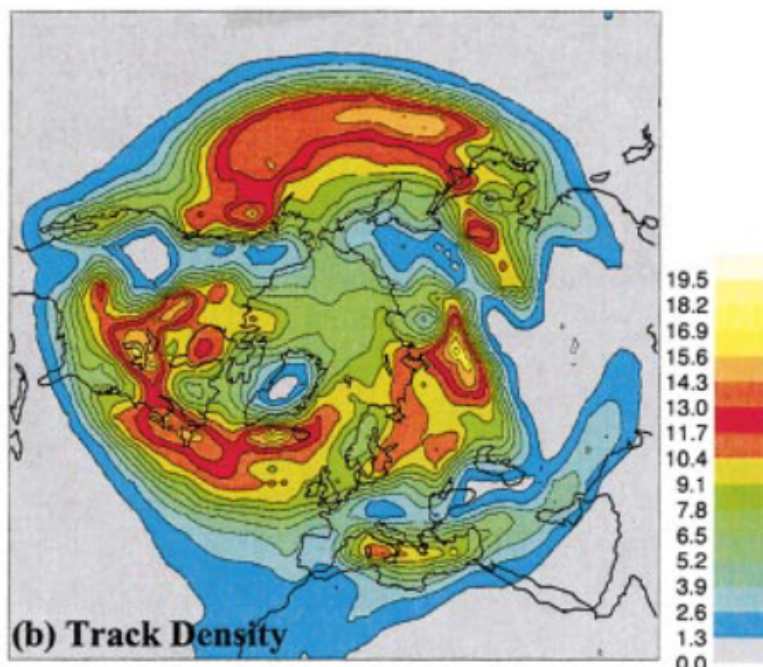


Figure 1.5: Density of tracks of extratropical cyclones identified as maxima in vorticity at 850 hPa from [Hoskins and Hodges \(2002\)](#). ©American Meteorological Society. Used with permission.

Conceptual models are useful for describing the life cycles of extratropical cyclones in terms of surface pressure charts. Considering geostrophic balance, cyclonic circulation is associated with a pressure minima and strong winds are associated with sharp pressure gradients so cyclones are often identified by surface pressure minima with the strength of the cyclone described by the depth of the minima (relative to the background pressure). The rate of at which a cyclone deepens is closely related to its maximum intensity ([Sanders and Gyakum, 1980](#)).

Figure. 1.6 shows the stages of a typical cyclone life cycle in terms of the surface evolution. The first conceptual model of extratropical cyclones, based on surface observations, described distinct air masses and the sharp boundaries (fronts) between those air masses (Bjerknes and Solberg, 1922). The starting point (0) is a front separating warm (tropical) air and cold (polar) air: whether the front is a cold front (triangles) or a warm front (semicircles) is defined by motion of the front relative to the ground. Fronts are inherently unstable and cyclogenesis can be triggered by interaction with existing PV anomalies (Joly and Thorpe, 1990; Schär and Davies, 1990). As the cyclone starts to circulate the front can be separated into a cold front to the west and warm front to the east (2). At the centre point of the two fronts the low pressure system develops with closed pressure contours and an associated cyclonic circulation (3). As the cyclone intensifies the cold front circulates faster than the warm front and the frontal structure wraps up around the cyclone (Schultz and Vaughan, 2010). For some rapidly developing cyclones the cold front is observed to “fracture” (4) with frontolysis in the centre of the cyclone leaving a “T-bone” structure ahead of the low pressure centre and a “bent-back front” wrapping around the low pressure centre (5) (Shapiro and Keyser, 1990). For more typical cyclones the cold front will undercut the warm front resulting in an occluded front wrapping around the cyclone (Schultz and Vaughan, 2010). As the cold front continues to advance the bent-back front wraps up in the cyclone centre creating a “warm-core seclusion” (6). As the frontal structure decays we are left with a cyclonic circulation around a low pressure centre that decays (7).

Cyclones also often occur in the absence of strong low-level potential temperature gradients where the upper-level forces the low-level cyclogenesis and this evolution can be described as a distinct type of cyclogenesis (Petterssen and Smebye, 1971). Type-A cyclones, which are the typical type of cyclones described above, are initially dominated by low-level forcing and type-B cyclones are initially dominated by upper-level forcing (Petterssen and Smebye, 1971). Type-B cyclogenesis can be seen in isentropic PV maps when an upper-level trough or cut-off triggers low-level cyclogenesis. There is also a third category, type-C cyclones (Deveson *et al.*, 2002; Plant *et al.*, 2003), described in section 1.4.5.

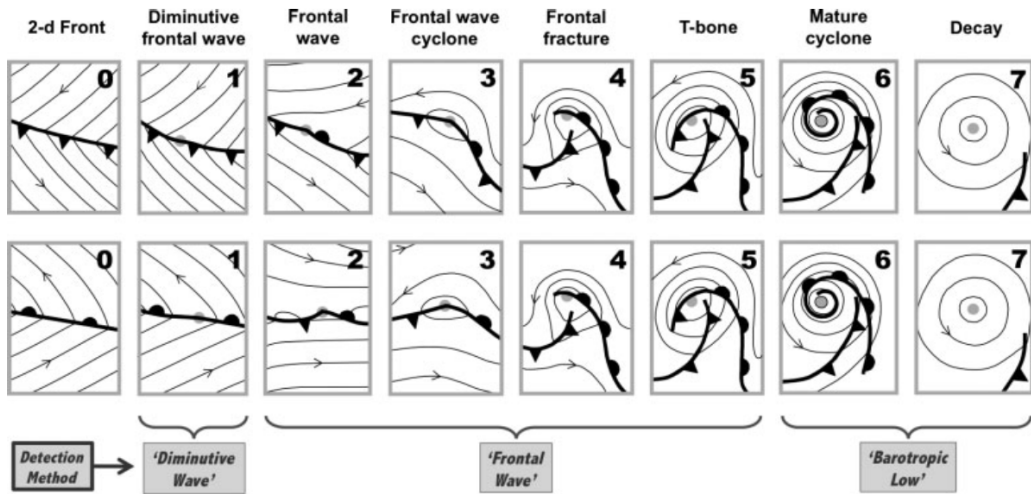


Figure 1.6: Figure 1 from [Hewson and Titley \(2010\)](#) depicting the phases of an idealised intense cyclone in surface pressure charts. Thin lines show isobars and thick lines show warm (semicircles) and cold (triangles) fronts. The top panels show a cyclone initiated on a cold front and the bottom panels show a cyclone initiated on a warm front. A detailed description of the various stages is given in the text.

1.4.4 Air Streams

A useful concept in understanding and analysing extratropical cyclones on a smaller scale is the idea of distinct airflows embedded within the cyclone. The original descriptions of air flows used isentropic relative flow analysis ([Green et al., 1966](#)) with observations; air parcels can be tracked by considering quantities that are approximately conserved following the flow. These large-scale air flows are associated with trajectories of air masses and can be considered as a coherent ensemble of trajectories where the trajectories of distinct airstreams remain close together for the life time of the cyclone ([Wernli and Davies, 1997](#)). [Hart et al. \(2015\)](#) demonstrated that identification of coherent airstreams can be achieved with an objective clustering method and that the resulting airstreams are consistent with subjectively identified airstreams.

Figure. 1.7, taken from [Martínez-Alvarado et al. \(2014b\)](#), shows a schematic of the important airstreams that have been identified in extratropical cyclones relative to a typical surface structure. The three major air streams are: the “warm conveyor belt” (WCB1 and WCB2 in Fig. 1.7), the “cold conveyor belt” (CCB in Fig. 1.7) and the “dry-intrusion” (DI in Fig. 1.7). Most of the clouds and precipitation within extratropical cyclones can

be associated with the two “conveyor belts” which are associated with sustained transports of moisture and ascent. From thermal-wind balance (Eq. 1.23) we know that the strongest wind shear tends to be 90° anticlockwise to the sharpest temperature gradients which explains the warm conveyor-belt on the warm side of the cold front and the cold conveyor belt on the warm side of the warm front.

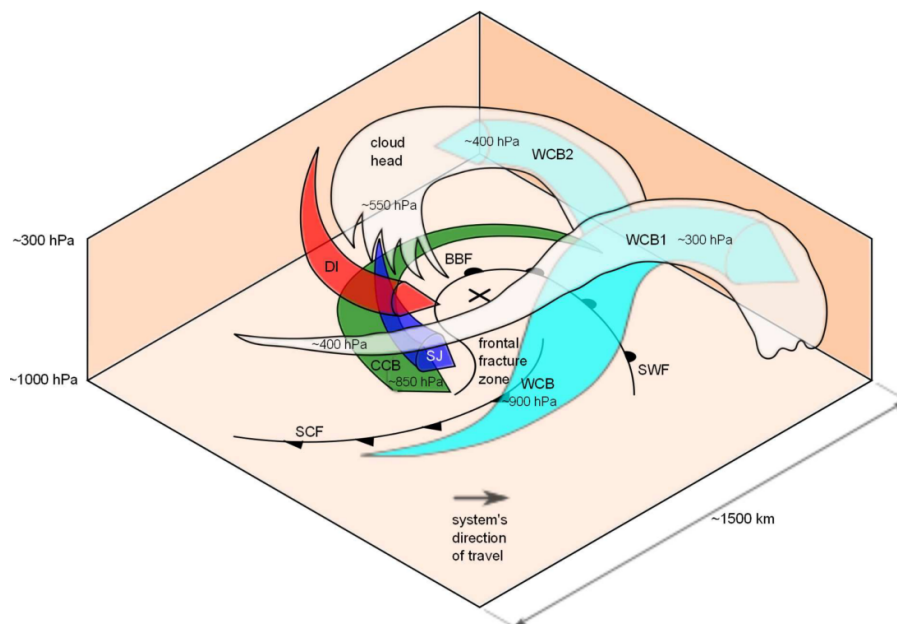


Figure 1.7: Figure 1 from Martínez-Alvarado *et al.* (2014a) depicting the important airstreams relative to a mature cyclone structure. SCF: surface cold front; SWF: surface warm front; BBF: bent-back front; CCB: cold conveyor belt; SJ: sting jet air stream; DI: dry intrusion; WCB: warm conveyor belt; WCB1: WCB anticyclonic branch; WCB2: WCB cyclonic branch; the large X represents the cyclone center at the surface and the gray shading represents cloud top. ©American Meteorological Society. Used with permission.

The warm conveyor belt is an ascending flow of air running parallel to the cold front towards, and ahead of, the cyclone centre (Harrold, 1973). The warm conveyor belt splits into two branches, one turning cyclonically (WCB2) and one anticyclonically (WCB1) (Harrold, 1973). Warm conveyor belts are associated with strong ascent; an ascent criterion of 600 hPa in 48 hours has been used to produce warm conveyor belt climatologies (Madonna *et al.*, 2014) and in their original identification using trajectories (Wernli and Davies, 1997). The strong ascent of warm conveyor belts means they can have important impacts on the upper-level flow, acting to amplify upper-level Rossby waves due to the

divergence of the outflow and the PV anomaly associated with the upward transport of air masses (Grams *et al.*, 2011). By transporting low-valued PV air upwards to areas that are climatologically stratospheric, the negative PV anomalies associated with warm conveyor belts have typical magnitudes of 1-3 PVU (Madonna *et al.*, 2014).

The cold conveyor belt is a low-level air stream that flows parallel to the warm front around the poleward side of the cyclone (Carlson, 1980). As the warm front wraps up into the cyclone the cold conveyor can also be associated with strong winds as the airflow direction matches the translation direction of the cyclone. This can be important for the wind impacts especially in the case of sting jets; the “sting jet” is a distinct airstream from the cold conveyor belt resulting from slantwise circulations descending out of the cloud head and can, in some cyclones, result in extreme surface winds by adding to the already strong winds associated with the cold conveyor belt (Browning, 2004).

The dry intrusion is a descending air stream consisting of dry upper-tropospheric air that is wrapped in to the cyclone centre (Young *et al.*, 1987; Raveh-Rubin, 2017). The combination of the cloud-free dry intrusion and the cloudy warm conveyor belt gives extratropical cyclones a distinctive “comma” cloud pattern in satellite images (Young *et al.*, 1987).

1.4.5 Diabatic Processes

1.4.5.1 Diagnostics

The simplest way to infer the effects of a process is to compare two simulations, one including the process and one excluding the process. Sensitivity tests alone often will not add any understanding of why the simulations are different and the combination of sensitivity tests with other diagnostics can be much more insightful (e.g. Davis *et al.* (1993)).

From Eq. 1.13 we know that diabatic and frictional processes can be described as modifications in PV. The PV perspective combined with the production of negative and positive PV anomalies by diabatic and frictional processes proves to be a powerful way of interpreting the dynamical impacts of those processes. The piecewise PV inversion method means we can invert individual PV anomalies to associate their effects on the balanced flow (Davis and Emanuel, 1991); combining piecewise PV inversion with a method

of associating a PV anomaly to a diabatic process allows us to consider the diabatically-induced balanced flow at a later time.

The attribution of a PV anomaly to diabatic forcing needs to consider the Lagrangian history of air parcels. The Lagrangian history of PV can be calculated from trajectories ([Wernli and Davies, 1997](#)) or can be calculated online in a numerical simulation using tracers that accumulate tendencies ([Davis *et al.*, 1993](#)). The advantage of trajectories is that they can be used with any sufficiently high resolution dataset. PV tracers have the advantages that the numerical model can provide a clear separation of different physical processes and the transport of tracers is more consistent with the dynamics of the numerical model than deriving trajectories from model output because information is used at each timestep.

Since cyclones are often considered by their surface pressure minima the relative contributions of different processes to the deepening of cyclones can be quantified by partitioning the pressure tendency of the cyclones. [Fink *et al.* \(2012\)](#) considered the vertically integrated tendencies in pressure of a column of air and split the tendencies among the following: advection of the upper boundary; mass changes by evaporation and precipitation; horizontal and vertical temperature advection; and the heating due to diabatic processes. [Fink *et al.* \(2012\)](#) demonstrated that diabatic processes are an important contribution to the deepening of intense extratropical cyclones and can be the dominant process in some cases.

1.4.5.2 Radiation

The pole to equator temperature gradient, a key ingredient to baroclinic instability ([Eady, 1949](#)), is a result of the distribution of incoming short-wave radiation from the sun. The storm tracks are the regions with a maximum in atmospheric poleward heat fluxes. This balance between baroclinicity generation and heat fluxes can be seen as a nonlinear oscillation between the diabatic processes building up the baroclinicity followed by cyclones forming from the large baroclinicity and eroding the baroclinicity ([Amabaum and Novak, 2014; Novak *et al.*, 2015](#)).

The maintainence of sharp PV gradient at the tropopause requires a diabatic process to maintain the stratospheric high PV reservoir and the tropospheric low PV ([Amabaum, 1997](#)). This process can be seen in the lifetime of individual cyclones as shown by the

dipole of diabatically-generated PV across the tropopause found by [Chagnon et al. \(2013\)](#) where positive PV generated in the stratosphere is brought to the stratospheric side of the tropopause and negative PV generated in the troposphere is brought to the tropospheric side of the tropopause with negligible exchange across the stratosphere. The tropopause is associated with a sharp decrease in water vapour from the troposphere to the stratosphere which results in a gradient in long-wave radiation ([Forster and Wirth, 2000](#)). The presence of clouds acts to focus the radiative cooling at the cloud top ([Cau et al., 2005](#)). The combination of the water vapour contrast and clouds reaching the tropopause means that the maintenance of the stratospheric and tropospheric PV reservoirs by long-wave radiation can be a localised sharpening of the tropopause ([Chagnon et al., 2013](#)).

1.4.5.3 Latent Heating

Latent heating in the atmosphere results from phase changes of water. At the Earth's surface water is evaporated into air parcels. As air parcels ascend they will cool adiabatically, as the temperature decreases the saturation pressure of water vapour decreases more rapidly than the air pressure and the water vapour must condense. The freezing of water vapour also produces latent heat and can be much more complex due to the different types of ice crystal that can form.

Modified forms of θ such as the wet-bulb (θ_w) and equivalent (θ_e) potential temperature can be used to take into account the latent heating and cooling effects from evaporation and condensation of water and can be treated similarly to θ for following air parcels. In the case that the moisture content is conserved the latent heating can be considered reversible because condensed water can be re-evaporated and vice-versa with no net latent heating. Air parcel ascent can be considered "pseudo-adiabatic" if the water is removed from the air parcel as it condenses: the air parcel will experience continuous latent heating while conserving θ_e/θ_w , although it is not reversible.

Latent-heating due the condensation of water vapour results in a low-level positive PV anomaly in cyclones that acts to intensify the cyclone by increasing the cyclonic vorticity ([Davis and Emanuel, 1991; Stoelinga, 1996](#)). The combination of the upper-level and low-level PV anomalies with the mid-level diabatic positive PV gives a coherent "PV tower" in mature extratropical cyclones ([Rossa et al., 2000](#)). In some cases the cyclonic circulation induced by latent heating of condensation can dominate cyclogenesis which

produces a distinct class of cyclones denoted type-C (following the type-A and type-B cyclones (Petterssen and Smebye, 1971)) (Deveson *et al.*, 2002; Plant *et al.*, 2003). In type-C cyclones there is an initial upper-level trough, but no surface θ anomaly; the upper-level trough initiates the low-level ascent which rapidly produces a positive PV anomaly (Ahmadi-Givi *et al.*, 2004).

Warm conveyor belts transport large amounts of evaporated water polewards and vertically; therefore, air parcels ascending in the warm conveyor belt will experience diabatic heating due to microphysical processes associated with phase changes of water. The distinction between the cyclonic and anti-cyclonic airstreams in the warm conveyor belt is possible early on in the ascent with the more strongly ascending anticyclonic branch having greater inflow moisture and as a result greater latent heating and ascent at an earlier stage (Martínez-Alvarado *et al.*, 2014b).

It is observed that the strongest ascending warm conveyor belt air parcels experience > 20 K of latent heating, but an average of almost zero change in PV (Madonna *et al.*, 2014) as shown in Fig. 1.8, resulting in the large negative PV anomaly relative to their surroundings at tropopause level. The result is that the latent heating in warm conveyor belts results in enhanced ascent associated with cross-isentropic transport of air masses. It is the gradient of latent heating along the warm conveyor belt that is important for the modification of PV. The heating structure of a warm conveyor belt can be described as a Gaussian-like peak at mid-levels through which trajectories ascend; as the trajectories ascend there is a positive PV tendency below the level of maximum latent heating and a negative PV tendency above. The net effect for the trajectories ascending through the full region of latent heating is roughly zero change in PV which can be explained as a result of the conservation of circulation and the PV impermeability theorem (Methven, 2015).

The negative PV anomalies produced by warm conveyor belts are an important contribution to the sharpening of the tropopause (Chagnon *et al.*, 2013). The tropopause is also indirectly sharpened due to warm conveyor belts transporting water vapour and producing clouds near the tropopause which enhances radiative cooling gradients at the tropopause (Kunkel *et al.*, 2016).

The enhancement of the ascent in a warm conveyor belt by diabatic processes leads to a stronger Rossby wave amplitude which leads to a more intense downstream cyclone

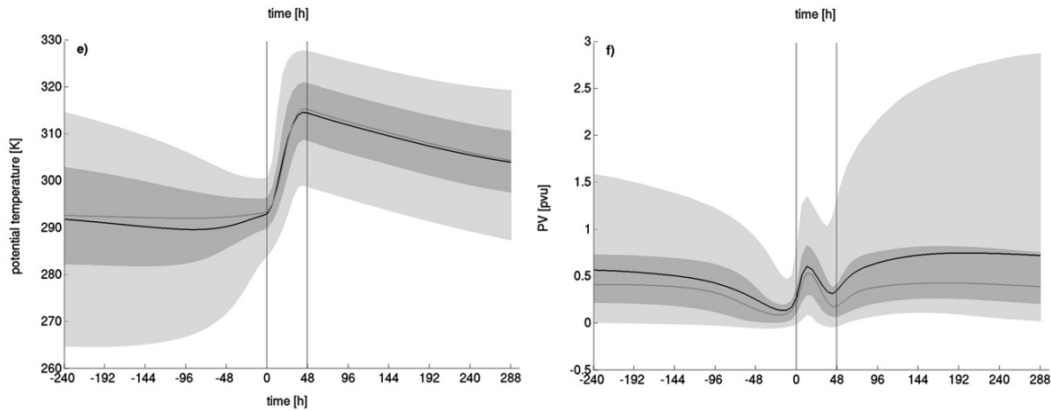


Figure 1.8: Figure 6 from [Madonna et al. \(2014\)](#). The evolution of (e) θ and (f) PV along warm conveyor belt trajectories in the North Atlantic winter. The trajectories are composed by their ascent phase marked by the vertical lines. “Black lines show the mean values over all trajectories, gray lines the median, and the dark and light gray areas represent the interquartile range (25th-75th percentiles) and the range between the 5th and 95th percentiles, respectively”. ©American Meteorological Society. Used with permission.

compared to a simulation with no moisture; in an equivalent dry simulation no warm conveyor belt could be identified with the 600-hPa ascent criteria ([Schemm et al., 2013](#)). Diabatically-enhanced ascent within warm conveyor belts is associated with an increased likelihood of persistent blocking downstream ([Pfahl et al., 2015](#)).

The negative PV anomaly associated with the warm conveyor belt can act to propagate cyclones poleward across the midlatitude jet ([Oruba et al., 2013](#)). The addition of moist processes enhances the negative PV anomaly and, therefore, the poleward propagation of the cyclone ([Coronel et al., 2015](#)). PV tendency analysis combined with idealised simulations has shown that without diabatic processes there is very little poleward propagation when averaged over many cyclones and the diabatic processes explain a large amount of the zonal tilt in the storm tracks ([Tamarin and Kaspi, 2016](#)). The poleward propagation of adiabatic cyclones is due to the cyclone starting equatorward of the jet so the poleward advection by the warm conveyor belt perturbs the sharpest PV gradient at the jet ([Rivière et al., 2012](#)).

1.4.5.4 Friction

Friction at the Earth's surface is an important component of the atmospheric circulation. The friction at the surface results in a boundary layer. The effects of surface friction are felt through the depth of the boundary layer, typically through the induced turbulent winds.

Surface friction acts to decrease the growth rate of cyclones ([Valdes and Hoskins, 1988](#)). A simple mechanism for understanding the effects of friction on cyclones is Ekman pumping. Figure 1.9 shows a schematic of the Ekman pumping mechanism. Figure 1.9a shows simple geostrophic balance where the wind (\mathbf{U}) is parallel to the isobars and the resulting Coriolis force (\mathbf{F}_C) balances the pressure gradient force (\mathbf{F}_p). Figure 1.9b shows the effect of imposing a simple frictional drag ($\mathbf{F}_d = -\frac{\mathbf{U}}{\tau}$, where τ is a friction coefficient) proportional and opposite to the wind. Since the Coriolis and frictional forces are perpendicular, for the forces to balance the frictional force must be balanced by a component of the pressure gradient force. For the same pressure gradient, the result is that the wind is rotated by an angle $\alpha = \arctan(\frac{1}{f\tau})$ and reduced by a factor $\varepsilon = \cos(\alpha)$. Therefore the friction results in an ageostrophic mass flux from high to low pressure. Figure 1.9c shows the effect of Ekman pumping on anticyclones and cyclones. In the boundary layer there is net mass flux away from the anticyclone ($\xi < 0$) compensated by descending air above resulting in an increase in vorticity by vortex stretching. The reverse is true for a cyclone ($\xi > 0$): there is a net mass flux in to the cyclone in the boundary-layer compensated by ascent resulting in a decrease in vorticity by vortex squashing. In both cases the vorticity anomaly is reduced by Ekman pumping.

The Ekman pumping mechanism implies generation of negative PV anomalies in cyclones. This is not necessarily the case in baroclinic systems where the winds can vary with height. If the thermal wind has a component opposing the surface wind then the turbulent fluxes of heat and momentum induced by boundary-layer friction can generate substantial positive PV anomalies in cyclones ([Cooper et al., 1992](#)). Simulations of cyclones with integrated tracers of PV showed that boundary-layer friction did result in positive PV anomalies that were transported to the cyclone centre, although the cyclone was weaker compared to simulations with no surface friction ([Davis et al., 1993; Stoelinga, 1996](#)). [Adamson et al. \(2006\)](#) explained why the positive PV anomaly would result in a weaker cyclone: the positive PV anomalies are generated downstream of the cyclone and

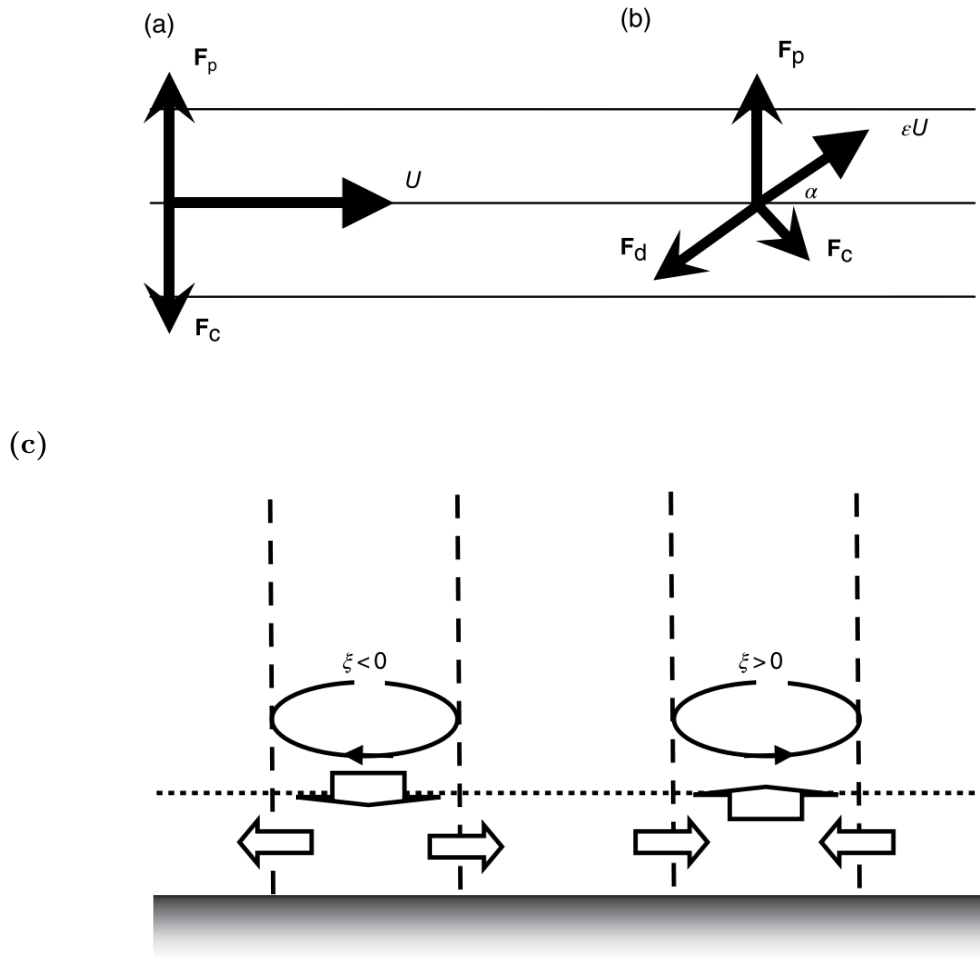


Figure 1.9: Schematics of Ekman pumping from [Hoskins and James \(2014\)](#): (a) and (b) are from Fig. 8.5 and (c) is from Fig. 8.6. Balance of forces for (a) geostrophic balance and (b) geostrophic balance with additional friction. (c) Schematic of Ekman pumping for a cross section through an anticyclone (left) and a cyclone (right).

advected by the warm conveyor belt out of the boundary layer and into the cyclone centre resulting in a thin layer of positive PV. From PV inversion the thin positive PV anomaly is associated with increased static stability which acts to reduce the coupling between the upper and lower-level Rossby waves and reduce the growth rate of the cyclone. Ekman pumping is important in shaping the positive PV anomaly into a static stability anomaly and can be of similar importance to the baroclinic generation of PV in baroclinic cyclones ([Boutle et al., 2015](#)).

1.5 Numerical Weather Prediction

Numerical weather prediction (NWP) is achieved by producing a set of initial conditions and using a numerical model of the atmosphere, which solves the governing equations given in section 1.2, to integrate forward in time. This essentially gives two sources of forecast errors: initial condition errors and model errors. It is impossible to ever have perfect initial conditions or a perfect model. Section 1.5.1 discusses how errors in initial conditions results in forecast errors due the inherent nature of the atmosphere and section 1.5.2 discusses how model errors result in forecast errors.

1.5.1 Predictability

The chaotic nature of atmospheric dynamics means that forecasts are sensitive to initial conditions. It was noted by [Eady \(1949\)](#) that since his model of baroclinic instability describes how synoptic scale disturbances can grow from arbitrarily small initial perturbations that small uncertainties in initial conditions will limit the lead time within which weather forecasting can provide any useful information. Using a simplified model of convection [Lorenz \(1963\)](#) demonstrated that small differences in initial conditions did grow so that two initially similar states could evolve to be as different as two randomly chosen states.

The dynamics of turbulence can inherently limit the predictability range of weather forecasting even for arbitrarily small initial condition errors. Using a two-dimensional vorticity equation [Lorenz \(1969\)](#) showed that more rapid error growth at smaller scales could result in saturation of errors within a fixed time. [Lorenz \(1969\)](#) showed that if the decrease of energy with decreasing length scales was shallower than k^{-3} , where k is wavenumber, then the upscale growth of error energy would saturate errors at the largest scale within a fixed time no matter what scale the initial error was reduced to. [Nastrom and Gage \(1985\)](#) calculated atmospheric spectra from aircraft data (Fig. 1.10): the atmosphere is characterised by a steep -3 spectral slope at large scales which transitions to a shallower $-5/3$ spectral slope at scales smaller than ≈ 400 km. For the two-dimensional turbulence model used by [Lorenz \(1969\)](#) a -3 spectral slope would be expected indicating a theoretically infinite predictability range; however, a $-5/3$ spectral slope can be justified using the surface quasi-geostrophic equations and gives a finite predictability limit

(Rotunno and Snyder, 2008). The growth of errors in weather forecasting is more likely to be dominated by small errors on large scales which will act to rapidly saturate errors at small scales (Durran and Gingrich, 2014).

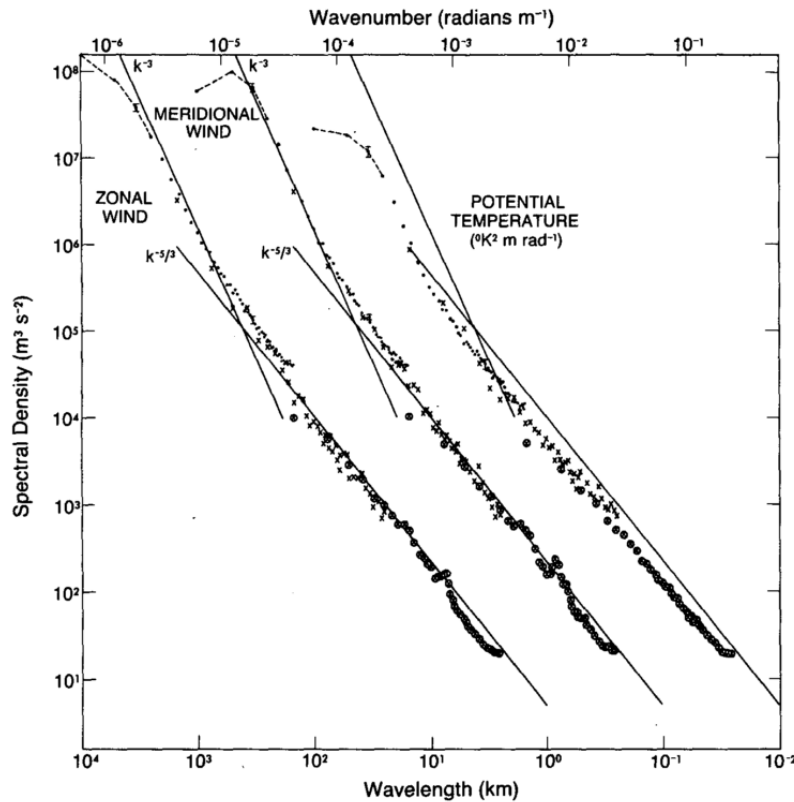


Figure 1.10: Figure 3 from Nastrom and Gage (1985). “Variance power spectra of wind and potential temperature near the tropopause from aircraft data. The spectra for meridional wind and temperature are shifted one and two decades to the right, respectively; lines with slopes -3 and $-\frac{5}{3}$ are entered at the same relative coordinates for each variable for comparison”. ©American Meteorological Society. Used with permission.

Longer timescale predictability can be achieved because the atmosphere does not lose predictability uniformly. Ensemble forecasts are used to quantify the uncertainty of a given forecast. Ensemble forecasts are achieved by running multiple forecasts with perturbed initial conditions to account for the uncertainty in the initial conditions. The result is a set of possible outcomes that can be used to construct probability distributions. Framing forecasts in terms of probabilities is key to achieving predictability beyond 10 days (Buizza and Leutbecher, 2015).

Given the limiting factor of initial condition uncertainty on the predictability limits

of weather forecasting an import process in weather forecasting is specifying the initial conditions. The issue with NWP is that the observational data available is uncertain and sparse compared to the resolution of NWP models. To provide useful initial conditions for NWP models other constraints need to be applied in addition to the observational data. “Data assimilation” techniques are used in NWP to produce the optimal initial conditions, known as the analysis, given the constraints. Data assimilation methods can be described in terms of Bayes’ theorem,

$$P(x=x_t|y=y_{obs}) \propto P(y = y_{obs}|x = x_t)P(x = x_t), \quad (1.32)$$

([Lorenc, 1986](#)). Equation 1.32 states that the probability that the model state (x) corresponds to the true state of the atmosphere (x_t), given the observations (y_{obs}), is proportional to the probability of obtaining the observations given the model state is the true state, multiplied by the probability that the model state is the true state. The problem that data assimilation solves is to find the optimum model state, the analysis, that maximises, or finds the minimum variance of, Eq. 1.32 ([Lorenc, 1986](#)). The first guess of the model state can be provided by the forecast. The observations then constrain the model state where they can. Additional constraints can be applied by considering the time variation of the model run that best matches the observations as well as the knowledge that the atmosphere is approximately balanced.

1.5.2 Model Errors

A numerical model of the atmosphere can be considered as the combination of a dynamical core, which solves the adiabatic and frictionless governing equations, and physics parametrizations. Figure. 1.11 shows a schematic of the processes that are typically parametrized in numerical models of the atmosphere. The parametrizations represent physical processes that are not represented by the adiabatic and frictionless dynamics (e.g. radiation and microphysics) or processes that are not well resolved (e.g. convection and turbulent mixing). Parametrizations are simplified representations of these processes to account for limited computing power. Model errors can arise from parametrization schemes for various reasons such as oversimplification of the physical processes representation or uncertainty in the parameters used within the parametrization.

The representation of poorly resolved processes, such as convection and turbulent-mixing, can be improved through increased resolution; however, this requires increased

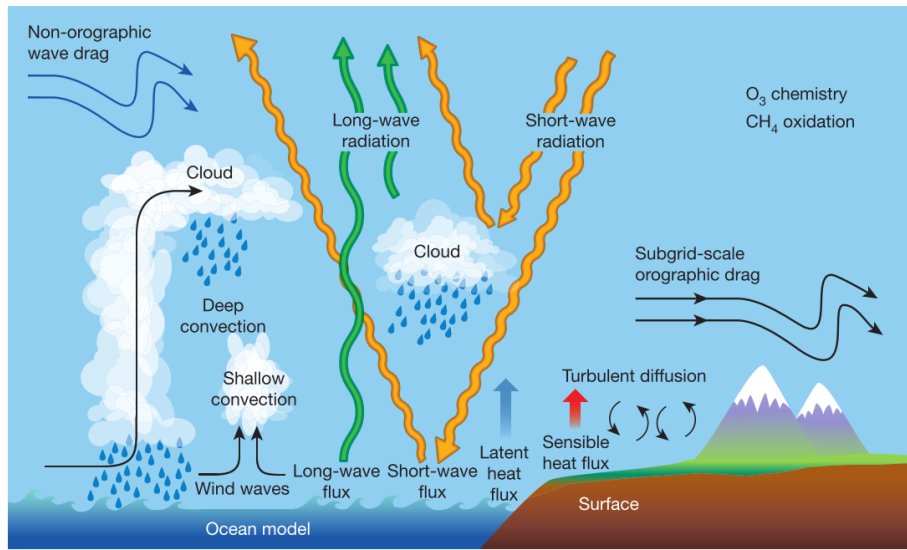


Figure 1.11: Figure 2 from [Bauer et al. \(2015\)](#) depicting the physical processes typically parametrized in NWP and/or climate models. Reprinted by permission from Macmillan Publishers Ltd: *Nature* ([Bauer et al., 2015](#)), copyright (2015).

computing power. One way of increasing resolution without increasing computational cost, such as in this thesis, is to use limited-area domains. The use of limited-area domains has allowed for numerical weather prediction models to be run at high enough resolutions to not require parametrized convection yielding significant improvements in forecasts (e.g. [Lean et al., 2008](#)). In the case of limited-area domains, the lateral boundary conditions also represent another source of forecast errors.

Forecast errors are typically quantified as the difference between the forecast and the analysis (e.g. [Bauer et al. \(2015\)](#)). It is not trivial to disentangle the contributions of initial condition errors and model errors from forecast errors. An example of this is forecast busts over Europe which have been linked to precursor errors over the USA 5-6 days beforehand ([Rodwell et al., 2013](#)). The initial error is in the prediction of the effects of latent-heat release over the eastern USA on the jet stream in a ridge-trough pattern over North America. The initial errors are then amplified and propagated by the Rossby wave packet ([Rodwell et al., 2013](#)). The isentropic tropopause PV gradient has been shown to decrease as a function of forecast lead time in global NWP models ([Gray et al., 2014](#)) which will lead to errors in the downstream propagation of Rossby waves ([Harvey et al., 2016](#)) and could be linked to the initial effects of diabatic processes on the jet stream; however, [Rodwell et al. \(2013\)](#) also showed that the forecast busts

had large initial condition uncertainty indicating that it may just be a situation with low predictability.

Since the same models are often used for weather and climate prediction, a simple way to identify model errors is to identify climate model biases. Since weather forecasting is concerned with the prediction and proper representation of individual events of certain features (e.g. extratropical cyclones) whereas climate prediction is concerned with the changes in the climatological frequency and behaviour of these features (e.g. position and strength of the storm tracks), climate prediction should not be affected by initial conditions. This approach is computationally expensive because it requires the model to be run for a long time to identify systematic biases so climate prediction uses much lower resolution than weather prediction.

Model errors can be identified from short forecasts if systematic forecast errors are considered. At short lead times, the systematic difference between forecasts and analyses is equivalent to the systematic imbalance between model processes. Figure 1.12 shows a schematic with systematic forecast errors in a forecast-analysis cycle. A forecast is run from an analysis that is close to the observations. The forecast drifts from the observations until the model state is brought back to be close to the observations at the next analysis step. Figure 1.12 depicts a systematic error because the forecast drift is always in the same direction such that the analysis increments always have the same sign. A similar approach can be taken for ensemble forecasts by considering the reliability (Palmer *et al.*, 2008; Rodwell *et al.*, 2016). A reliable ensemble is one where the predicted probability of an event matches the observed frequency of the event.

The structure and amplitude of errors from short forecasts has been shown to closely resemble the long-term biases from the same model; therefore, by identifying the processes that result in systematic short-term forecast errors, the origins of climate model bias are also identified (Palmer *et al.*, 2008). Insight into the origin of model imbalances can be obtained by considering the “initial tendencies” from each model process individually (Klinker and Sardeshmukh, 1992; Rodwell and Palmer, 2007). The initial tendencies quantify the contributions of each process to the systematic forecast errors allowing for a computationally inexpensive method of identifying the important processes and quantifying the impacts of changes to model processes on the systematic errors. In this thesis, PV tracers are used to quantify the effects of individual model processes following air masses.

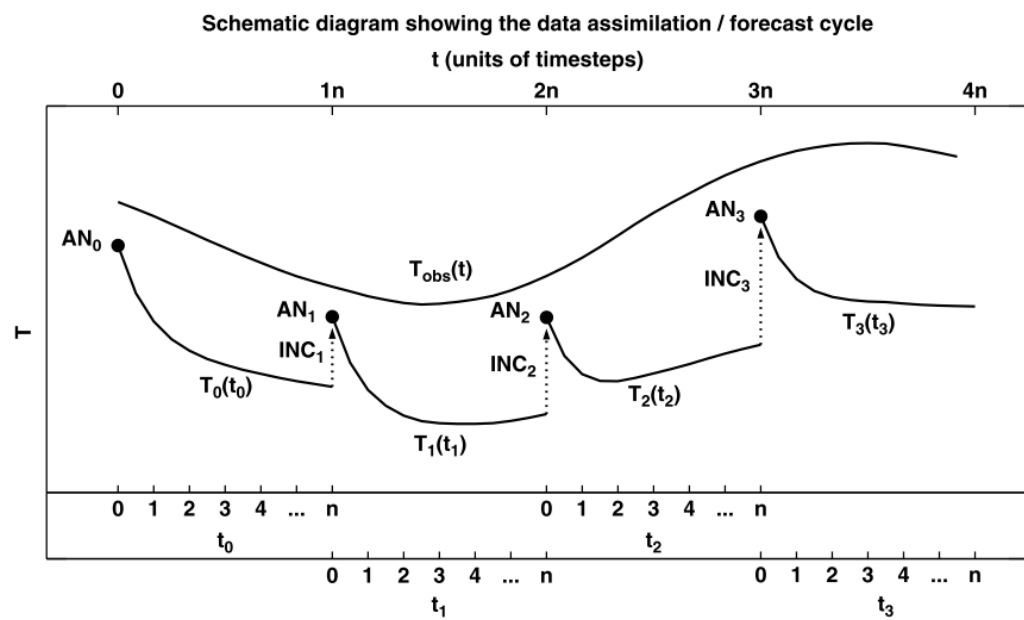


Figure 1.12: Figure 1 from Rodwell and Palmer (2007). Schematic of the data assimilation and forecast integration cycle in numerical weather prediction. A forecast ($T_i(t_i)$) of a variable (T) is initialised from an analysis (AN_i) which is subsequently incorporated with the observations ($T_{obs}(t)$) at the next analysis step with an analysis increment, INC_i .

Chapter 2

Methods

The main technique used in this thesis involves using PV tracers to accumulate the effects of different physical processes (section 2.2) integrated online in the Met Office Unified Model (MetUM) (section 2.1). The model setup described below has been used to produce forecasts of two case studies (section 2.3) and a set of 92 forecasts, initialised daily over a winter season (section 2.4).

2.1 Met Office Unified Model

The Met Office Unified Model (MetUM) is an operational numerical weather prediction model and also the basis of the Hadley centre climate model. The term “unified” is used to describe the seamless approach of using the MetUM for weather and climate prediction. In the following sections the model grid (section 2.1.1), parametrization schemes (section 2.1.2) and formulation (section 2.1.3) of the MetUM used in this thesis are described. The configuration used in this thesis is from version 7.3, parallel suite 22, which was used operationally from 10 November 2009 until 9 March 2010.

2.1.1 Grid

The prognostic variables in the MetUM are \mathbf{u} , θ , ρ , the mass mixing ratios of moisture variables (specific humidity (σ), cloud ice (σ_{cf}) and cloud liquid(σ_{cl})), and Exner pressure. The variables in the MetUM are placed on an C-grid (Arakawa and Lamb, 1977) with Charney-Phillips staggering in the vertical (Charney and Phillips, 1953) using a terrain-following, height-based, coordinate that gradually flattens at higher altitudes (Davies *et al.*, 2005). The simulations in this thesis use 70 non-uniformly spaced vertical model levels up to 80 km; Fig. 2.1a shows the vertical-level spacing for the first 50 model levels on which θ is stored (θ -levels).

The simulations in this thesis use a limited area configuration known as the NAE

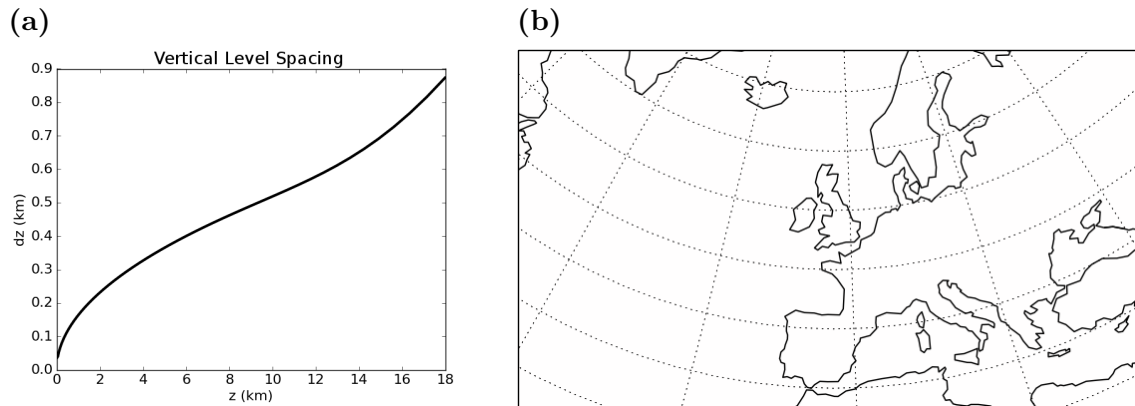


Figure 2.1: The NAE (North Atlantic European) domain. (a) Height spacing for the first 50 model levels above sea-level. (b) Horizontal grid coverage excluding the lateral boundaries.

(North Atlantic and European) that was used operationally until February 2014. Figure 2.1b shows the extent of the NAE domain. The NAE domain has 0.11° horizontal grid spacing and uses a rotated pole to centre the domain on the equator giving, an approximately uniform, 12-km horizontal grid spacing. The simulations in this thesis use a standard timestep for this domain of 5 minutes. The initial conditions used are from operational NAE analyses and boundary conditions are given by operational runs of the global model for the same start time using the downscaling method described in Davies (2014).

2.1.2 Parametrisation Schemes

The MetUM contains various parametrizations to account for physical processes that are either not resolved or not represented within the dynamical core, each of which are described in the following sections. The schemes are: microphysics (section 2.1.2.1); radiation (section 2.1.2.2); orographic and non-orographic gravity-wave drag (section 2.1.2.3); turbulent-mixing including the boundary-layer (section 2.1.2.4); and convection (section 2.1.2.5).

2.1.2.1 Microphysics

Figure 2.2 shows the various processes represented by the microphysics scheme in the MetUM. The condensation and evaporation between water vapour and liquid is represented by diagnosing the liquid water content as any, non-ice, water content exceeding the gridbox saturation vapour pressure. When the gridbox average value of humidity is below saturation a fraction of the grid box can still be diagnosed as cloudy due to the subgrid-scale variability. The diagnostic cloud scheme is only applied if the gridbox average relative humidity exceeds a critical value. The critical values used here are 0.91 for the lowest model θ level, following by a linear decrease from 0.9 to 0.8 over the following 6 vertical levels and 0.8 elsewhere. The distribution of mixing ratios over a gridbox are then set to follow a symmetric triangular probability distribution (Smith, 1990).

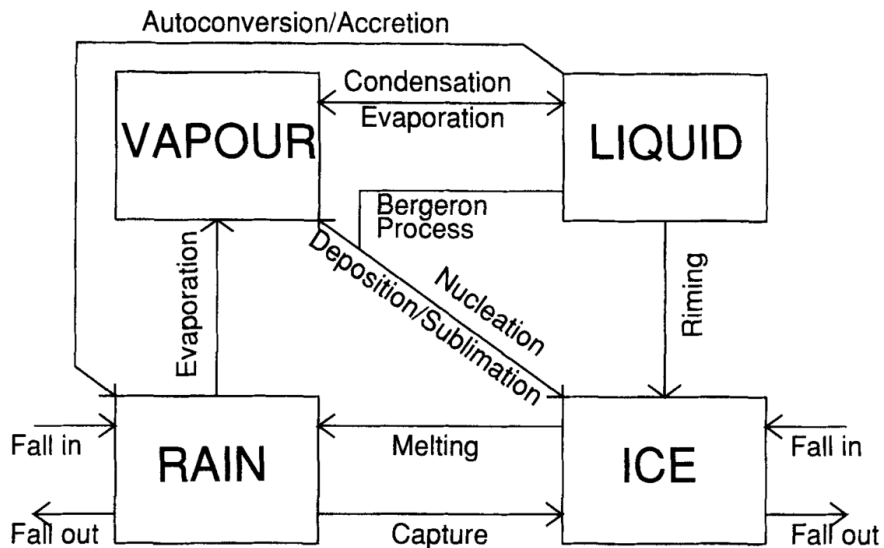


Figure 2.2: Figure 1 from Wilson and Ballard (1999) showing the transfers between water quantities modelled by the large-scale precipitation scheme.

The remaining transfer and conversion of moisture variables are calculated from the top down within a column of air. The change in each moisture variable from each process is calculated within a gridbox (the order is given in Wilson and Ballard (1999)). The result is that each of the moisture variables are modified as well as temperature from the latent heating and cooling. Any diagnosed rain is assumed to fall to the surface within the timestep. A fraction of the ice content is then transferred to the grid box below and the process is repeated until the bottom of the domain is reached, any transfer of ice

content from the bottom gridbox is diagnosed as snow.

2.1.2.2 Radiation

Radiative transfer in the MetUM is calculated in vertical layers using the two-stream approximation (Edwards and Slingo, 1995). The fluxes are calculated separately for short-wave (solar) radiation and long-wave (thermal) radiation. The fluxes in the short-wave and long-wave spectral regions are calculated as the sum of partial fluxes by subdividing the spectral regions into several monochromatic bands. The radiation scheme takes account of the different types of cloud and water vapour. The radiation scheme also accounts for ozone; for the simulations in this thesis the distribution of ozone is set to a prescribed 3D climatology. To reduce the computational expense of the scheme the increments are not recalculated every timestep (Edwards and Slingo, 1995). For the simulations in this thesis the increments are recalculated every hour.

2.1.2.3 Gravity-Wave Drag

The orography in the MetUM is described in terms of the average height of the surface in each gridbox and the standard deviation of the height within a gridbox, including standard deviations taken in perpendicular directions to account for the anisotropy of the orography (Webster *et al.*, 2003). The dynamical core of a numerical model produces gravity-waves due to the resolved variability of the orography but subgrid scales must be parametrized. The surface orography and standard deviations are filtered so that scales less than six times the model grid-scale, the scale at which the model can skillfully resolve orographic features (Davies and Brown, 2001), are parametrized (Webster *et al.*, 2003).

The total parametrized surface stress is calculated from an analytical expression for 2-dimensional non-rotating frictionless flow (Webster *et al.*, 2003). The stress is proportional to the mass flux over the orography, the static stability and the standard deviation of the subgrid-scale orography (accounting for anisotropy). The total stress (τ) is partitioned into two components: the blocked flow (τ_{bf}) and gravity-wave drag (τ_{gwd}).

$$\tau = \tau_{bf} + \tau_{gwd}, \quad (2.1)$$

$$\tau_{gwd} = \tau \cdot \left(\frac{t}{h} \right)^2, \quad (2.2)$$

where h is height of the “tops of the subgrid mountains” defined to be 2.5 times the

standard deviation of the subgrid-scale orography and t is the “top layer” where the Froude number reaches a critical value of order 1 (Webster *et al.*, 2003). The simulations in this thesis use a critical Froude number of 4. The stress is applied as a linear decrease from τ_{bf} at the surface to τ_{gwd} at height h (Webster *et al.*, 2003). The distribution of gravity-wave stress above the blocked flow is then diagnosed by launching gravity-waves from height h . At each level a critical stress is calculated; if the gravity-wave stress exceeds the critical stress it is reduced to the critical stress with the difference being deposited at that level following McFarlane (1987).

Non-orographic gravity-waves are parametrized using the spectral gravity wave scheme of Warner and McIntyre (1999) with the modifications of Scaife *et al.* (2002). A continuous spectrum of gravity-waves is launched from a fixed level near the surface and propagated conservatively to consecutive vertical levels. The launch spectrum is defined to give a fixed flux of horizontal momentum with a homogeneous wave stress (Scaife *et al.*, 2002). As the wave spectrum is propagated, positive vertical wind shear will Doppler shift the wave spectrum towards zero frequency approaching critical levels. The conservative propagation is approximated as hydrostatic and nonrotating which simplifies the doppler shifting calculations (Warner and McIntyre, 1999). At each level the gravity-wave spectra is limited by a “chopping function” based on observational constraints of an m^{-3} spectral slope for gravity waves, where m is vertical wavenumber (Warner and McIntyre, 1996). The chopping function removes the momentum from the wave spectra associated with the breaking waves and the horizontal wave forcing in each layer is then diagnosed from the section of the wave spectra removed by the chopping function (Warner and McIntyre, 1999).

2.1.2.4 Turbulent Mixing and Boundary-Layer Scheme

The turbulent mixing scheme in the MetUM is based on the scheme of Lock *et al.* (2000). The effects of vertical turbulent mixing are calculated as a downgradient diffusion using height dependent diffusion coefficients (K-profiles) (Lock *et al.*, 2000). The downgradient diffusion is applied to the specific total water content, momentum and the liquid-frozen water potential temperature,

$$\theta_l = T - \frac{L}{c_p} \sigma_{cl} - \frac{L_s}{c_p} \sigma_{cf} + \frac{g}{c_p} z, \quad (2.3)$$

where L and L_s are the latent heat of evaporation and sublimation respectively (Lock *et al.*, 2000). Additional non-local mixing is applied to θ_l (Lock *et al.*, 2000). The turbulent-mixing scheme can also include nonlocal momentum mixing (Brown *et al.*, 2008); however, it is not applied in the simulations in this thesis. The variables chosen are conserved for adiabatic and pseudo-adiabatic motions providing a consistent formulation of mixing for dry and moist regions. There are three different coefficients used depending on what is driving the turbulence:

$K(\mathbf{Ri})$ shear driven turbulence calculated as a function of the Richardson number (Ri)
(Smith, 1990)

K_{surf} surface driven turbulence in unstable boundary layers

K_{Sc} turbulence driven by cloud-top buoyancy forcing

The flux of a quantity, χ , is then calculated as

$$\overline{w'\chi} = - \max[K_{\text{surf}} + K_{\text{Sc}}, K(\mathbf{Ri})] \frac{\partial \chi}{\partial z}. \quad (2.4)$$

The Richardson number based coefficient is taken when it is larger than the other terms to ensure a smooth transition between different mixing regions (Lock *et al.*, 2000).

The first step of the turbulent-mixing parametrisation is to diagnose the different mixing regions. Figure 2.3 shows where the different mixing regimes are applied and typical vertical distributions of the different K-profiles. The regions of mixing can be categorised into three types of boundary-layer: stable (a), well-mixed (c) and cumulus capped (f) with the possible addition of a decoupled stratocumulus layer to each (b, d and e). There is also a seventh type of boundary-layer, the shear dominated boundary-layer (to be described below).

The boundary layer is diagnosed as unstable if the surface buoyancy flux is positive. If the boundary-layer is diagnosed as stable, the depth of the boundary layer is diagnosed as where the Richardson number drops below a critical value of 0.25. In this stable boundary layer and any equivalent layers of below critical Richardson number in the free troposphere, the turbulent fluxes are calculated as a function of the Richardson number,

$$K(\mathbf{Ri}) = l^2 \left| \frac{\partial \mathbf{u}}{\partial z} \right| f(\mathbf{Ri}), \quad (2.5)$$

where l is a mixing length scale and $f(\mathbf{Ri})$ is shown in Fig. 2.4. Two different forms of $f(\mathbf{Ri})$ are used (Brown *et al.*, 2008): for grid-points over sea $f(\mathbf{Ri})$ is prescribed to fit

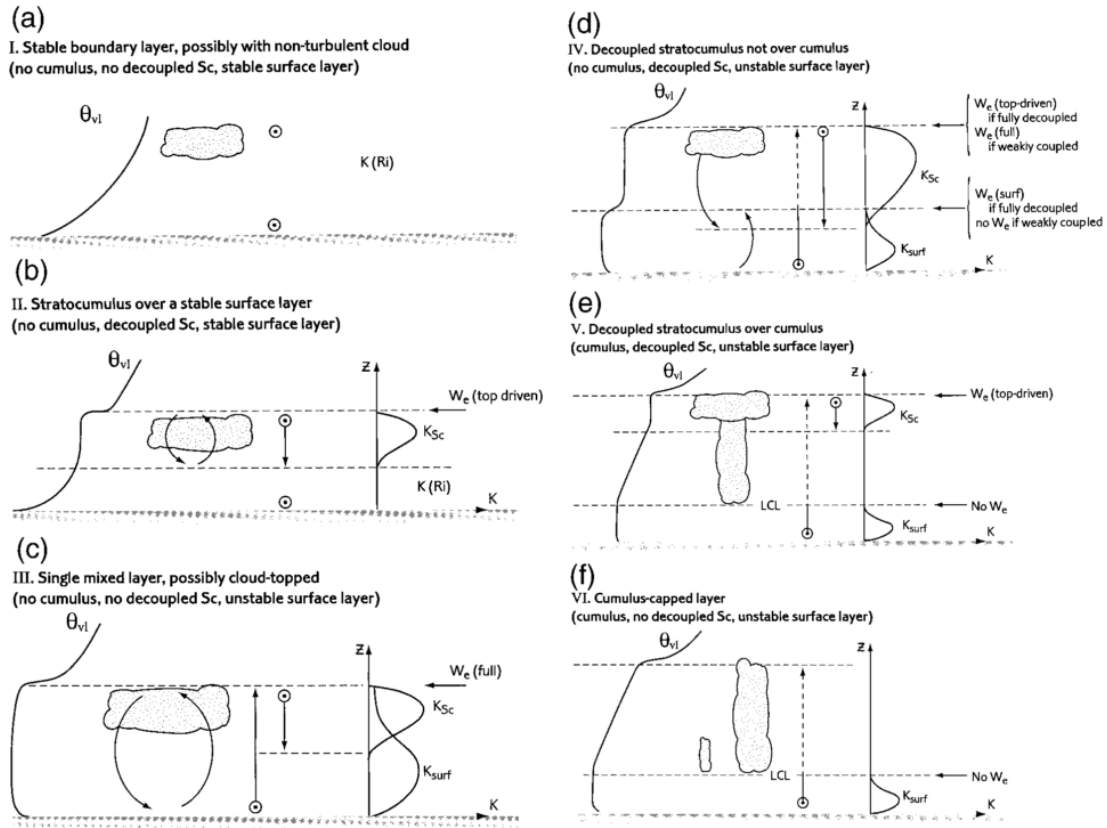


Figure 2.3: Figure 1 from Lock *et al.* (2000) showing the different types of boundary-layer identified in the parametrization scheme and the associated mixing coefficients (K_i) and entrainment velocities (w_e). Note that there is a seventh boundary-layer type not included in this figure (described in the text). ©American Meteorological Society. Used with permission.

expected mixing rates from theory; for grid-points over land a “long-tailed” function is used to artificially increase the derived mixing at higher stabilities.

For unstable boundary layers, the depth of the layer is diagnosed by a diagnostic parcel ascent from the surface with θ_l perturbed by an amount proportional to the surface buoyancy flux (Lock *et al.*, 2000). The boundary-layer height is diagnosed as the height at which the air parcel becomes neutrally buoyant or, if above the lifting condensation level, the air parcel achieves maximum buoyancy excess (Lock *et al.*, 2000). If the air parcel has ascended above the lifting condensation level, the boundary-layer is diagnosed as cumulus capped if the moisture gradient above the lifting condensation level is $> 1.1 \times$ the moisture gradient below the lifting condensation level; otherwise, it is classified as

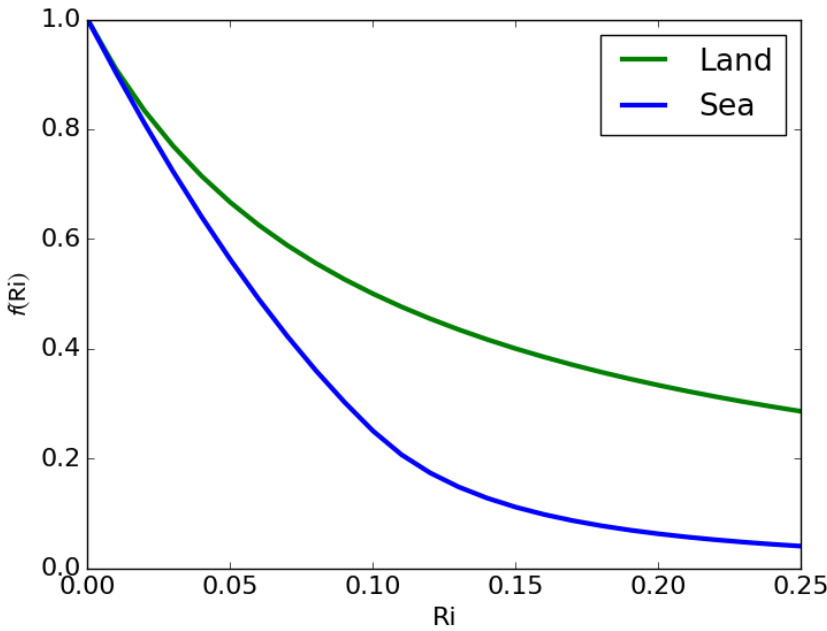


Figure 2.4: $f(Ri)$ used in Eq. 2.5 as a function of the Richardson number from the functions given in [Brown et al. \(2008\)](#) for land and sea gridpoints.

well mixed ([Lock et al., 2000](#)). For a cumulus-capped boundary layer, the boundary-layer height is then set as the height of the lifting condensation level and the mixing in this region is represented solely by the convection scheme ([Lock et al., 2000](#)). Shear generation of turbulence is allowed to inhibit cumulus convection: a “shear-dominated” boundary layer is diagnosed if a surface layer with below critical Richardson number extends above the diagnosed cumulus convection layer. In this case, the mixing is calculated using the Richardson number dependant coefficient rather than the convection scheme ([Lock et al., 2015](#)).

A stratocumulus layer is diagnosed if the cloud fraction at the top of the diagnosed boundary layer (before being modified in the case of cumulus-capped boundary layers) is above a critical value of 0.1 ([Lock et al., 2000](#)). The depth of the decoupled stratocumulus layer is then diagnosed by a diagnostic parcel descent: the air parcel is perturbed by a term proportional to the radiative cloud-top cooling rate and the bottom of the stratocumulus layer is diagnosed as the height at which the air parcel virtual θ_l exceeds that of the environment ([Lock et al., 2000](#)). Entrainment in decoupled stratocumulus layers is also parametrized using the method of [Lock \(1998\)](#). A second diagnostic parcel descent is made after accounting for entrainment and the largest depth is then taken for the depth

of the stratocumulus layer.

2.1.2.5 Convection

The convection scheme used in the MetUM can be divided in to two parts: convection in cumulus layers diagnosed by the turbulent-mixing scheme and “mid-level” convection for all remaining grid points above the boundary layer with excess buoyancy. The cumulus convection is further divided into “shallow” convection, if the top of the cumulus layer diagnosed by the turbulent-mixing scheme is below either the freezing level or 2.5 km, and “deep” convection otherwise. The parametrisation of each type of convection is based on the scheme of [Gregory and Rowntree \(1990\)](#) with pragmatic modifications for each different type of convection. The scheme of [Gregory and Rowntree \(1990\)](#) parametrises the modifications to prognostic variables in terms of the vertical mass flux averaged over an ensemble of convective plumes much smaller than the grid-scale. For mid-level and deep convection the initial mass flux is determined from the convective available potential energy ([Walters *et al.*, 2011](#)): an adjustment timescale of 30 minutes is used for the simulations in this thesis. For shallow convection the initial mass flux is determined from the boundary-layer turbulent kinetic energy ([Grant, 2001](#)).

The modifications of prognostic variables arise from the exchange of air between convective plumes and the environment by entrainment, mixing detrainment and forced detrainment. The entrainment and mixing detrainment are proportional to the cloud mass flux and forced detrainment acts when the excess buoyancy of an air parcel drops below a threshold value ([Gregory and Rowntree, 1990](#)). The scheme uses a height dependent entrainment rate to account for a mix of shallow and deep clouds near the surface transitioning to only deep clouds reaching the upper troposphere ([Gregory and Rowntree \(1990\) Fig. 2](#)). The scheme also includes terms for phase changes of water and the resulting latent heat release. Convective momentum transport ([Gregory *et al.*, 1997](#)) can also be accounted for, in addition to heat and moisture modifications in the original scheme ([Gregory and Rowntree, 1990](#)) and is included in the simulations in this thesis.

The convection scheme can produce precipitation when updraught cloud depth and cloud amount within an air parcel exceed threshold values ([Gregory and Rowntree, 1990](#)). The critical cloud depth is smaller over sea than over land to account for differences in concentrations of condensation nuclei when prognostic aerosols are not included in the

model (Gregory and Rowntree, 1990). The amount of precipitation formed over a gridbox is then proportional to the excess cloud amount (Gregory and Rowntree, 1990); the phase of the precipitation is determined by the temperature of the air parcel in which it initiates. Freezing and melting, and the resulting latent heat release, is represented at the freezing level of the environment (Gregory and Rowntree, 1990). Below cloud base, snow is allowed to fall to the ground and rain is evaporated at a rate proportional to the environment subsaturation (Gregory and Rowntree, 1990).

Precipitation can also maintain downdraughts. Downdraughts are essentially parametrized as updraughts in reverse: a descending air parcel interacts with the environment through entrainment, mixing detrainment and forced detrainment (Stratton *et al.*, 2015). A downdraught is initiated if an updraught is terminated in saturated air with a cloud depth and precipitation rate above threshold values (Stratton *et al.*, 2015). The downdraught continues for as long it can be maintained by latent heat release from evaporation and sublimation of precipitation (Stratton *et al.*, 2015).

2.1.3 Formulation of the Unified Model

The dynamical core of the MetUM version used here approximates a two time level, semi-implicit, semi-Lagrangian solution to the nonhydrostatic, deep atmosphere, equations (Davies *et al.*, 2005). The MetUM solves the governing equations of the atmosphere using a “predictor-corrector” method; an initial “predictor” is made of the prognostic variables at time level $n+1$ and is refined using a set of “correctors”. The full method and governing equations are set out by Davies *et al.* (2005) and the inclusion of parametrized physical processes to the equations is presented in Diamantakis *et al.* (2007). A simplified description of the method, based on section 5 of Davies *et al.* (2005) and section 2 of Diamantakis *et al.* (2007), is given here so that the budget of PV in the MetUM can be described precisely in the following section.

The discretisation of the governing equations that the MetUM aims to approximate is given by

$$\frac{\mathbf{X}^{n+1} - \mathbf{X}_d^n}{\Delta t} = (1 - \alpha)(\mathbf{L} + \mathbf{N})_d^n + \mathbf{S}\mathbf{P}_d^n + \alpha(\mathbf{L} + \mathbf{N})^{n+1} + \mathbf{F}\mathbf{P}^{n+1}, \quad (2.6)$$

where \mathbf{X} is a vector of the prognostic variables in the MetUM; \mathbf{L} and \mathbf{N} are the linear and

nonlinear dynamics terms respectively; \mathbf{SP} and \mathbf{FP} are the tendencies of the “slow” and “fast” parametrized physical processes; a subscript “ d ” denotes evaluation at departure points in the MetUM’s semi-Lagrangian method; α is a time-weighting coefficient (typically 0.7); n and $n + 1$ are the time levels; and Δt is the time step. Figure 2.5 shows a schematic of a single timestep of the MetUM which demonstrates the application of the predictor-corrector method to solving Eq. (2.6). The components of this figure are now described.

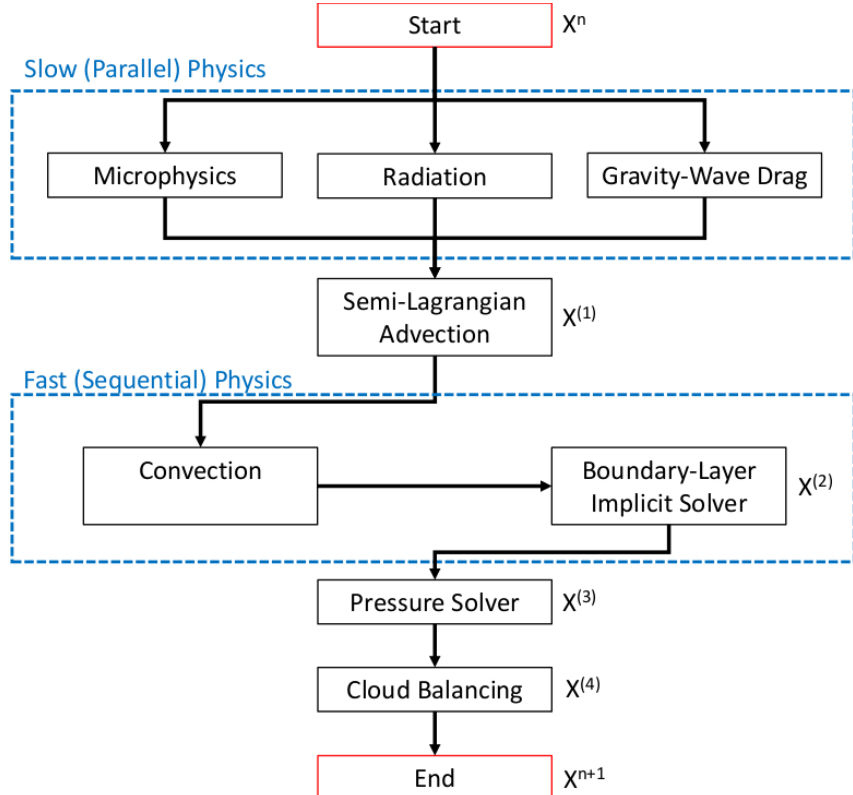


Figure 2.5: A schematic of a single timestep of the MetUM.

First, a set of increments due to the slow physical processes (microphysics (mic), radiation (rad) and gravity-wave drag (gwd)) are calculated from the set of prognostic variables at the start of the timestep. The increment to prognostic variables due to slow physical processes can be written as

$$\mathbf{SP} \equiv \mathbf{SP}(\mathbf{X}^n). \quad (2.7)$$

Next solutions to the thermodynamic, moisture and momentum equations are approximated. This is the predictor step for \mathbf{X} . Equation (2.6) is solved explicitly with time

level $n + 1$ values replaced with time level n estimates. This can be written as

$$\mathbf{X}^{(1)} = \mathbf{X}_d^n + \Delta t \{(1 - \alpha)(\mathbf{L} + \mathbf{N})_d^n + \alpha(\mathbf{L} + \mathbf{N})^n + \mathbf{SP}_d^n\}, \quad (2.8)$$

where $\mathbf{X}^{(1)}$ is the first estimate of \mathbf{X}^{n+1} . Note that the increments due to slow physical processes, interpolated to departure points, are added on at this stage: this can therefore be described in two steps, with an intermediate step of

$$\mathbf{X}^{(1)} = \mathbf{X}^{sl} + \Delta t \mathbf{SP}_d^n, \quad (2.9)$$

where \mathbf{X}^{sl} is the set of prognostic variables after the semi-Lagrangian dynamics only and the slow physical processes increments act as the first corrector for \mathbf{X} .

The next corrector adds the effects of fast physical processes (convection (*con*) and boundary layer (*bl*)) using the most up to date estimates of the prognostic variables. The fast physical processes are calculated sequentially for stability. This can be written as

$$\mathbf{X}^{(2)} = \mathbf{X}^{(1)} + \Delta t \mathbf{FP}(\mathbf{X}^n, \mathbf{X}^{(1)}, \mathbf{X}^{(2)}). \quad (2.10)$$

At this stage density and Exner pressure have not been updated from their time-level n estimates. The continuity equation is discretised in an Eulerian form and Exner pressure is used to couple the prognostic variables using the ideal gas equation of state. The back substitution of the equations to replace time-level n estimates with $n + 1$ values leads to a Helmholtz-type equation to solve; the full equations are given in appendix B of [Davies et al. \(2005\)](#). This is known as the pressure solver and is written as another corrector:

$$\mathbf{X}^{(3)} - \alpha \Delta t \mathbf{L}(\mathbf{X}^{(3)}) = \mathbf{X}^{(2)} + \alpha \Delta t (\mathbf{N}^* - \mathbf{N}^n - \mathbf{L}^n), \quad (2.11)$$

where \mathbf{N}^* is the latest estimate of \mathbf{N} .

At the end of the timestep the MetUM modifies the prognostic variables in clouds to eliminate supersaturation and account for the additional latent heat release (known as cloud balancing). This can be considered as a final physical process corrector:

$$\mathbf{X}^{(4)} = \mathbf{X}^{(3)} + \Delta t \mathbf{CB}(\mathbf{X}^{(3)}), \quad (2.12)$$

such that $\mathbf{X}^{n+1} \equiv \mathbf{X}^{(4)}$.

The semi-Lagrangian method does not explicitly conserve any variables; however, the choice of an Eulerian discretisation of the continuity equation ensures local mass conservation ([Davies et al., 2005](#)). No explicit diffusion is applied to prognostic variables:

the diffusion in the MetUM is entirely implicit and a result of the cubic interpolation (quintic for moisture variables) used in the semi-Lagrangian scheme. The MetUM contains a modified vertical interpolation for θ , described in section 6 of [Davies et al. \(2005\)](#), that is required for stability. This modified vertical interpolation is applied up to a height of 3.4 km in the NAE simulations.

2.2 PV Tracers

2.2.1 Method

A set of PV tracers is integrated online in the MetUM for each forecast in this thesis. The method is based on [Davis et al. \(1993\)](#) and was first applied to the MetUM by [Gray \(2006\)](#). The general method is to integrate the Lagrangian PV tendency of PV (Eq. (1.13)) along trajectories over a forecast of time T :

$$\int_{t_0}^{t_0+T} \frac{Dq}{Dt} dt = q(0) + \int_{t_0}^{t_0+T} S dt, \quad (2.13)$$

where t_0 is the forecast start time and S represents the right-hand side of Eq. (1.13). S can be partitioned into different physical processes ($S = \sum S_i$) resulting in a set of PV tracers (q_i) from the integration of S_i starting with each $q_i = 0$:

$$q(0) + \int_{t_0}^{t_0+T} \frac{Dq}{Dt} dt = q(0) + \sum q_i. \quad (2.14)$$

The PV diagnostics are essentially mimicking the behaviour of the numerical weather prediction model in terms of PV, allowing the tendencies of each parametrized physical process to be partitioned and accumulated separately. There is an implicit assumption here that the effects of each parametrized physical process can be separated. In practice the PV tracers will often have large cancelling terms between compensating processes. It is important to consider all terms in the PV budget to assess where this is the case.

2.2.2 Formulation in the MetUM

PV is partitioned into an advection-only PV tracer (q_{adv}) and a set of physics PV tracers ($\sum q_{phys}$). Each PV tracer, apart from the advection-only PV tracer, is set to zero everywhere at the initial time and the advection-only PV tracer is initialised as equal to the PV diagnosed from the prognostic variables \mathbf{X} (diagnosed PV). At the lateral

boundaries of a limited area domain each PV tracer, apart from the advection-only PV tracer, is set to zero and the advection-only PV is set equal to the diagnosed PV, at each timestep. This is because there is no prior information on the history of the air parcels at the lateral boundaries so they are treated like initial conditions.

In the MetUM tracers are advected by the flow resolved in the model using its semi-Lagrangian advection scheme. Passive tracers can also be transported by the effects of sub-grid parametrizations for turbulence and convection ([Lock *et al.*, 2000](#); [Gregory and Rowntree, 1990](#)). The parametrized sub-grid scale motions have no horizontal component across the sides of a gridbox and, by construction, the updraughts and downdraughts are exactly compensated by vertical motion in the remainder of the column (above the grid box on the Earth's surface) such that the area-averaged vertical motion at each level equals the resolved vertical motion in that gridbox ([Lock *et al.*, 2000](#); [Gregory and Rowntree, 1990](#)). The impermeability theorem of [Haynes and McIntyre \(1987\)](#) applies generally to fully compressible non-hydrostatic dynamics and implies that the cross-isentropic flux of PV must be identically zero. This applies to the resolved motions in a model and notional sub-grid transports. Furthermore, the theorem also holds for other vertical coordinates. For example, in pressure coordinates there can be no net transport of the vertical component of vorticity across pressure levels. Therefore, since the sub-grid turbulence and convective schemes describe only vertical fluxes and the non-transport of vorticity must hold, these transport schemes are not applied to the PV tracers and only advection by the resolved 3D motion transports them.

The tracer advection scheme in the MetUM also has the option to apply a conservation correction and a monotone correction; however, neither is applied to the PV tracers. The conservation correction is not applied because it is a global correction to a tracer field and will produce non-local terms in the PV tracers. A monotone correction is generally used for tracer advection of fields that are required to remain positive which is not the case for the PV tracers so it is not applied. With no corrections applied for tracer advection, the tracer advection scheme simply amounts to updating a variable with its departure point value, obtained by interpolating the tracer at time-level n to the departure point of the trajectory calculated by the semi-Lagrangian scheme of the MetUM. In this way the PV tracers method is calculating the left hand side of Eq. (1.13), partitioned by each PV tracer, at each timestep, following the resolved flow of the forecast.

Although there are no PV fluxes across isentropic surfaces, diabatic and frictional effects have an important influence on the PV distribution via diabatic mass fluxes across isentropic surfaces, horizontal divergent flow and frictional torques. Each PV tracer, apart from the advection-only PV tracer, accumulates increments in PV due a specific parametrized physical process at each timestep. The PV increment is calculated as the difference in PV before and after adding the increments to the prognostic variables. In this way the PV tracers method is calculating the right hand side of Eq. (1.13), partitioned by each parametrized physical process, at each timestep.

The slow physical processes are calculated in parallel and each increment is calculated independently using \mathbf{X}^n . The increments in PV due to slow physical processes are calculated as

$$\Delta q_{sp} = q(\mathbf{X}^n + \Delta \mathbf{X}_{sp}) - q(\mathbf{X}^n), \quad (2.15)$$

where $q(\cdot)$ means a calculation of PV as a function of the given variables in the argument and sp is microphysics, radiation or gravity-wave drag. The fast physical processes are calculated sequentially so the PV increments are calculated as

$$\Delta q_{con} = q(\mathbf{X}^{(1)} + \Delta \mathbf{X}_{con}) - q(\mathbf{X}^{(1)}), \quad (2.16)$$

for convection and

$$\Delta q_{tm} = q(\mathbf{X}^{(1)} + \Delta \mathbf{X}_{con} + \Delta \mathbf{X}_{tm}) - q(\mathbf{X}^{(1)} + \Delta \mathbf{X}_{con}), \quad (2.17)$$

for the turbulent-mixing scheme, where $q(\mathbf{X}^{(2)}) \equiv q(\mathbf{X}^{(1)} + \Delta \mathbf{X}_{con} + \Delta \mathbf{X}_{tm})$. The increment from cloud balancing is also included with the physics PV tracers, calculated as

$$\Delta q_{cloud} = q(\mathbf{X}^{(4)}) - q(\mathbf{X}^{(3)}). \quad (2.18)$$

Therefore the equations for updating the PV tracers are given by

$$q_{adv}^{n+1} = q_{adv,d}^n, \quad (2.19)$$

for the advection-only PV, where the “ d ” subscript indicates that the tracer is evaluated at departure points in the MetUM’s semi-Lagrangian scheme;

$$q_{sp}^{n+1} = (q_{sp}^n + \Delta q_{sp})_d, \quad (2.20)$$

for slow physical processes; and

$$q_{fp}^{n+1} = q_{fp,d}^n + \Delta q_{fp}, \quad (2.21)$$

for fast physical processes, where fp is convection, turbulent mixing or cloud balancing.

In the previous equations where $q(\cdot)$ is evaluated a modified version of the MetUM's standard diagnostic PV calculation has been used. PV is calculated at the corners of grid points, on model levels where ρ is stored, such that the calculation of the vertical component of vorticity requires no averaging. Each component of PV is calculated using centred differences with prognostic variables averaged when required. The result is then linearly interpolated to the centres of the grid points in the horizontal then linearly interpolated to model levels where θ is stored in the vertical. The modification is that vertical velocity components have also been included in the calculation of PV such that the PV calculated is consistent with the governing equations solved by the MetUM (non-hydrostatic deep atmosphere). The PV calculation has also been modified to include horizontal terms in the Coriolis force; however, this was done after the forecasts presented in this thesis were run. The inclusion of the horizontal Coriolis terms in the PV calculation has a negligible impact on the PV tracers in the domain investigated.

2.3 Case Studies

This section introduces the two case studies investigated in this thesis. The case studies chosen are two intense observing periods (IOPs) from the DIAMET (DIAbatic influences on Mesoscale structures in ExTratropical storms) field campaign. DIAMET was a UK project set up to investigate the effects of mesoscale processes on extratropical cyclones with the aims of improving the understanding of these processes and their representation within numerical weather prediction models ([Vaughan *et al.*, 2015](#)). The DIAMET project centered around a three week field campaign conducted during November and December of 2011. During this time period Met Office analyses were produced using the 4D-Var method documented by [Rawlins *et al.* \(2007\)](#).

2.3.1 IOP5

The first case study investigated here is IOP5. During IOP5, a cold front passed over the UK on 29 November 2011. Multiple flight legs crossed the front as it approached and passed over the UK, taking detailed observations of microphysical structures in liquid and ice phase clouds ([Lloyd *et al.*, 2014](#)). [Dearden *et al.* \(2014\)](#) used observations from IOP5

with a Lagrangian parcel model to derive diabatic heating and cooling rates in the cold front due to phase changes of water and assess their representation in parametrization schemes. IOP5 has also been used as a case study of a tornadic cold front (Clark and Parker, 2014).

The main reason for choosing IOP5 as a case study here is that IOP5 has been used to investigate the influence of diabatic processes on the tropopause (Chagnon and Gray, 2015). Chagnon and Gray (2015) showed that the diabatic PV dipole across the tropopause found by Chagnon *et al.* (2013) was robust across three case studies at various resolutions; however, for IOP5, the accumulation of positive PV in the stratosphere was much weaker than the other two case studies.

To analyse the IOP5 case study, a forecast was initialised at 12 Z on 28 November 2011 from the corresponding operational analysis and run for 36 hours. Figure 2.6 shows synoptic charts every 12 hours from Met Office analyses corresponding to IOP5. The start of the forecast corresponds to Fig. 2.6a; the region of interest is the long cold front to the west of the UK associated with the low-pressure centre near Iceland. Also of note is that the front had a double front structure further south of the cyclone and a frontal wave developing around 50° N. Over the following 12 hours the frontal wave developed into a new low pressure centre as the front approached the UK (Fig. 2.6b).

The front passed over the UK around 12 Z on the 29th (Fig. 2.11c) and reached mainland Europe in the following 12 hours (Fig. 2.11d). When the front reached the UK it was no longer diagnosed as a double front; there is a single cold front and associated pressure trough over the entire UK (Fig. 2.11c). Figure 2.7 shows satellite images at 12 Z. There is a distinct band of thick cloud associated with ascent along the front and higher cloud to the north-east of the UK associated with warm conveyor belt airstreams ascending into a ridge. In the cold sector to the west of the front, there are patches of cumulus clouds (Fig. 2.7a) as well as a dry region (Fig. 2.7b) associated with the humidity front marked by a thin line on Fig. 2.6c.

Figure 2.8 shows differences between the forecast run for this case study at 24-hours lead time and the corresponding Met Office analysis. The forecast gave a deeper trough compared to the analysis. This can be seen by the generally negative errors in low-level pressure (Fig. 2.8a) and 500 hPa height (Fig. 2.8b) around the UK, both of which have a minima to the southwest of the UK. Ridges and troughs are better seen by PV on

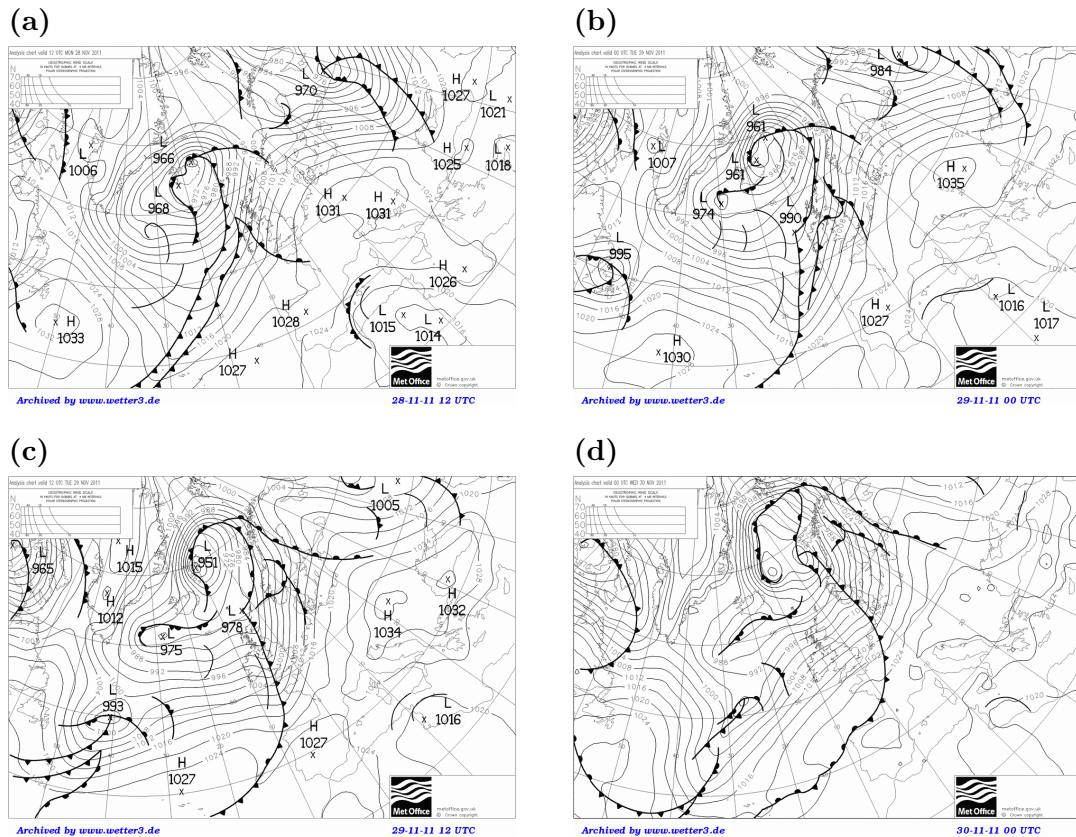


Figure 2.6: Met Office surface analysis charts for DIAMET IOP5 every 12 hours starting at (a) 12 UTC on 28 November 2011, corresponding to the initialisation of the forecast used to study IOP5.

θ . Figure 2.9 shows PV on the 320 K isentrope for the forecast and analysis: both the forecast and analysis show a distinctive trough-ridge pattern. The main difference is that the trough has expanded slightly further eastward in the forecast, indicated by the narrow positive error in PV on the leading edge of the trough, giving a deeper trough over the UK. The forecast has also produced a larger amplitude ridge than the analysis indicated by the large negative errors in PV around Scandinavia. There are also a lot of smaller positive and negative differences in PV between the forecast and analysis in the stratosphere. This is due to the analysis having a more patchy PV distribution compared to the forecast and may be an unrealistic artifact of the data assimilation system.

The exception to the deeper trough in the forecast is to the north of the UK where the low-level pressure is too high in the forecast (Fig. 2.8a) but is not seen at upper-levels (Fig. 2.8b). This is because the frontal wave seen in the analyses has not developed

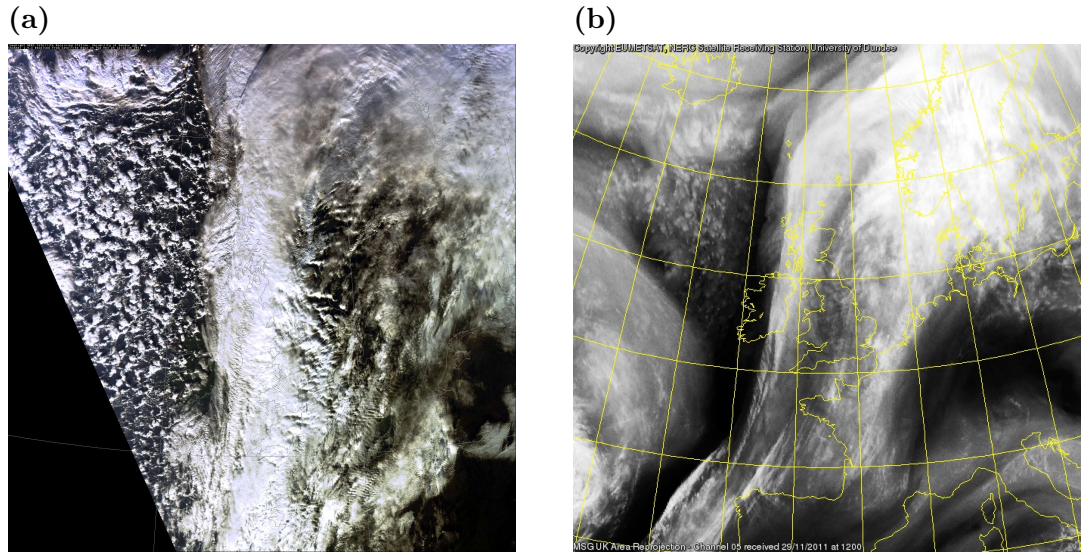


Figure 2.7: Satellite images for the IOP5 case study on 29 November 2011. (a) MODIS colour composite image from red (620-670nm), green (545-565nm) and blue (459-479nm) channels at 1232 UTC, reprojected over the UK. (b) Meteosat SEVIRI geostationary satellite mid-infrared/water vapour image (5.35-7.15 μm) at 1200 UTC, reprojected over the UK. Note that the two projections are different. Images archived by the NERC Satellite Receiving Station, Dundee University, Scotland (<http://www.sat.dundee.ac.uk/>).

in the forecast. This can be seen if we look at the low-level θ distribution (Fig. 2.10). The forecast reproduces the location and intensity of the front in the analysis with small differences in θ around the region of the front. The exception is north of the UK where the forecast θ is colder than the analysis due to the cold front advancing further in the forecast. The isotherms in this region in the forecast are roughly straight whereas the isotherms in the analysis have a bend because of the developing low pressure centre.

2.3.2 IOP8

The second case study investigated here is IOP8. IOP8 corresponds an intense extratropical cyclone with strong winds over Scotland on 8 December 2011. The main interest in IOP8 for the field campaign was the association of the intense winds with a sting jet which were observed in-situ with the research aeroplane (Baker *et al.*, 2013). IOP8 has been used for developing sting-jet detection techniques by defining sting-jet air streams in terms of trajectories (Martínez-Alvarado *et al.*, 2014a; Hart *et al.*, 2015). IOP8 has also

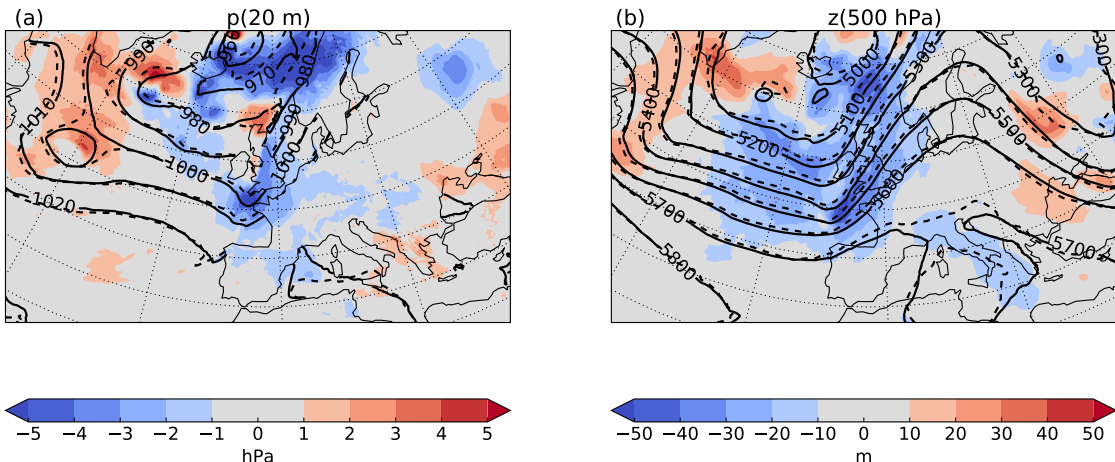


Figure 2.8: Forecast minus analysis errors for the forecast run for the IOP5 case study at 24-hours lead time (12 UTC on 29 November 2011). (a) Pressure on the lowest model θ -level (20 m; contours masked over land). (b) 500 hPa height. Solid lines show the forecast, dashed lines show the analysis and colours show the forecast minus analysis.

been used as a case study of a non-tornadic cold front in the same study as IOP5 ([Clark and Parker, 2014](#)).

To analyse the IOP8 case study, a forecast was initialised at 12 Z on 7 December 2011 from the corresponding operational analysis and run for 36 hours. Figure 2.11 shows synoptic charts every 12 hours from the Met office analyses corresponding to IOP8. The start of the forecast corresponds to Fig. 2.11a. The initial cyclone can be seen as the 1001 hPa low pressure system developing in a trough in the Atlantic. The front had started to wrap up with a distinct cold and warm front meeting at the low pressure centre. Over the next 12 hours the cyclone developed rapidly as seen in Fig. 2.11b where the central pressure had dropped by 24 hPa and the cyclone had developed the “T-bone” structure distinctive of intense extratropical cyclones ([Shapiro and Keyser, 1990](#)).

The strongest winds occurred over Scotland around 12 Z on the 8th ([Baker *et al.*, 2013](#)) (24-hours lead time). By this time the cyclone had deepened by a further 20 hPa and the warm front had wrapped around the cyclone centre (Fig. 2.11c). The cyclone did not deepen further as it passed over Scotland (Fig. 2.11d). Figure 2.12 shows satellite images at 12 Z. The satellite images show features distinctive of extratropical cyclones: cloudy air along the trailing cold front, a cloud head wrapped around the low-pressure centre and a dry intrusion from descending air being wrapped into the cyclone centre. Also of

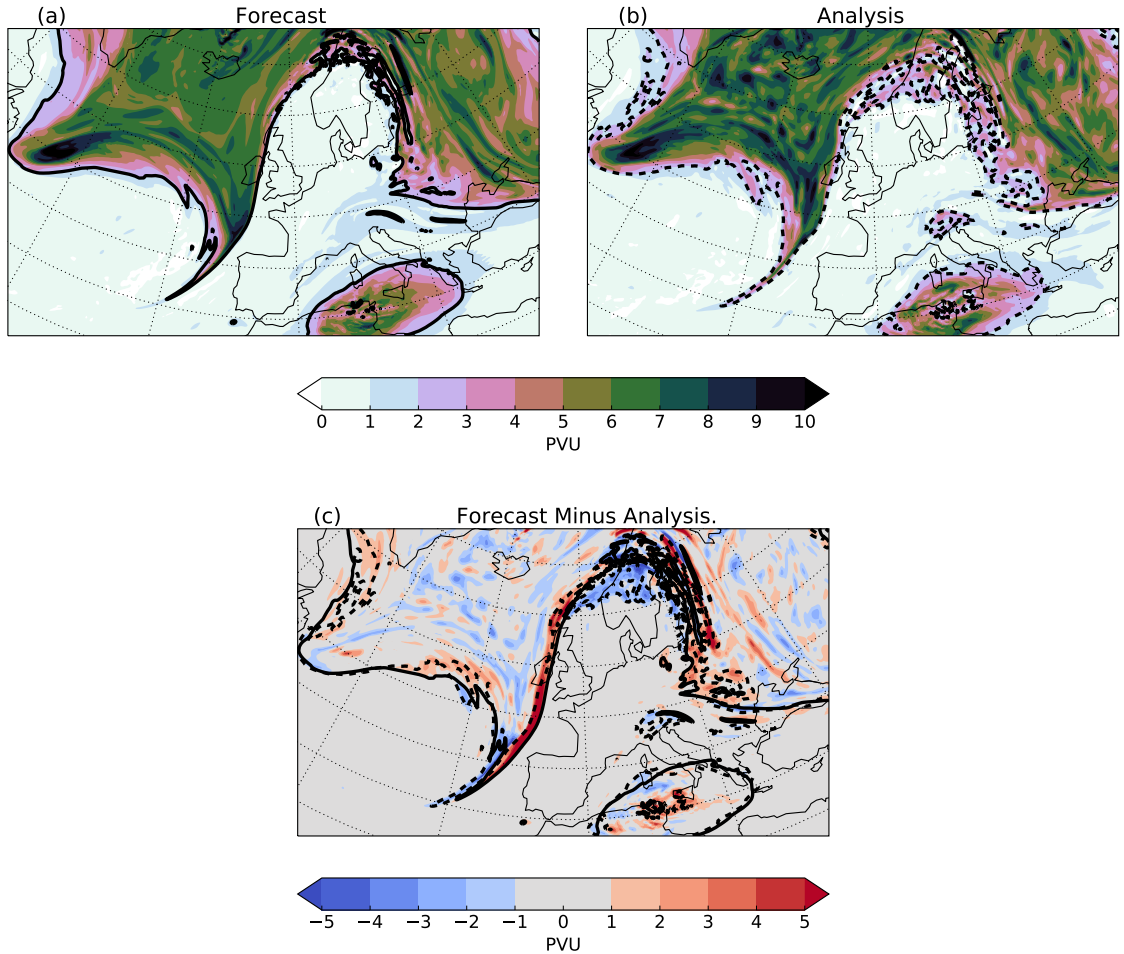


Figure 2.9: PV on 320 K for the IOP5 case study at 12 UTC on 29 November 2011. (a) Forecast at 24-hours lead time. (b) Corresponding analysis. (c) Forecast minus analysis. Contours highlight 2-PVU for the forecast (solid) and analysis (dashed).

note is the cloud banding in the air wrapping into the cyclone centre (Fig. 2.12a), which is an expected signature of sting-jet airstreams (Browning, 2004).

Figure 2.8 shows differences between the forecast and analyses. The forecast reproduced the structure and intensity of the cyclone with good accuracy. The main errors are dipole-like around the cyclone centre in both low-level pressure (Fig. 2.13a) and 500 hPa height (Fig. 2.13b) indicating that the main error is a small displacement of the cyclone in the forecast relative to the analysis. This can be seen in the low-level wind speeds (Fig. 2.14): the forecast reproduced the intense wind speeds in the analysis but displaced slightly south-eastward.

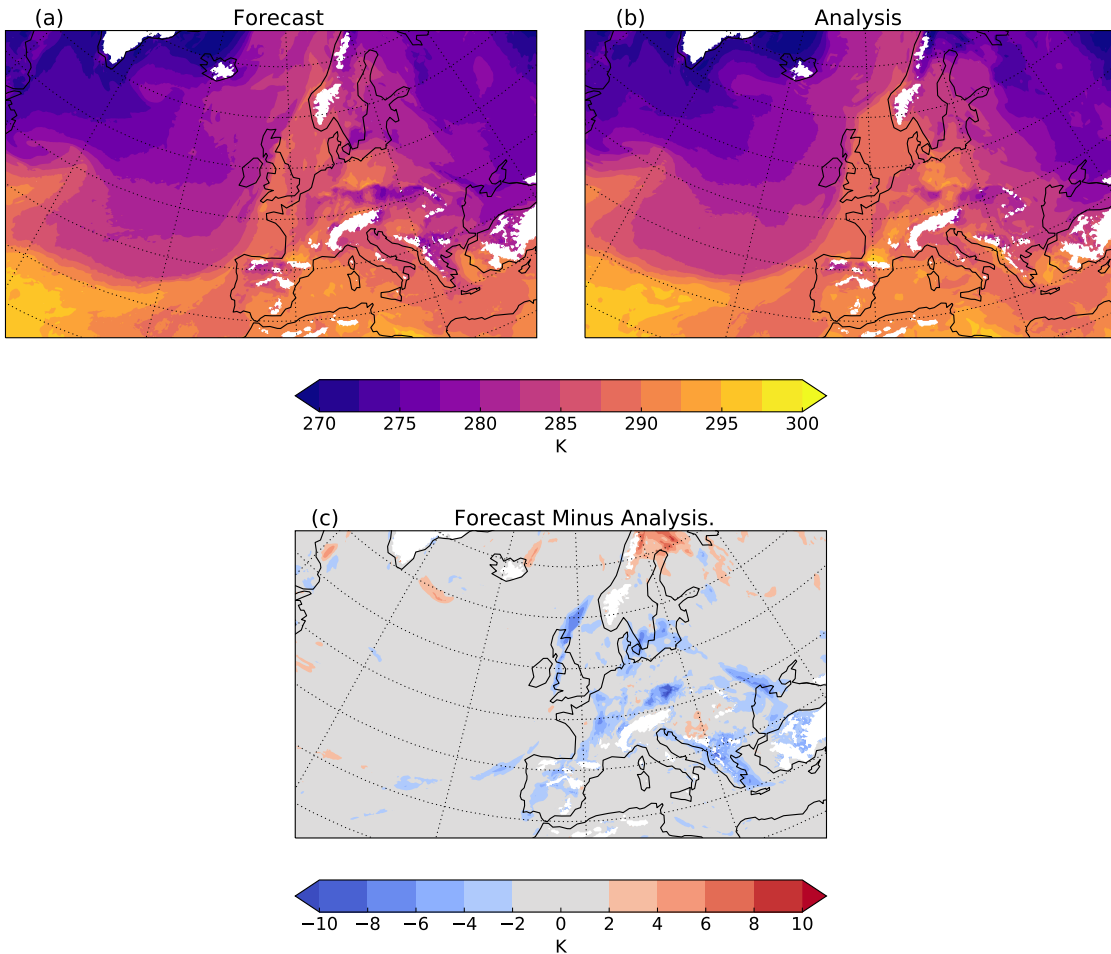


Figure 2.10: θ at 900 hPa for the IOP5 case study at 12 UTC on 29 November 2011. (a) Forecast at 24-hours lead time. (b) Corresponding analysis. (c) Forecast minus analysis.

2.4 Winter Season

This section describes a set of forecasts over a winter season investigated in this thesis. By compositing forecast errors over many forecasts, systematic forecast errors can be identified and related to model errors. The initial tendencies method (see section 1.5.2) relates the systematic forecast errors of short forecasts to the initial imbalance of model processes (Klinker and Sardeshmukh, 1992; Rodwell and Palmer, 2007). By integrating the PV tracers over many forecasts, the systematic effects of model processes can be diagnosed and linked to systematic forecast errors, and as a result, associated with model errors.

The period chosen is the 2013/14 winter season. The 2013/14 winter season was notable for large accumulations of precipitation in the UK due to an increased frequency

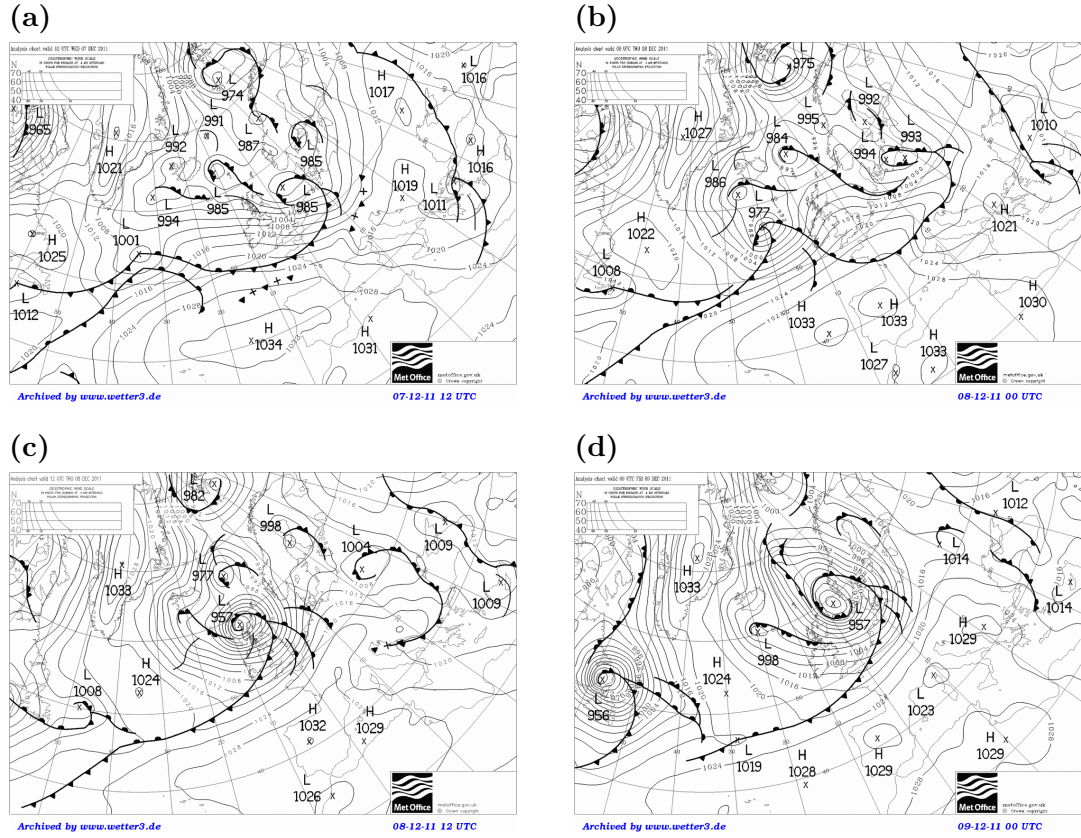


Figure 2.11: Met Office surface analysis charts for DIAMET IOP8 every 12 hours starting at (a) 12 UTC on 7 December 2011, corresponding to the initialisation of the forecast used to study IOP8.

of storms, although few of those individual events were extreme (Kendon and McCarthy, 2015). Priestley *et al.* (2017) attributed the increased frequency of storms over the UK to an anomalously strong and persistent jet stream driven by increased Rossby wave breaking to the north and south of the jet.

To study the 2013/14 winter season, a forecast was initialised for each day in the three-month winter period from 1 November 2013 to 31 January 2014 (a total of 92 forecasts). Each forecast was initialised at 00 UTC using operational analyses and run for 2.5 days to give an overlap between forecasts. During this time period Met Office analyses were produced using the hybrid ensemble/4D-Var method documented by Clayton *et al.* (2013). The Met Office phased out operational use of the NAE domain beyond 31 January 2014 which is why November has been used instead of February for the “winter” season.

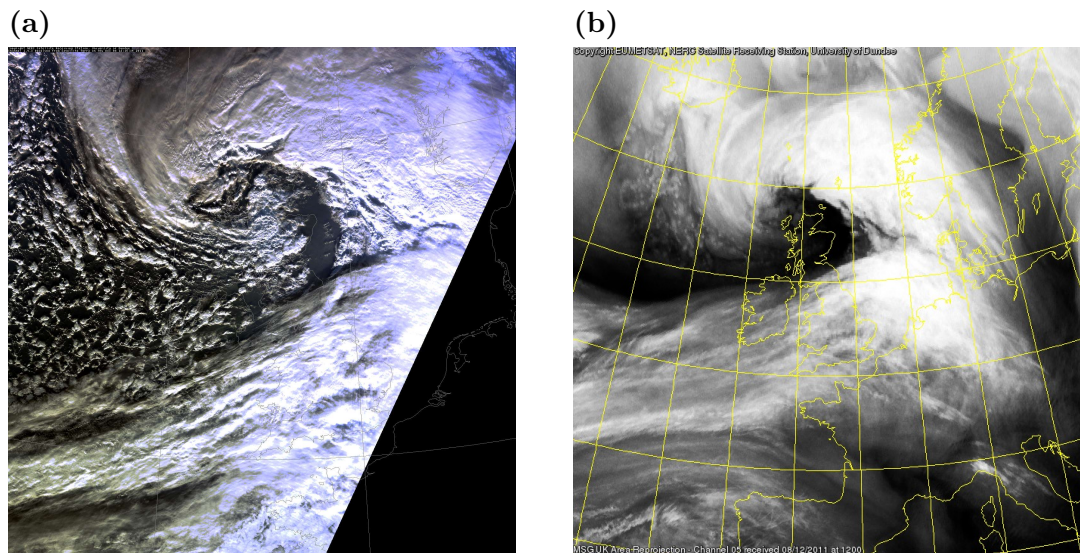


Figure 2.12: Satellite images for the IOP8 case study on 8 December 2011. (a) MODIS colour composite image from red (620-670nm), green (545-565nm) and blue (459-479nm) channels at 1215 UTC, reprojected over the UK. (b) Meteosat SEVIRI geostationary satellite mid-infrared/water vapour image (5.35-7.15 μm) at 1200 UTC, reprojected over the UK. Note that the two projections are different. Images archived by the NERC Satellite Receiving Station, Dundee University, Scotland (<http://www.sat.dundee.ac.uk/>).

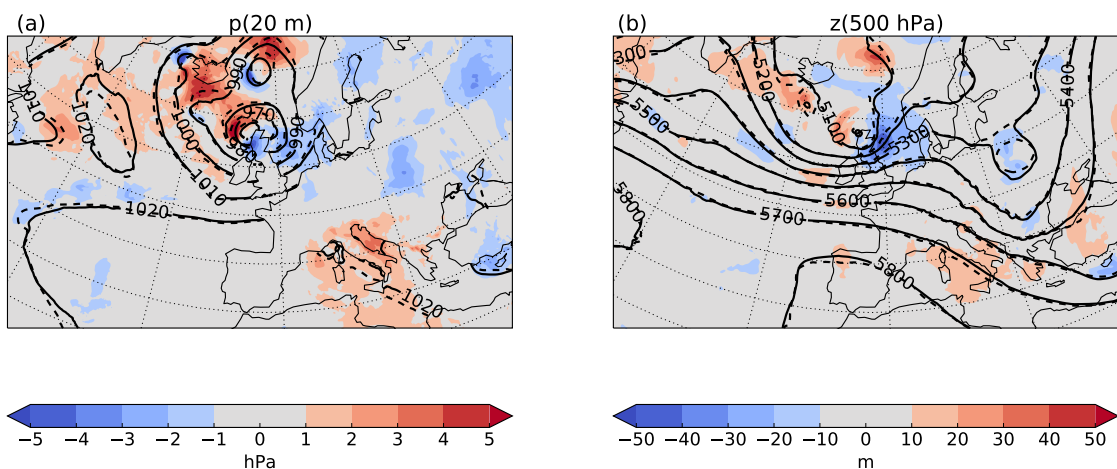


Figure 2.13: Forecast minus analysis errors for the forecast run for the IOP8 case study at 24-hours lead time (12 UTC on 8 December 2011). (a) Pressure on the lowest model θ -level (20 m). (b) 500 hPa height. Solid lines show the forecast, dashed lines show the analysis and colours show the forecast minus analysis.

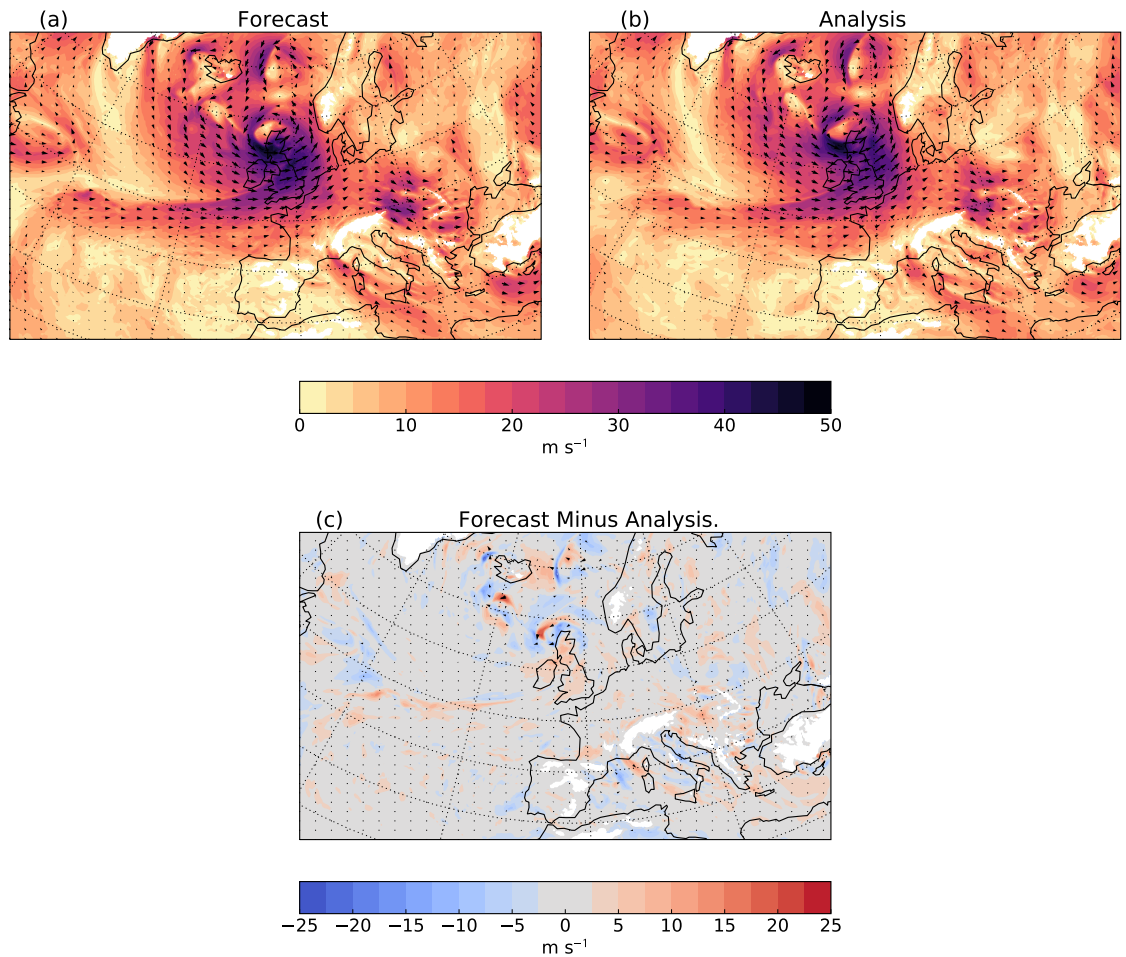


Figure 2.14: Wind speed at 1 km for the IOP8 case study at 12 UTC on 8 December 2011. (a) Forecast at 24-hours lead time. (b) Corresponding analysis. (c) Forecast minus analysis.

Chapter 3

Dynamics-tracer Inconsistency

3.1 Introduction

Considering the PV conservation in a numerical model of the atmosphere [Davis *et al.* \(1993\)](#) partitioned PV into a set of tracer diagnostics to explicitly integrate the cumulative effects of parametrized physical processes in a study of cyclogenesis. Combined with the piecewise PV inversion method of [Davis and Emanuel \(1991\)](#) this allowed them to assess the impact of non-conservative processes on a cyclone's circulation. The PV tracers did have limitations: [Davis *et al.* \(1993\)](#) noted differences between the PV tracers and the PV diagnosed from model variables and attributed this to numerical truncation errors in updating PV. [Stoelinga \(1996\)](#) discussed this difference in more detail and attributed it to the difference between the explicit PV integration and the model dynamics which are not designed to conserve PV exactly.

[Zhang *et al.* \(2008\)](#) demonstrated that inconsistencies between tracer advection and the dynamical core of an atmospheric model can produce significant biases in modelling chemical transport. [Whitehead *et al.* \(2015\)](#) assessed the consistency of several dynamical cores with their respective tracer advection schemes by investigating PV in an idealised baroclinic wave test. In this test there is no diabatic heating or friction: the only source of PV non-conservation is dissipation, implicit or explicit, induced by the dynamical core. [Whitehead *et al.* \(2015\)](#) tested the consistency of this dissipation with the dissipation induced by the tracer advection scheme for a range of dynamical cores and demonstrated that each dynamical core produces values of PV inconsistent with the tracer advection scheme but with structure and amplitude differing between dynamical cores. [Whitehead *et al.* \(2015\)](#) used the consistency between a dynamical PV and a tracer of PV to rank the different dynamical cores.

Tracers of PV have been used for two things: assessing the dynamical impacts of parametrized physical processes and diagnosing inconsistencies between dynamical cores

and tracer advection schemes. This chapter demonstrates that, by extending the PV tracer diagnostics of [Davis et al. \(1993\)](#), the inconsistency in PV (defined by [Whitehead et al. \(2015\)](#)) can be diagnosed in a simulation which also has parametrized physical processes. It is shown that this “dynamics-tracer inconsistency” is comparable to the effects on PV of parametrized physical processes for the IOP5 case study and that the majority of the “dynamics-tracer inconsistency” in the MetUM can be attributed to non-conservation of PV by the dynamical core.

The structure of this chapter is as follows. In section 3.2 the residual in the PV tracers budget is demonstrated for the IOP5 case study and the reasons for this residual are identified. In section 3.2.1 an exact budget of PV, in the context of the PV tracers, is outlined. For the in-depth description of the PV tracers in the MetUM see section 2.2.2. In section 3.2.2 the dynamics-tracer inconsistency term, derived in section 3.2.1, is quantified for the IOP5 case study. In section 3.2.3 it is shown that the non-conservation of PV by the dynamical core of the MetUM is the dominant contribution to dynamics-tracer inconsistency. In section 3.2.4 the non-conservation of PV by the dynamical core is considered in the context of the diabatically generated PV dipole identified by [Chagnon et al. \(2013\)](#). A summary and discussion of results is presented in section 3.3.

3.2 Results

If all processes modifying PV were accounted for by the PV tracers then the accumulated effects of parametrized physical processes ($\sum q_{phys}$) would be equivalent to the total change in PV given by the diagnosed PV minus the advection-only PV ($q - q_{adv}$). A parameter (ε) is defined as the difference between these two measures of PV change, such that

$$\varepsilon^n = q^n - q_{adv}^n - \sum q_{phys}^n, \quad (3.1)$$

where $q^n \equiv q(\mathbf{X}^n)$ is the diagnosed PV. Note that ε is the same as q_r in [Stoelinga \(1996\)](#).

Figure 3.1b shows ε and Fig. 3.1a shows the sum of physics PV tracers for comparison, each at the end of the 36 h forecast interpolated to the 320 K isentropic surface. The field of ε has structure and amplitude that is comparable to the sum of physics PV tracers and therefore represents an important contribution to the PV budget.

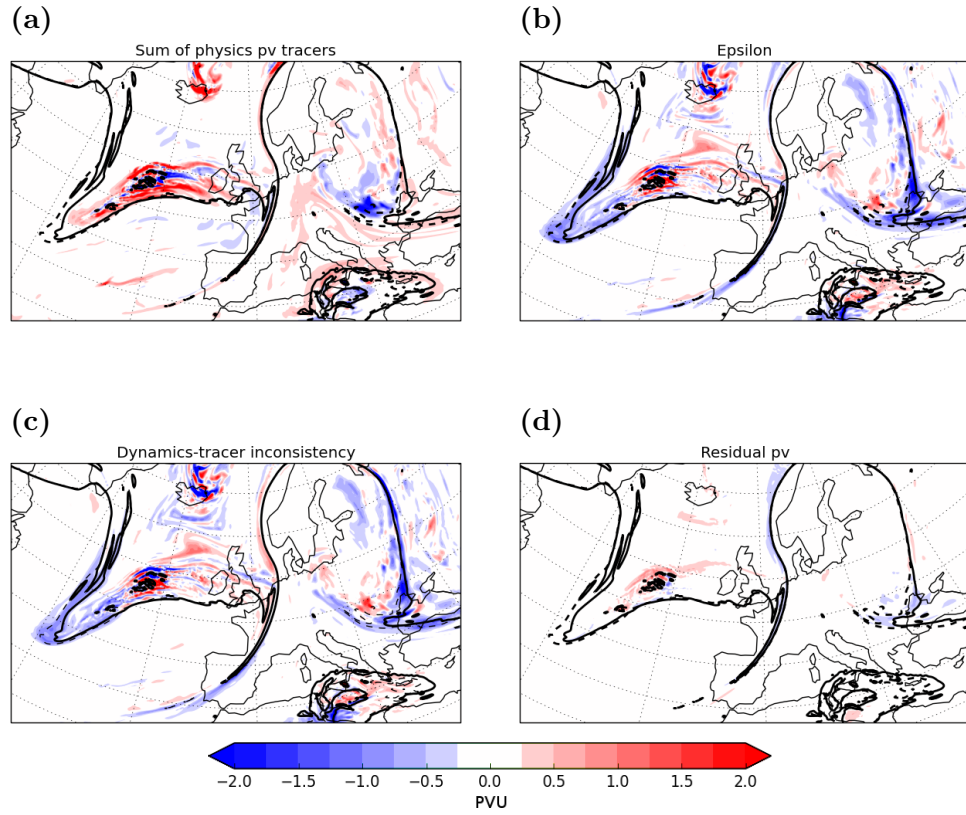


Figure 3.1: Terms in the PV budget for the forecast run for the IOP5 case study at 36-hours lead time (00 UTC on 30 November 2011). All plots show variables linearly interpolated to the 320 K isentrope. (a) The sum of the physics PV tracers ($\sum q_{phys}$). (b) ε as defined by Eq. (3.1). (c) Dynamics-tracer inconsistency. (d) The residual in the PV budget (ε_r in Eq. (3.16)). The thick black line in each plot is the 2 PVU line of the diagnosed PV and the dashed line is the 2 PVU line of the advection-only PV tracer

3.2.1 PV Budget

In this section, by considering the evolution of the PV budget across a timestep, it is shown that ε is completely accounted for by three terms: “dynamics-tracer inconsistency” ($\Delta\varepsilon_I$) to be defined below based on the inconsistency investigated by Whitehead *et al.* (2015); “missing PV” ($\Delta\varepsilon_M$) which accounts for any increments in PV not attributed to a dynamical or physical process; and a “splitting error” ($\Delta\varepsilon_S$) which accounts for the difference between numerical diffusion acting on multiple tracers of PV and the numerical diffusion acting on a single field representing the sum of those PV tracers. In this section, these three terms are defined by their numerical form in the MetUM. In principle a PV budget for any numerical model of the atmosphere could be closed using just these three

terms.

To calculate a closed PV budget all changes in PV across a single timestep must be accounted for, such that the PV at time-level $n+1$ is equal to the PV at time-level n plus all the changes in PV in that timestep. Considering every change in PV across a single timestep of the MetUM (as in Fig. 2.5) gives:

$$\begin{aligned} q^{n+1} = q^n &+ \{q(\mathbf{X}^{sl}) - q(\mathbf{X}^n)\} + \{q(\mathbf{X}^{(1)}) - q(\mathbf{X}^{sl})\} \\ &+ \{q(\mathbf{X}^{(2)}) - q(\mathbf{X}^{(1)})\} + \{q(\mathbf{X}^{(3)}) - q(\mathbf{X}^{(2)})\} \\ &+ \{q(\mathbf{X}^{(4)}) - q(\mathbf{X}^{(3)})\}. \end{aligned} \quad (3.2)$$

Each of the terms in Eq. (3.2) can be attributed to increments in PV related to dynamical and physical processes. The first increment in PV in Eq. (3.2) ($q(\mathbf{X}^{sl}) - q(\mathbf{X}^n)$) is a result of the semi-Lagrangian dynamics, which can be defined as Δq_{sl} , such that

$$q(\mathbf{X}^{sl}) - q(\mathbf{X}^n) = \Delta q_{sl}. \quad (3.3)$$

The next increment in PV in Eq. (3.2) ($q(\mathbf{X}^{(1)}) - q(\mathbf{X}^{sl})$) is a result of adding the increments to prognostic variables from the slow physical processes to the latest estimate of \mathbf{X} . This is approximately equivalent to updating the slow physics PV tracers:

$$q(\mathbf{X}^{(1)}) - q(\mathbf{X}^{sl}) \approx \sum (q_{sp}^n + \Delta q_{sp})_d - \sum q_{sp,d}^n, \quad (3.4)$$

where $\sum q_{sp}$ is the set of PV tracers for slow physical processes. The equation is not exact because of the nonlinearity associated with the calculation of the PV increments due to slow physical processes (Eq. (2.15)) in parallel and the order in which the increments are added. The next increment in PV in Eq. (3.2),

$$q(\mathbf{X}^{(2)}) - q(\mathbf{X}^{(1)}) = \Delta q_{con} + \Delta q_{bl}, \quad (3.5)$$

is the increment in PV due to the fast physical processes (Eqs. (2.16) and (2.17)). The next increment in PV in Eq. (3.2) ($q(\mathbf{X}^{(3)}) - q(\mathbf{X}^{(2)})$) is a result of the pressure solver, which can be defined as Δq_{solver} , such that

$$q(\mathbf{X}^{(3)}) - q(\mathbf{X}^{(2)}) = \Delta q_{solver}. \quad (3.6)$$

The final increment in PV in Eq. (3.2),

$$q(\mathbf{X}^{(4)}) - q(\mathbf{X}^{(3)}) = \Delta q_{cloud}, \quad (3.7)$$

is the increment in PV due to cloud balancing (Eq. (2.18)). The increments due to fast physical processes can be defined as,

$$\sum \Delta q_{fp} = \Delta q_{con} + \Delta q_{bl} + \Delta q_{cloud}. \quad (3.8)$$

The increment due to cloud balancing Δq_{cloud} has been grouped with fast physical processes for convenience.

Whitehead *et al.* (2015) define the inconsistency between a dynamical core and tracer advection as the difference between the evolution of PV calculated by integrating the governing equations in a dynamical core and the advection of a tracer of PV. We can define this “dynamics-tracer inconsistency” for a single timestep as $\Delta\varepsilon_I$ by comparing PV obtained by solving the adiabatic and frictionless governing equations ($q^n + \Delta q_{sl}$) with PV advected using the tracer advection scheme (q_d^n), such that

$$\Delta\varepsilon_I = (q^n + \Delta q_{sl}) - q_d^n. \quad (3.9)$$

Ideally the increment in PV due to the pressure solver from Eq. (3.6) would be included because the pressure solver involves the solution of the continuity equation and the back-substitution to complete the solution of the thermodynamic and momentum equations. However, the pressure solver also couples the parametrized physics to the dynamics so it is not completely attributable to adiabatic and frictionless dynamics.

With all increments in PV described in terms of dynamics and physics, Eq. 3.9 can be used to rewrite Eq. (3.2) as

$$q^{n+1} = q_d^n + \sum (q_{sp}^n + \Delta q_{sp})_d - \sum q_{sp,d}^n + \sum \Delta q_{fp} + \Delta\varepsilon_I + \Delta\varepsilon_M, \quad (3.10)$$

where $\Delta\varepsilon_M$ is the “missing PV” and includes the increment in PV due to the pressure solver as well as accounting for the nonlinearity in the calculations of PV increments due to slow physical processes from Eq. (3.4).

Rearranging Eq. (3.1) for time level $n + 1$ gives

$$q^{n+1} = q_{adv}^{n+1} + \sum q_{sp}^{n+1} + \sum q_{fp}^{n+1} + \varepsilon^{n+1}, \quad (3.11)$$

and

$$q_d^n = (q_{adv}^n + \sum q_{sp}^n + \sum q_{fp}^n + \varepsilon^n)_d, \quad (3.12)$$

The terms describing PV tracers in Eq. (3.10) can be eliminated using the definitions of PV tracer updates (Eqs (2.19), (2.20) and (2.21)). However, the difference between numerical diffusion acting on multiple tracers of PV and the numerical diffusion acting on a single field representing the sum of those PV tracers, highlighted by the placement of the d subscript in Eq. (3.12), must be accounted for first. This “splitting error” is a result of diffusion in the tracer advection scheme which is entirely implicit for the operational MetUM and in the simulation performed here. We define the “splitting error” as

$$\Delta\varepsilon_S = q_d^n - (q_{adv,d}^n + \sum q_{sp,d}^n + \sum q_{fp,d}^n + \varepsilon_d^n). \quad (3.13)$$

Now, all terms describing PV tracers in Eq. (3.10) can be eliminated using Eqs (3.11), (3.12) and (3.13) and the definitions given by Eqs (2.19), (2.20) and (2.21), which gives the result

$$\varepsilon^{n+1} = \varepsilon_d^n + \Delta\varepsilon_I + \Delta\varepsilon_M + \Delta\varepsilon_S. \quad (3.14)$$

Since ε is by definition zero everywhere at the start of a forecast, Eq. (3.14) tells us that the gap in the PV budget can only be due to the accumulation of the three terms defined in this section: “dynamics-tracer inconsistency” ($\Delta\varepsilon_I$), “missing PV” ($\Delta\varepsilon_M$) and a “splitting error” ($\Delta\varepsilon_S$) and modifications due to the implicit diffusion of ε from carrying it forward on departure points in Eq. (3.14).

3.2.2 Dynamics-tracer Inconsistency

The previous derivation allows us to describe ε completely as the accumulation of three terms: dynamics-tracer inconsistency; missing changes in PV across a single timestep; and the difference between advecting a single tracer of PV and advecting multiple tracers of PV. In this section it will be shown that dynamics-tracer inconsistency is the dominant contribution to ε .

The dynamics-tracer inconsistency is calculated in the MetUM at each timestep using Eq. (3.9) and then accumulated in the same way as a PV tracer:

$$\varepsilon_I^{n+1} = \varepsilon_{I,d}^n + \Delta\varepsilon_I. \quad (3.15)$$

The residual of the PV budget is calculated as

$$\varepsilon_r^n = \varepsilon^n - \varepsilon_I^n, \quad (3.16)$$

and can only be due to the “missing PV” and the “splitting error” (i.e. the time integral of $\Delta\varepsilon_M + \Delta\varepsilon_S$). Figure 3.1 shows the integrated dynamics-tracer inconsistency (ε_I) and the residual PV (ε_r) for a 36 hour forecast. Dynamics-tracer inconsistency accounts for most of ε and the residual PV is generally more than an order of magnitude smaller than ε and has smaller-scale structure. Therefore, the pressure solver and nonlinearities in calculations of PV increments ($\Delta\varepsilon_M$) and the “splitting error” ($\Delta\varepsilon_S$) are comparatively small contributions to the PV budget for this case study.

3.2.3 Non-conservation of PV by the Dynamical Core

In this section, it is shown that the dominant process contributing to dynamics-tracer inconsistency is the non-conservation of PV by the dynamical core rather than the numerical dissipation of a PV tracer in the tracer advection scheme. It has already been shown that $\Delta\varepsilon_S$ is a small contribution to the PV budget which tells us that the numerical diffusion acting on multiple tracers of PV is approximately the same as the numerical diffusion acting on a single field representing the sum of those PV tracers. In this section it is shown that the numerical dissipation of a single tracer of PV is small compared to the dynamics-tracer inconsistency.

What is the true change in PV integrated along the resolved flow of the forecast? Dynamics-tracer inconsistency arises both from non-conservation of PV by the dynamical core and the numerical dissipation in the tracer advection scheme. If the tracer advection scheme were perfectly conservative, the total change in PV following an air-mass would be the difference between the diagnosed PV and the PV from the origin of the trajectory that the air-mass followed through the whole forecast ($q - q_{origin}$). Including the PV at the origin of trajectories in the PV budget (Eq. (3.1)) gives

$$\varepsilon^n = (q^n - q_{origin} - \sum q_{phys}^n) + (q_{origin} - q_{adv}^n), \quad (3.17)$$

which highlights a notional partition between non-conservation of PV by the dynamical core (the left bracket) and non-conservation associated with numerical dissipation in the tracer advection scheme acting on the advection-only PV tracer (right bracket). To estimate the relative magnitudes of these two contributions, trajectories were released from a regular grid on the 500 hPa surface at the end of the forecast (T+36) and calculated backwards in time to the start of the forecast using the trajectory calculation method of Wernli and Davies (1997) (LAGRANTO, Sprenger and Wernli (2015)) with hourly

3D wind output from the MetUM. The initial PV field is interpolated to each trajectory location at $t = 0$, providing an estimate of q_{origin} which can be associated with the grid point that the trajectory “arrives on” at the end of the forecast. This technique is called a “reverse domain filling” (RDF) trajectory calculation since a map of $q_{\text{origin}}(\mathbf{x})$ is obtained (Fig. 3.2c). Since the forecast is run using a limited-area domain, any trajectories that leave the domain are given the value of the advection-only PV tracer at the last point they are in the domain instead of an unknown $t = 0$ value.

Figure 3.2 compares three different measures of PV: the diagnosed PV (q), the advection-only PV (q_{adv}), and the PV calculated from RDF trajectories (q_{origin}). The fields are shown at 500 hPa because the back trajectory calculations were initialised on pressure levels. The 500 hPa surface is found using linear interpolation while assuming a logarithmic variation of pressure with height, consistent with other MetUM diagnostics. Owing to the exact conservation implied by the RDF technique, the maxima and minima in the field are given by the extrema in the initial PV distribution (at the origin locations which in general are not at 500hPa due to vertical motion). Fine scales are generated through stirring by advection and there is no dissipation in the reverse domain filling calculation to smooth the small-scale structure. In contrast the advection-only tracer experiences numerical diffusion. This acts to remove the smallest structures and to fill in some regions with intermediate PV values (for example, around the cyclonic spiral to the southwest of Iceland in Fig. 3.2). The highest PV values in RDF PV over southern England are also reduced in the PV tracer, presumably by mixing in the tracer calculation. In contrast, the diagnosed PV (from the prognostic variables) shows much lower values than q_{adv} or q_{origin} within the low PV air to the south of Iceland. Part of this difference is associated with physical processes and part with the non-conservation by the dynamical core.

Figure 3.3 shows ε calculated from Eq. (3.1) and ε calculated from the first bracket in Eq. (3.17) using the RDF estimate q_{origin} . There are considerable differences between the two terms, mainly in terms of fine-scale structure fluctuating about zero. As already discussed the fine scale structure arises from lack of dissipation in the RDF calculation and also small errors associated with the offline calculation of long trajectories used in the RDF calculation. However, it can be seen that ε calculated from RDF trajectories accounts for most of the larger scale and magnitude PV anomalies seen in ε calculated

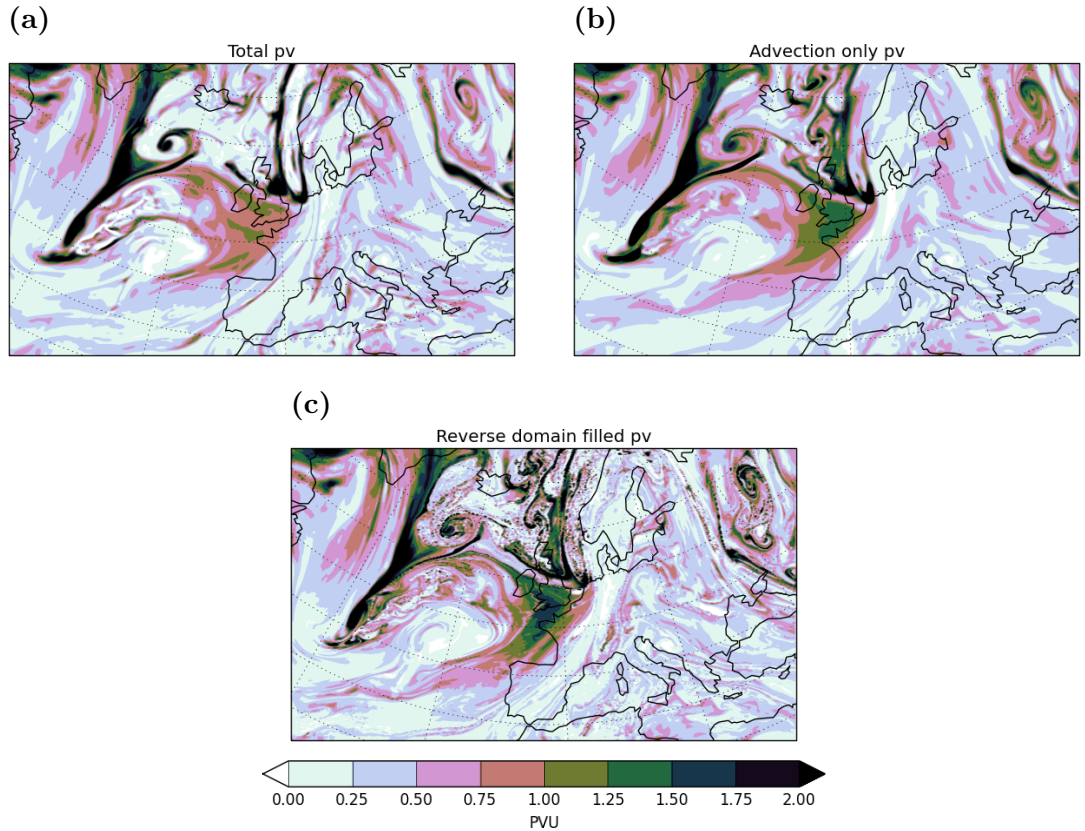


Figure 3.2: Different measures of PV at 500 hPa for the forecast run for the IOP5 case study at 35-hours lead time (23 UTC on 29 November 2011). (a) Diagnosed PV. (b) Advection-only PV tracer. (c) PV from reverse domain filling trajectories.

from Eq. (3.1). Therefore, we can conclude that numerical diffusion of the advection-only PV tracer is not the major contribution to the dynamics-tracer inconsistency in ε .

Tracer advection within the MetUM has the option to run with various different interpolation schemes. Running the same simulation while varying the interpolation scheme used for the PV tracers from linear to quintic makes very little difference to the dynamics-tracer inconsistency (not shown). This suggests that the numerical diffusion of the PV tracers associated with the interpolation to departure points in the semi-Lagrangian advection scheme is not the major contribution to the dynamics-tracer inconsistency.

Having eliminated other options, the conclusion is that the tracer advection used for the PV tracers is more conservative, in terms of PV, than the dynamical core. The majority of the dynamics-tracer inconsistency must therefore be due to the non-conservation of PV by the dynamical core.

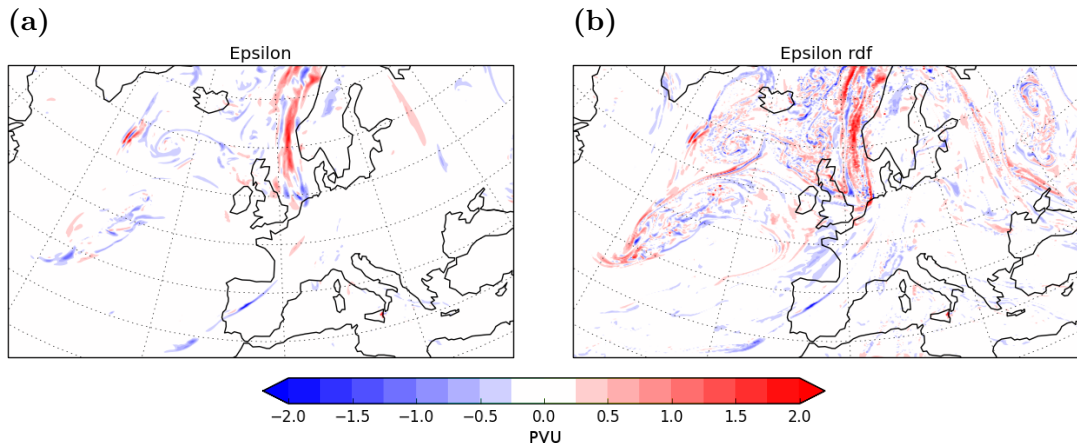


Figure 3.3: The difference between the accumulated effects of parametrized physical processes ($\sum q_{phys}$) and the total change in PV calculated using (a) advection-only PV (q_{adv}) and (b) PV traced back along a trajectory (q_{origin}), at 500 hPa for the forecast run for the IOP5 case study at 35-hours lead time (23 UTC on 29 November 2011).

How should this non-conservation of PV by the dynamical core be interpreted? Like PV, θ is conserved in the absence of diabatic and frictional processes. Therefore it can be partitioned into a set of tracers in the same way as PV (Martínez-Alvarado and Plant, 2014) and will also have an associated dynamics-tracer inconsistency. However, θ is a prognostic variable in the MetUM so the changes to θ in the dynamical core are essentially identical to tracer advection (depending on the interpolation schemes used). The dynamics-tracer inconsistency for θ (calculated with Eq. (3.9)) would therefore be close to zero and tests have shown it is close to zero (Martínez-Alvarado, personal communication).

If the same study as Whitehead *et al.* (2015) were run with the MetUM, there would be different answers depending on whether PV or θ is used. The prognostic variable θ tells us that the MetUM has a consistent dynamical core and tracer advection scheme; however, the diagnostic variable PV shows a large dynamics-tracer inconsistency. PV is diagnosed as a function of the gradients of the prognostic variables, each of which are updated separately (Eq. (2.6)). Therefore the Lagrangian equation for PV (Eq. (1.13)) is not respected exactly by the dynamical core of the MetUM. The dissipation of prognostic variables θ and \mathbf{u} in the dynamical core will act like the effects of heating and friction terms on PV.

The straining flow of the atmosphere results in a tracer cascade to smaller scales

by conservative advection of PV; however, exact conservation of PV is not necessarily a desirable property of a dynamical core because the cascade to smaller scales will be blocked at the grid-scale (Thuburn, 2008). The non-conservation of PV by the dynamical core can be associated with an implicit representation of small-scale dissipation. Kunkel *et al.* (2014) used a PV tracer in an adiabatic and frictionless simulation to assess the impact of inertia-gravity waves near the tropopause. Kunkel *et al.* (2014) found systematic differences between the diagnosed PV and tracer PV in the regions of inertia-gravity waves. Small-scale physical processes would act to modify PV but should not be expected to modify passive tracers in the same way.

3.2.4 Tropopause Dipole

Using the PV tracers method Chagnon *et al.* (2013) showed that the accumulated effects of parametrized physical processes contributed to a sharpening of the tropopause PV gradient for a case study of an extratropical cyclone. In this section the effects of the non-conservation of PV by the dynamical core on the tropopause PV gradient are investigated for this case study.

Chagnon *et al.* (2013) showed, for their case study, that the 2 PVU surface of the advection-only PV tracer coincided with the 2 PVU surface of the diagnosed PV. This meant that the direct modifications of PV by non-conservative processes did not act to change the position of the tropopause. By summing the values of the near-tropopause PV changes ($q - q_{adv}$), binned by the advection-only PV tracer, Chagnon *et al.* (2013) showed that the average change in PV for initially tropospheric air ($q_{adv} < 2$) was negative and the average change in PV for initially stratospheric air ($q_{adv} > 2$) was positive with a zero value at 2 PVU (Fig. 6 in Chagnon *et al.* (2013)). Chagnon and Gray (2015) repeated this diagnostic for three more extratropical cyclones and showed that the IOP5 case study (case II in Chagnon and Gray (2015)) contains regions of tropopause sharpening but with a weaker tropopause dipole on average due to weaker positive PV tendencies on the stratospheric side of the tropopause.

Figure 3.4a shows the same diagnostic as Fig. 6 in Chagnon *et al.* (2013) but integrated over many vertical levels by weighting the gridpoints by mass, rather than an area average over individual vertical levels, with Fig 3.4b showing the total mass associated with each bin. The diagnostic was integrated over many vertical levels to include any shallow PV

anomalies that may be important. Only gridpoints within 2.5 km in the vertical of the tropopause are included, excluding the boundary layer using the MetUM's diagnosis of boundary layer height. The mean mass of the included gridpoints is 3.18×10^{10} kg, with a maximum of 4.21×10^{10} Kg and a minimum of 5.69×10^9 Kg.

[Whitehead et al. \(2015\)](#) found large amounts of dynamics-tracer inconsistency where isentropes intersected the ground. This is also true for the PV tracers shown here; however, this low-level “dynamics-tracer” inconsistency is found to largely cancel out tendencies between the radiation and boundary layer parametrization schemes such that the total change in PV ($q - q_{adv}$) is much smaller in magnitude. By excluding the boundary-layer, the large signals of opposite sign are excluded from Fig. 3.4a.

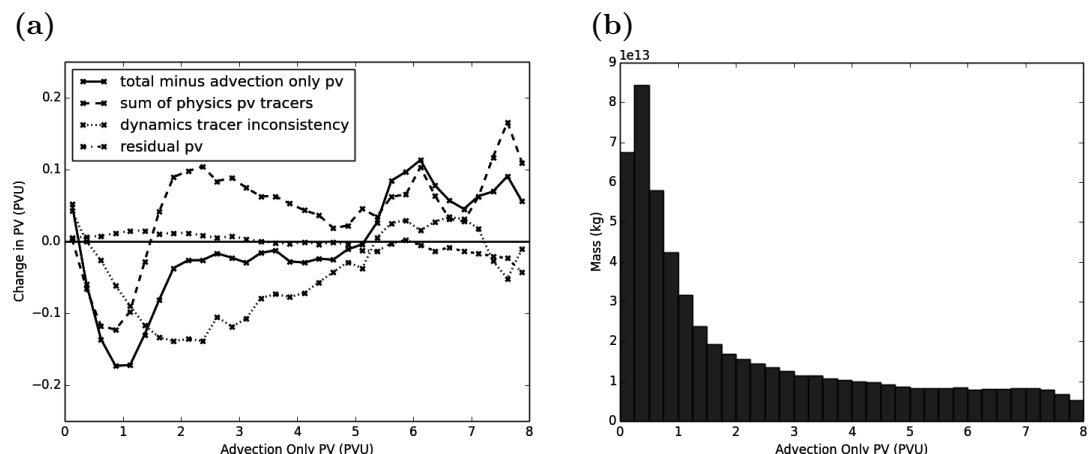


Figure 3.4: (a) The near-tropopause mass-weighted average PV in bins of 0.25 PVU of the advection-only PV tracer. (b) The total mass in each 0.25 PVU bin of advection-only PV. Results shown for the forecast run for the IOP5 case study at 36-hours lead time (00 UTC on 30 November 2011).

Figure 3.4a does show a dipole in the total change in PV. The dipole is consistent with the one in [Chagnon and Gray \(2015\)](#) with the addition of a positive PV anomaly at q_{adv} between 6 and 8 PVU which can be attributed to the use of many vertical levels. More relevant to this study is the large difference between the sum of physics PV tracers and the total change in PV ($q - q_{adv}$). This difference is mostly accounted for by the non-conservation of PV by the dynamical core (ε_I). In Fig. 3.1 there is a difference between the position of the 2 PVU contour of the advection-only PV and the 2 PVU contour of the diagnosed PV that is directly caused by the non-conservation of PV by the dynamical

core. The movement of the 2 PVU contour agrees with Fig. 3.4 in which the zero point of $q - q_{adv}$ is found at $q_{adv} > 2$ but the zero point of $\sum q_{phys}$ is still close to 2 PVU. The difference can be attributed to the systematic reduction of PV by the dynamical core.

Figure 3.5 shows the same diagnostic as Fig. 3.4 as a function of lead time for the accumulated effects of parametrized physical processes and the total change in PV. The difference between Fig. 3.5a and Fig. 3.5b can be attributed to the non-conservation of PV by the dynamical core (ε_I). The sum of physics PV tracers shows a clear dipole at a value of advection only PV tracer close to the 2 PVU tropopause; however this is not present for the total change in PV which appears to have a faint dipole that drifts with time. This suggests that the non-conservation of PV by the dynamical core acts to move the 2 PVU tropopause position whereas the parametrized physical processes do not.

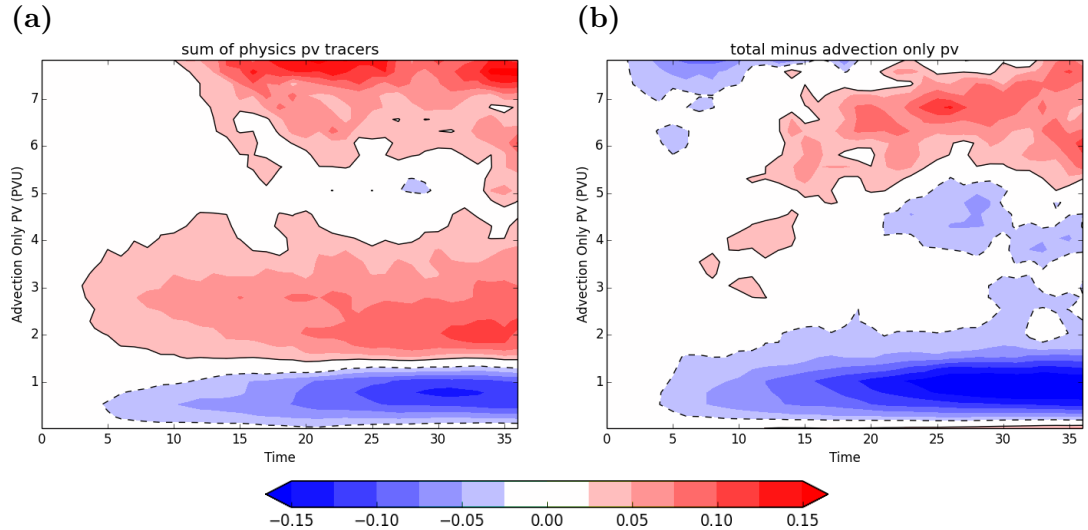


Figure 3.5: The near-tropopause mass-weighted average PV in bins of 0.25 PVU of the advection-only PV tracer against time (hours since forecast initialisation for the forecast run for the IOP5 case study) for (a) the accumulated effects of parametrized physical processes ($\sum q_{phys}$) and (b) the total change in PV ($q - q_{adv}$).

3.3 Conclusions

A new diagnostic framework has been introduced to calculate the non-conservation of PV by the dynamical core of a numerical model of the atmosphere when simulating a realistic case study with a full suite of physics parametrizations. The non-conservation of PV by

the dynamical core has been considered in the context of PV tracers based on the method introduced by [Davis *et al.* \(1993\)](#). [Whitehead *et al.* \(2015\)](#) used tracers of PV to diagnose inconsistencies between dynamical cores and tracer advection schemes but applied to idealised simulations without any parametrization of physical processes. A “dynamics-tracer inconsistency” diagnostic has been incorporated into the PV tracers method in the MetUM and used to diagnose the non-conservation of PV by the dynamical core. It has been shown that, for the IOP5 study, the non-conservation of PV by the dynamical core has a comparable contribution to the PV budget to that of parametrized physical processes.

Discrepancies between the PV diagnosed from the prognostic variables of a model and the PV tracers have been previously noted. [Davis *et al.* \(1993\)](#) attributed the difference to numerical errors in the explicit integration of PV. [Stoelinga \(1996\)](#) attributed the difference to using a numerical model that does not conserve PV explicitly. [Gray \(2006\)](#) and [Chagnon *et al.* \(2013\)](#) attributed the difference to the amplified effects of diffusion across multiple tracers. In reality, all of these terms could be important and will have differing importance for different numerical models. A framework that can account for each of these effects separately has been introduced and the relative importance of these terms for the PV tracers method applied to any numerical weather prediction model can be quantified.

The residual in the PV budget is generally more than an order of magnitude smaller than the dominant physical processes when the non-conservation of PV by the dynamical core is accounted for. Currently the largest part of the residual in the PV budget comes from the pressure solver. If the residual in the PV budget were larger then a method to sensibly partition the PV increment from the pressure solver would need to be developed for the PV tracers. A possible method to include the pressure solver would be to run two timesteps of the model in parallel: one regular timestep and one adiabatic and frictionless timestep. The latter would be used to calculate the dynamics PV increments in calculating the dynamics-tracer inconsistency. This method is generic for any dynamical core and would also be a closer match to the inconsistency defined by [Whitehead *et al.* \(2015\)](#). It has not been implemented here because the dynamics-tracer inconsistency diagnosed from the semi-Lagrangian dynamics only was sufficient to account for most of the residual in the PV tracers.

The simulations used in this thesis do not add any explicit diffusion to the PV tracers. In the initial formulation of the PV tracers method, [Davis et al. \(1993\)](#) chose to add diffusion to the PV increments at each timestep to mimic the effect of explicit thermal diffusion on small-scale anomalies. The approach in this thesis is to use the PV tracers to assess the behaviour of the numerical model itself.

It has been shown that numerical weather prediction models systematically smooth the tropopause PV gradient with lead time ([Gray et al., 2014](#)). One suggestion put forth by [Gray et al. \(2014\)](#) was that the smoothing of the PV gradient was due to an underrepresentation of diabatic processes consistent with the development of a diabatic PV dipole shown by [Chagnon et al. \(2013\)](#). However, the non-conservation of PV by the dynamical core has been shown to have a strong effect on the tropopause and could also explain the smoothing of the PV gradient. The results of [Chagnon et al. \(2013\)](#) and [Chagnon and Gray \(2015\)](#) do implicitly include the non-conservation of PV by the dynamical core because they look at differences between the diagnosed and advection-only PV. However, by attributing PV to dynamics-tracer inconsistency, the uncertainty in the PV budget has been reduced and therefore reduced the uncertainty in the individual PV tracers, further validating the approach in [Chagnon et al. \(2013\)](#) of looking at the effects of individual physical processes on the PV dipole with the caveat that the non-conservation of PV by the dynamical core should also be considered.

By looking at the evolution of numerical solutions to idealised cases of frontogenesis past the point of frontal collapse, [Visram et al. \(2014\)](#) suggested that insufficient Lagrangian conservation of PV can cause a degradation to the long-term solutions of forecasts. The non-conservation of PV by the dynamical core would be a direct cause of this. However, we refrain from describing the non-conservation of PV by the dynamical core as “model error” because it is necessary to have some form of dissipation in numerical models of the atmosphere and this dissipation may also be linked to unrepresented small-scale physical processes. By diagnosing non-conservation of PV by the dynamical core with the dynamics-tracer inconsistency diagnostic the Lagrangian conservation of PV can be assessed with the possibility of differentiating between physical processes and model error.

Chapter 4

Processes Maintaining Tropopause Sharpness

4.1 Introduction

A distinct feature of the extratropical atmosphere is the sharp contrast between the troposphere and the stratosphere: the tropopause. The thermal tropopause is defined as the height at which the vertical lapse rate transitions from tropospheric values to stratospheric values. Composites of radiosonde data in height relative to the thermal tropopause show a shallow static stability maximum above the tropopause known as the tropopause inversion layer (TIL) ([Birner et al., 2002](#)) emphasising that the vertical transition in lapse rate is sharp. The dynamical tropopause defines the boundary between the troposphere and stratosphere as a value of Ertel potential vorticity (PV) between the tropospheric values and stratospheric values. Since PV is conserved for adiabatic and frictionless motion ([Ertel, 1942](#)), the dynamical tropopause emphasises that the tropopause behaves almost like a material surface with exchange of mass between the stratosphere and troposphere only enabled by diabatic processes (including small-scale mixing).

Since both potential temperature (θ) and PV are conserved for adiabatic and frictionless motion, the large-scale dynamics of the midlatitude atmosphere are compactly described by maps of PV on isentropic (constant θ) surfaces ([Hoskins et al., 1985](#)) where the tropopause is seen as a narrow region of strong isentropic gradients of PV separating the high PV stratospheric air and the low PV tropospheric air. The strong isentropic PV gradient at the tropopause, coinciding with the midlatitude jet, acts as a waveguide for Rossby waves ([Hoskins and Ambrizzi, 1993; Schwierz et al., 2004; Martius et al., 2010](#)). Rossby waves can be an important source of predictability in medium-range forecasting ([Grazzini and Vitart, 2015](#)) and are crucial to accurately representing longer time-scale processes ([Palmer et al., 2008](#)).

The isentropic tropopause PV gradient decreases systematically with forecast lead time in current numerical weather prediction (NWP) models (Gray *et al.*, 2014). Rossby wave propagation depends on to the isentropic PV gradient: a weaker tropopause PV gradient both reduces jet speed and weakens the upstream propagation rate of Rossby-waves. Harvey *et al.* (2016) showed that the two effects cancel at first order but at second order the reduction in jet speed is greater, giving a net reduction in phase speed. They estimated that the smoother isentropic PV gradients seen in NWP forecasts compared to analyses would produce a phase error in Rossby waves of 400 km over 5 days.

The reduction of the tropopause PV gradient with forecast lead time indicates that there is a net imbalance in the processes modifying the tropopause PV gradient. The purpose of this chapter is to quantify the systematic effects of different processes contributing to the tropopause PV gradient. The structure of this chapter is as follows. A brief review of the key processes affecting the tropopause sharpness is given in section 4.2. An objective definition of ridges and troughs used in compositing the forecasts is defined in section 4.3. Section 4.4 describes the results. The key conclusions and discussion of results are presented in section 4.5.

4.2 Processes Affecting Tropopause Sharpness

From previous studies, three key processes affecting tropopause sharpness have been identified: vortex stripping, radiative cooling and latent heating enhanced ascent (i.e. warm conveyor-belts (WCBs)) have significant effects on the midlatitude tropopause. In this study the relative contributions of these processes are quantified using daily forecasts over a winter season.

Vortex stripping describes a process in which sharp gradients in vorticity are generated from an initially smooth vorticity distribution in two-dimensional fluids (Legras and Dritschel, 1993). Using an isentropic single-layer quasi-geostrophic model, Ambaum (1997) showed that the two-dimensional vortex stripping motion of baroclinic eddies is the essential process for forming and maintaining a sharp tropopause PV gradient. Results of three-dimensional simulations have shown that layerwise horizontal vortex stripping in isentropic layers can also result in sharp vertical PV gradients (Haynes *et al.*, 2001) and a TIL (Son and Polvani, 2007; Wang and Geller, 2016). The general action of vortex

stripping can be described as air being stirred on either side of the tropopause without stirring across the tropopause which acts as a transport barrier. We can approximately consider that the stirring results in a three-component fluid on an isentrope with high-PV stratospheric air around the poles and low-PV tropospheric air equatorward, separated by a region of intermediate PV: the tropopause. The regions of intermediate PV are drawn away from the tropopause by the eddies on either side of the tropopause. The intermediate PV is then stretched out into filaments. As the filaments stretch out they are broken up by small-scale mixing and gradually dissipated. The result is that the PV gradient at the tropopause has been enhanced by removing the intermediate PV air and bringing high and low PV air closer together. At longer time scales small-scale mixing will eventually dominate resulting in a uniform PV distribution; a key process for maintaining the tropopause sharpness in idealized simulations is the inclusion of a thermal relaxation towards a state with a smooth equator-to-pole PV gradient, as an idealized representation of other diabatic processes, which acts to maintain the contrast between the high-PV stratospheric air and the low-PV tropospheric air. The result is a dynamical equilibrium between thermal relaxation and vortex stripping ([Ambaum, 1997](#); [Haynes *et al.*, 2001](#)).

The effects of diabatic processes on the tropopause are more complicated than thermal relaxation: [Forster and Wirth \(2000\)](#) showed that radiative cooling could directly enhance the PV contrast across filaments of PV provided the vorticity was sufficiently large and [Randel *et al.* \(2007\)](#) showed that radiative cooling provides a significant contribution to the strength of the TIL. The dominant contribution to the direct effect of radiation on the tropopause is long-wave cooling from water vapour ([Forster and Wirth, 2000](#); [Ferreira *et al.*, 2016](#)): the moister troposphere cools more rapidly than the drier stratosphere with the most efficient cooling just below the dry layer resulting in a gradient of diabatic heating and positive PV tendencies across the humidity gradient. The presence of clouds will modify the profile of radiation and, as a result, the PV tendencies. The addition of clouds below the tropopause acts to focus the maxima in radiative cooling at the cloud top ([Cau *et al.*, 2005](#)), resulting in a sharper gradient in diabatic heating rate and a stronger and more localised dipole of PV tendencies, positive above the cloud and negative below.

Latent heating in WCBs has been shown to affect the tropopause. WCBs are air streams associated with extratropical cyclones which transport air upwards and polewards ([Harrold, 1973](#)). A WCB airstream can be identified as a coherent ensemble of trajectories

ascending 600 hPa in 48 hours following Wernli and Davies (1997). WCBs transport moist low-PV air from the boundary layer to the upper troposphere (Wernli and Davies, 1997) and the outflow can have large impacts on the tropopause and subsequent Rossby wave propagation (Riemer and Jones, 2010; Grams *et al.*, 2011). Latent heating has a large effect on WCB evolution: air parcels typically experience a net heating of ≈ 20 K (Madonna *et al.*, 2014) mainly associated with condensation at low levels and depositional growth of snow at upper levels (Joos and Wernli, 2012). Schemm *et al.* (2013) showed that a dry simulation produced a weaker WCB and as a result slower development of a downstream cyclone when compared with a moist simulation. In terms of PV, air parcels experience positive PV tendencies below the maximum in latent heating rates and negative PV tendencies above. WCB climatologies have found the net change in PV between the inflow and outflow of WCB trajectories to be close to zero (Madonna *et al.*, 2014). Methven (2015) used a Kelvin's circulation argument to outline the conditions under which the PV of the inflow is expected to match that of the outflow.

Chagnon *et al.* (2013) showed that the combined effect of long-wave radiation and WCBs gave a dipole of diabatically-generated PV that enhanced the tropopause PV gradient. Chagnon *et al.* (2013) also argued that the transport of moisture by the WCB would enhance the effects of long-wave radiation. Kunkel *et al.* (2016) showed similar results for the TIL: long-wave radiation strengthened the TIL and transport of moisture to the tropopause results in a more rapid formation of the TIL. However, these results are limited to case studies (Chagnon *et al.*, 2013; Chagnon and Gray, 2015) and idealised simulations (Kunkel *et al.*, 2016). This study instead quantifies the systematic effects of physical processes on the tropopause over a season of forecasts with an NWP model.

4.3 Objective Definition of Ridges and Troughs

The results in this study are tropopause-relative composites produced over ridges and troughs separately. The expectation is that there will be significant differences in the behaviour of physical processes in ridges and troughs. For example, we might expect stronger effects of radiation in troughs due to a lower tropopause meaning more moist and cloudy air below the tropopause (e.g. Cavallo and Hakim (2009)), whereas we might associate ridges more with the strongly ascending WCB outflows. There are also differences in the structure of ridges and troughs purely due to the balanced dynamics (Wirth,

2001). In this section a new diagnostic approach for dividing regions into ridges and troughs is described.

The diagnostic extends Gray *et al.* (2014) where the position of the tropopause is compared with an “equivalent latitude” (to be defined below). Gray *et al.* (2014) identify the location of the tropopause with a single contour of PV on 320 K: anywhere the contour is poleward of its equivalent latitude is a ridge and anywhere the contour is equatorward is a trough. Hoskins and Berrisford (1988) introduced maps of θ on the tropopause as a useful overview of multiple isentropic PV maps, where a value of 2 PVU is typically used to define the tropopause. An isopleth of PV on a θ surface is the same as an isopleth of θ on a PV surface; therefore, a map of θ on the 2-PVU surface is equivalent to identifying the 2-PVU tropopause on every isentrope that intersects it. An exception is that the 2-PVU surface can fold so that the 2-PVU surface can be crossed multiple times on a vertical profile above some geographical locations. At any geographical location where the PV surface is folded, the highest value of θ is taken. Ridges and troughs are then defined as anomalies of θ on the 2-PVU surface relative to a zonally symmetric background state:

$$\theta' = \theta(\lambda, \phi, q=2) - \theta_b(\phi, q=2), \quad (4.1)$$

where $\theta(\lambda, \phi, q=2)$ is the forecast θ as a function of longitude (λ) and latitude (ϕ) on the 2-PVU surface ($q=2$) and $\theta_b(\phi, q=2)$ is a zonally symmetric background state. A gridpoint is defined as being in a ridge or trough by a positive or negative value of θ' respectively.

The background state used here is defined by adiabatic rearrangement of PV to a zonally symmetric state (Methven and Berrisford, 2015): for each PV contour on each isentropic surface an equivalent latitude (ϕ_e) is defined as the latitude circle that encloses the same mass and circulation as the PV contour in the full (3D) state. The method of Methven and Berrisford (2015) calculates a set of equivalent latitudes as a function of PV value on isentropic surfaces $\phi_e(\theta, q)$ at six-hourly intervals from ERA-Interim data (Dee *et al.*, 2011). Figure 4.1a shows the range of $\phi_e(\theta, q=2)$ for the three-month forecast period with the first timestep of each month overplotted to highlight the instantaneous structure.

In the midlatitudes, the equivalent latitude of the 2-PVU surface decreases monotonically going to higher θ surfaces (Fig. 4.1a). In this region a poleward displacement of the 2-PVU surface can be unambiguously associated with a positive θ anomaly (negative for

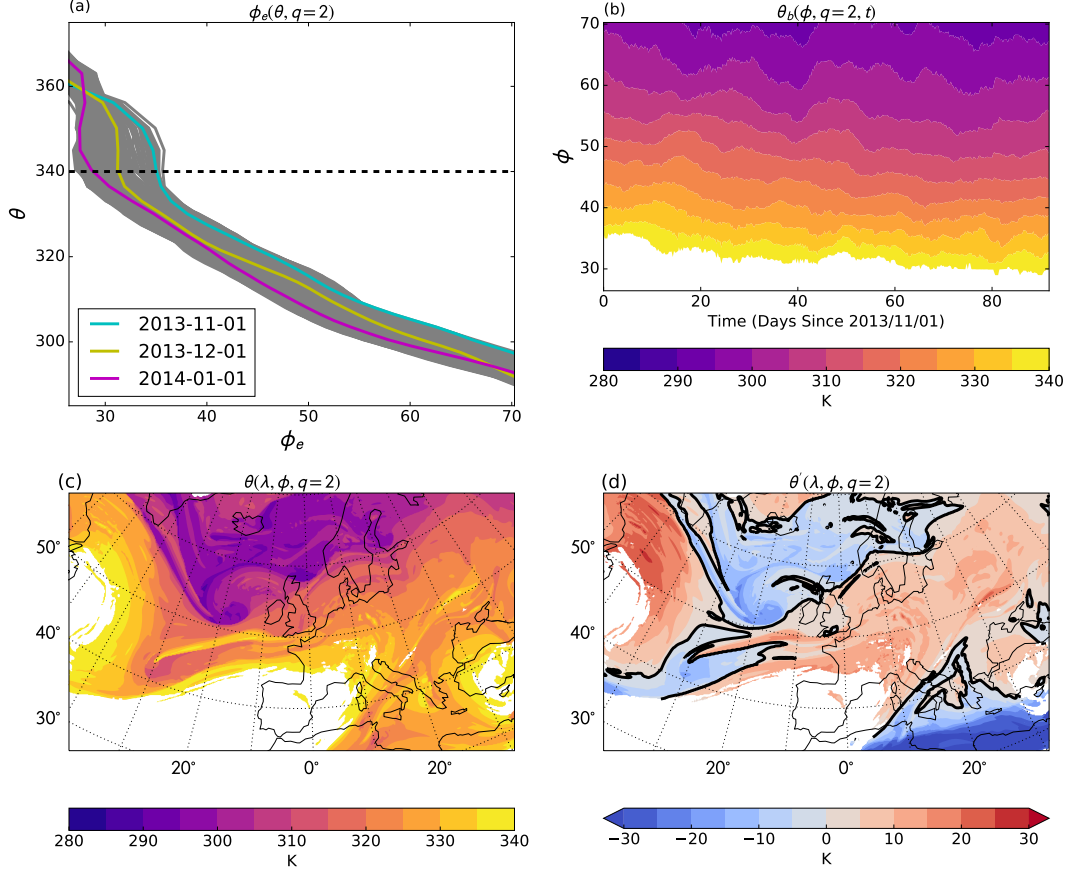


Figure 4.1: The background state on the 2-PVU surface used to diagnose ridges and troughs for the three-month forecast period. (a) $\phi_e(\theta, q=2)$, gray shows the range of values with highlighted lines showing the first timestep of each month. (b) The evolution of $\theta_b(\phi, q=2)$. (c) $\theta(\lambda, \phi, q=2)$ for the first forecast at 24-hours lead time. (d) θ' from Eq. 4.1: anomaly of (c) relative to the background state with $\theta'=0$ highlighted by the bold line. The white regions in (c) and (d) show the mask on $\theta(\lambda, \phi, q=2) > 340$ K.

an equatorward displacement). The exception is at the 340–350 K range corresponding to the subtropical jet: at the subtropical jet, the background state 2-PVU surface can be folded so that $\theta_b(\phi, q=2)$ is multivalued. Chagnon and Gray (2015) noted that the dipole of diabatically-generated PV across the 2-PVU surface was not robust in subtropical regions which is consistent with the tropopause equatorward of the subtropical jet not being well defined as a constant PV surface (Wilcox *et al.*, 2012); therefore, regions where the forecast $\theta(\lambda, \phi, q=2)$ is greater than 340 K are excluded from the diagnostics calculated here. The background state $\theta_b(\phi, q=2, t)$ is then calculated by finding the θ that satisfies $\phi_e(\theta, q=2) = \phi$ by linear interpolation. In the case of multiple θ values, the

value of θ less than 340 K is taken. Figure 4.1b shows $\theta_b(\phi, q=2, t)$. Note that there is no time averaging but that $\theta_b(\phi, q=2, t)$ is inherently slowly varying.

Figure 4.1c shows $\theta(\lambda, \phi, q=2)$ from the first forecast at 24-hours lead time and Fig. 4.1d shows the anomaly relative to the background state. Ridges and troughs are defined by the sign of the anomaly in Fig. 4.1d (positive and negative respectively). The advantage of this diagnostic is that it has allowed identification of ridges and troughs on a limited area domain even if it is much smaller than the scale of Rossby wave activity. The white regions in Fig. 4.1c and d show the mask applied at $\theta > 340$ K to ignore subtropical air masses. There are occasionally regions of negative or near zero PV in the stratosphere associated with gravity-wave breaking that cause the tropopause to be diagnosed too high; the mask on $\theta > 340$ K is also useful for excluding these points.

4.4 Results

In this section the results from the winter-season forecasts are presented. Composites of PV and PV tracer diagnostics relative to the tropopause are presented in section 4.4.1. In section 4.4.2 the tropopause-relative composites are used to quantify the evolution of tropopause sharpness with lead time and the contributions of different processes to tropopause sharpness. In the following sections the results from the first two sections are explained in terms of different processes: chaotic advection by the model winds (section 4.4.3), dynamics-tracer inconsistency (section 4.4.4) and parametrized physical processes (section 4.4.5).

4.4.1 Tropopause-Relative Composites

The novel method that led to the discovery of the TIL by Birner *et al.* (2002) was compositing radiosonde profiles relative to the diagnosed thermal tropopause. The composites in this study are produced in a coordinate relative to the dynamical tropopause, defined as the 2-PVU surface,

$$\tilde{z} = z - z(q=2). \quad (4.2)$$

The approach is similar to Cavallo and Hakim (2009) who used a coordinate of pressure relative to the tropopause to composite PV tendencies in tropopause polar vortices. The composites are produced using the following method:

1. For each forecast, at each lead time
 - (a) Calculate the height of the 2-PVU surface using linear interpolation from PV on model levels. For any columns with multiple heights for the 2-PVU surface (i.e. folded tropopause), the highest position is taken.
 - (b) Linearly interpolate each variable to height levels relative to the dynamical tropopause (\tilde{z}). The levels are taken every 0.2 km up to ± 2 km from the tropopause. Note that this resolution is sharper than the vertical model grid spacing which decreases from 400 m at 6 km to 600 m at 12.5 km.
 - (c) Calculate the area-weighted mean of each variable on each tropopause-relative level over areas diagnosed as ridges and troughs separately.
2. Calculate the mean and standard error of each diagnostic over the set of forecasts.

The compositing method above is then repeated taking \tilde{z} relative to the 2-PVU surface of the advection-only PV tracer ($q_{adv}=2$) rather than $q=2$ in Eq. 4.2. Repeating the composites relative to each surface ($q=2$ and $q_{adv}=2$) allows us to systematically quantify how much non-conservative processes act on either side of the tropopause (the composites are the same) or directly influence stratosphere-troposphere exchange by separating the two surfaces (the composites are different). This can be seen if we consider some non-conservative process producing negative PV tendencies initially above the tropopause. In this case, initially stratospheric air ($q>2$) can become tropospheric ($q<2$) such that the diagnosed position of the $q=2$ surface has moved above the negative PV tendencies but the position of the $q_{adv}=2$ surface is unchanged. The opposite can occur for positive PV tendencies initially below the tropopause with the position of the $q=2$ surface moving below the positive PV tendencies. Over many of these situations we would diagnose positive PV tendencies systematically above the $q=2$ surface but below the $q_{adv}=2$ surface and negative PV tendencies systematically below the $q=2$ surface but above the $q_{adv}=2$ surface. Therefore, a composite over many cases would diagnose dipoles across the $q=2$ and $q_{adv}=2$ surfaces of opposite sign; however, since the $q=2$ surface has moved this does not necessarily imply any change in the diagnosed PV gradient across the $q=2$ surface, only that mass is being exchanged between the troposphere and stratosphere. This would not be the case for positive PV tendencies above the tropopause or negative PV tendencies below the tropopause because they would not directly move the $q=2$ surface, and therefore

have a direct effect on the PV gradient. This is also true of PV tendencies occurring near the tropopause that are too weak to directly move the $q=2$ surface. In these cases, the composites relative to $q=2$ and $q_{adv}=2$ would be the same and imply a direct effect on the tropopause PV gradient.

Figure 4.2 shows the tropopause-relative composites over ridges (a,b,c) and troughs (d,e,f) at 24-hours lead time. Figure 4.2a and d show PV and q_{adv} as the difference between the 24-hour forecasts and the verifying analyses for each forecast. The profile of PV in Fig. 4.2 is thus the systematic forecast error. There is a systematic decrease in PV above the 2-PVU surface relative to analyses, but comparatively little change in the troposphere (the error is zero at the tropopause because $q=2$ by definition). The systematic errors in PV can be contrasted with q_{adv} which reduces above the tropopause and increases below the tropopause relative to the analyses (Fig. 4.2a and d). The difference between PV and q_{adv} is the “net effect of non-conservative processes” ($q - q_{adv}$) which was shown to enhance the tropopause PV gradient by Chagnon *et al.* (2013). The tendency of $q - q_{adv}$ is systematically positive in the stratosphere and negative in the troposphere (Fig. 4.2b and e) consistent with the case studies from Chagnon *et al.* (2013) and Chagnon and Gray (2015). The effects of non-conservative processes are also of similar magnitude to the systematic forecast errors.

The PV tracers partition $q - q_{adv}$ (Chapter 3) into parametrized physical processes ($\sum q_{phys}$), dynamics-tracer inconsistency (ε_I) and a residual (ε_r). Figure 4.2b and e show that the residual is small with approximately zero systematic effect allowing us to focus on the remaining terms. The combined effect of parametrized physical processes ($\sum q_{phys}$) is to produce a dipole in PV tendencies with positive PV tendencies in the stratosphere and negative PV tendencies in the troposphere and approximately zero net change at the 2-PVU surface, consistent with the findings of Chagnon *et al.* (2013) and Chagnon and Gray (2015) from individual case studies. The dipole is similar when composited relative to $q_{adv}=2$, albeit weaker, showing that the parametrized physical processes are acting to directly enhance the tropopause PV gradient rather than change the height of the tropopause. The partitioning of $\sum q_{phys}$ into individual physical processes (Fig 4.2c and f) is discussed in section 4.4.5.

The dynamics-tracer inconsistency (ε_I) shows net negative tendencies at tropopause level in ridges and troughs (Fig. 4.2b and e) although there are positive PV tendencies

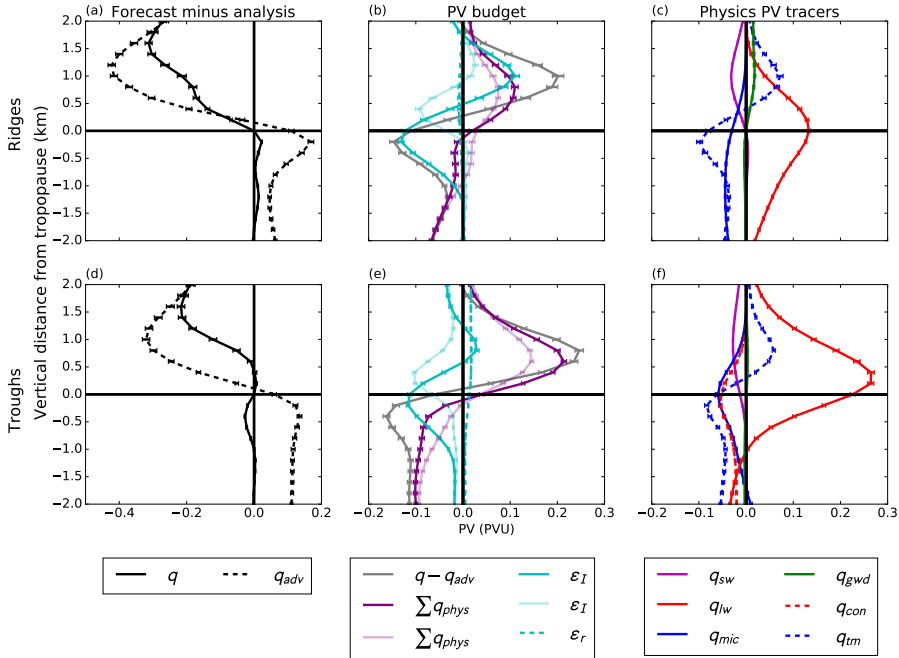


Figure 4.2: PV as a function of vertical distance from the 2-PVU surface in ridges (a, b and c) and troughs (d, e, and f). Lines show the mean and error bars show the standard error on the mean for the 92 winter-season forecasts at 24-hours lead time. (a) and (d) show the forecast minus analysis values for PV (q) and the advection-only PV tracer (q_{adv}). (b) and (e) show the difference ($q - q_{adv}$) and the contributing processes: parametrized physical processes ($\sum q_{phys}$), dynamics-tracer inconsistency (ε_I) and a residual (ε_r). The faint lines show composites relative to the advection-only PV tracer ($q_{adv}=2$) for ε_I and $\sum q_{phys}$. (e) and (f) show the contributions to $\sum q_{phys}$ from the individual physics tracers: short-wave radiation (q_{sw}), long-wave radiation (q_{lw}), microphysics (q_{mic}), gravity-wave drag (q_{gwd}), convection (q_{con}) and turbulent mixing (q_{tm}).

around 1 km above the tropopause which are more pronounced in ridges than in troughs. The negative peak is slightly below $q=2$, but above $q_{adv}=2$, which indicates that, unlike the parametrized physical processes, the main effect of ε_I is to directly separate the two surfaces ($q_{adv}=2$ and $q=2$). This does not explain why ε_I is most negative at the tropopause which is discussed in section 4.4.4.

4.4.2 Tropopause PV Contrast

To quantify the effects of different physical processes on the reduction in isentropic PV gradient seen in [Gray et al. \(2014\)](#) we can calculate the vertical tropopause PV contrast of the variables in Fig. 4.2 over a fixed distance. From the tropopause relative means, the tropopause PV contrast for each variable is calculated as the difference between the average of points 1 km above and below the tropopause. As with the previous composites, the mean and standard error are then calculated over the 92 forecasts. By calculating the vertical tropopause PV contrast, the difference in PV between tropospheric and stratospheric air near the tropopause is quantified. This will be equivalent to quantifying the isentropic PV contrast over a larger horizontal distance; however, the varying slope of the tropopause is a limiting factor in this comparison. Strong isentropic PV gradients often occur where the tropopause is almost vertical (e.g. [Davies and Rossa \(1998\)](#)) and will not be well quantified by this method.

Figure 4.3 shows the tropopause PV contrast as a function of lead time for each of the variables in Fig. 4.2. There is a reduction in PV contrast with lead time (Fig. 4.3a and d) consistent with the reduction in isentropic PV gradient found by [Gray et al. \(2014\)](#). The reduction in PV contrast is stronger in ridges than in troughs.

The contrast in q_{adv} decreases more rapidly than for PV because it is not being maintained by diabatic processes: the parametrized physical processes produce a net increase in the tropopause PV contrast with lead time in ridges and troughs (Fig. 4.3b and e). The contribution of individual physical processes (Fig 4.3c and f) is discussed in section 4.4.5. The diagnosed contribution of ε_I to the tropopause PV contrast is less clear, showing an increased contrast relative to $q=2$ and a reduced contrast relative to $q_{adv}=2$. This is because, as stated in the previous section, ε_I is acting to directly separate the two surfaces.

4.4.3 Tracer Advection

The evolution of q_{adv} is a result of advection by the resolved winds of the model using the semi-Lagrangian scheme of the MetUM. Conservative tracer advection results in a continuous cascade of features to smaller scales. Horizontal and vertical length scales in tracers decrease exponentially at the same rate ([Haynes and Anglade, 1997](#)) giving an

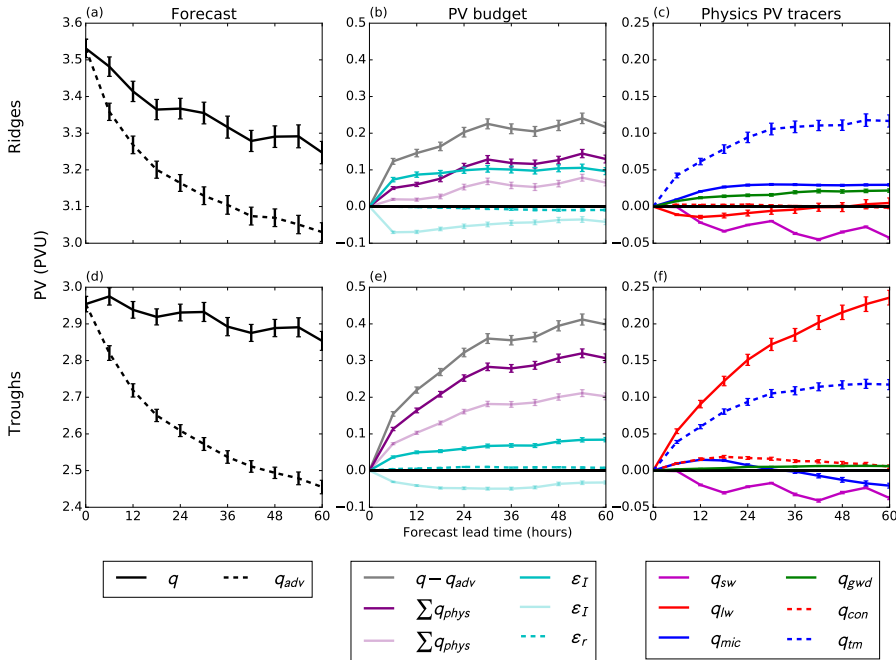


Figure 4.3: The same variables as in Fig. 4.2, but showing the tropopause PV contrast as a function of lead time calculated as the difference between points up to 1 km above and 1 km below 2-PVU. PV and the advection-only PV tracer are shown as absolute values rather than forecast minus analysis.

exponential increase in tracer gradients. The difference here is that implicit numerical diffusion takes over as length scales approach the grid-scale and the PV contrast is calculated over a fixed length scale. Diffusive processes act most rapidly at small scales and slowly at large scales. The contrast in q_{adv} decreases as features cascade to smaller scales where diffusion reduces the extrema.

The decrease of the contrast in q_{adv} is the opposite to that expected from vortex stripping (see section 4.2). The reason for this different behaviour is that there is a dynamical equilibrium between sharpening by intermittent stripping events and a continuous smoothing of the tropopause. A model with consistent initial conditions would be initialised in the dynamic equilibrium state of the model climate and the net effects of processes sharpening and smoothing the tropopause would cancel out over many forecasts, giving a constant PV gradient as a function of lead time. In the idealised simulations of Ambaum (1997) and Haynes *et al.* (2001) the diabatic processes contribute to a smoothing of the tropopause and so an advection-only PV tracer initialised in the dynamic equilibrium state would show a net sharpening of the tropopause on short timescales. In our

simulations diabatic processes directly sharpen the tropopause so the net effect of the advection scheme must be to smooth the tropopause. Also, the forecasts start from an analysis in which gradients are sharper than can be maintained by the free-running model.

The net result of the tracer advection is that the contrast of q_{adv} as a function of lead time (T) exponentially decays from an initial contrast $\Delta q_{adv}(0)$, to a reduced contrast, $\Delta q_{adv}(\infty)$,

$$\Delta q_{adv}(T) = \Delta q_{adv}(\infty) + [\Delta q_{adv}(0) - \Delta q_{adv}(\infty)]e^{-\frac{T}{\tau}}, \quad (4.3)$$

where τ is the decay timescale. Although the term $\Delta q_{adv}(\infty)$ is obtained by fitting Eq. 4.3 to the forecast data, it cannot be a long-time limit for a passive tracer because a tracer will eventually become well mixed as diffusive effects dominate.

The parameters in Eq. 4.3 have been calculated by fitting Eq. 4.3 to the evolution of $\Delta q_{adv}(T)$ using `scipy.optimize.curve_fit` (Jones *et al.*, 2017). Figure 4.4 shows an example of this fit for $\Delta q_{adv}(T)$ in ridges. The solid black line is the same as the dashed line in Fig. 4.3a and the grey line shows Δq_{adv} calculated from composites relative to $q_{adv}=2$ rather than relative to $q=2$. The evolution of Δq_{adv} relative to $q_{adv}=2$ is shown because the evolution can only be a result of the tracer advection scheme, even in the presence of non-conservative processes. The circles in Fig 4.4a show the fit of Eq. 4.3. Note that the first data point has been excluded from the fit leaving $\Delta q_{adv}(0)$ as a derived parameter. This was done because the first six-hours deviates slightly from an exponential decay. This can be seen from the fitted points: in the first six-hours Δq_{adv} decreases more rapidly relative to $q=2$ and slightly less rapidly relative to $q_{adv}=2$ compared to what would be predicted from the following exponential decay. The estimate of $\Delta q_{adv}(0)$ is not very sensitive to ignoring the first data point; however, the derived timescale is sensitive to overfitting to the first data point giving an overestimation of the timescale relative to $q=2$ and an underestimation of the timescale relative to $q_{adv}=2$.

The fit of Eq. 4.3 is repeated for multiple vertical length scales by calculating Δq_{adv} only from points up to $\pm\tilde{z}$: Fig. 4.4b shows the derived timescale. The timescale appears to be constant at small vertical scales because we approach the vertical level spacing of the model which reduces from 400 m at 6 km to 600 m at 12.5 km altitude. Approaching the scale of the vertical resolution, the timescale increases in ridges and decreases at in troughs. It is unclear why the timescale in ridges and troughs should have the opposite behaviour as a function of vertical scale; however, the timescale does approach a similar

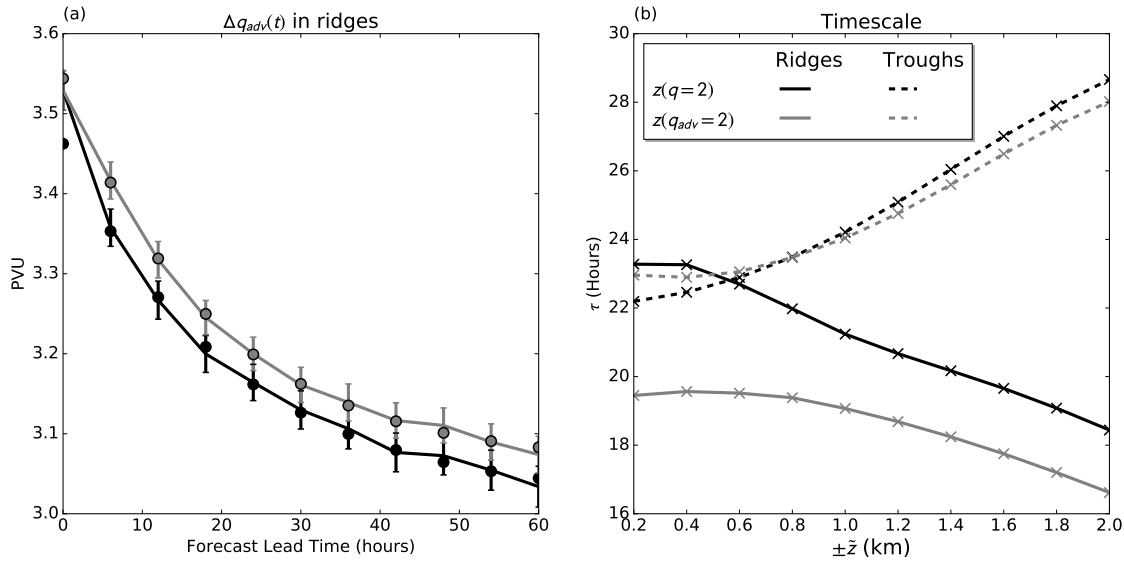


Figure 4.4: Fitting of Eq. 4.3 to the decay of Δq_{adv} in the winter-season forecasts. (a) Δq_{adv} in ridges (circles show fit). (b) The derived timescale from Eq. 4.3 for varying vertical scales. The key in (b) applies to both plots.

value of 20–24 hours in ridges and troughs.

4.4.4 Dynamics-tracer Inconsistency

The dynamics-tracer inconsistency quantifies the difference between non-conservation of PV resulting from the dynamical core and non-conservation associated with the tracer advection scheme. Saffin *et al.* (2016) showed that local tendencies of dynamics-tracer inconsistency were dominated by non-conservation of PV by the dynamical core; however, this result does not necessarily generalize to the integrated tendencies over many forecasts so it is important to diagnose the underlying processes.

Figure 4.5 shows the tropopause-relative mean of the dynamics-tracer inconsistency as a function of lead time. The top panels show composites relative to $q=2$ and the bottom panels show composites relative to $q_{adv}=2$. There is a dipole of positive and negative tendencies centered slightly above $q=2$ suggesting a raising and sharpening of the tropopause. However, the peak in negative tendencies is shifted upwards when composited relative to $q_{adv}=2$, as well as net positive tendencies appearing below $q_{adv}=2$ in ridges, as a result of the two surfaces ($q_{adv}=2$ and $q=2$) being separated by dynamics-tracer inconsistency rather than directly affecting the tropopause PV gradient (see section 4.4.1). The pos-

itive tendencies have saturated at short lead times which may explain the discrepancy in behaviour of Δq_{adv} over the first 6 hours in Fig. 4.4. This rapid saturation can also be seen for the diagnosed effect of dynamics-tracer inconsistency on the PV contrast in ridges (Fig. 4.3b).

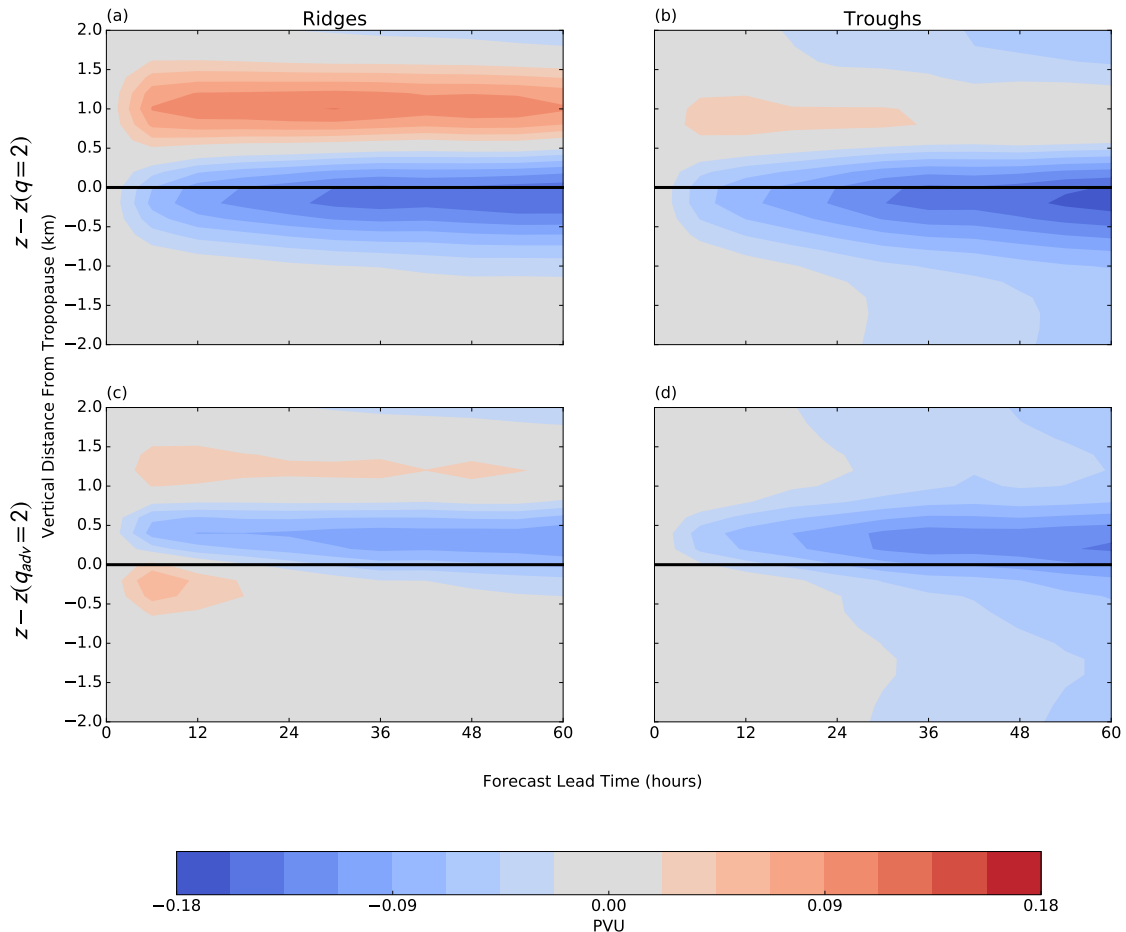


Figure 4.5: Dynamics-tracer inconsistency as a function of forecast lead time in ridges (a and c) and troughs (b and d). Values shown are the mean from the 3-months of forecasts when composited relative to the 2-PVU surface of PV (a and b) and the 2-PVU surface of the advection-only PV tracer (c and d)

At longer lead times the dynamics-tracer inconsistency becomes increasingly negative which is more pronounced in troughs. A possible explanation for the net negative tendencies of the dynamics-tracer inconsistency is that it results from dissipation as part of the vortex stripping process: as filaments of PV are drawn away from the tropopause the dynamical-core dissipates the PV filament faster than tracer advection giving negative tendencies in the filament. Negative PV tendencies are consistent with a downwards dia-

batic transport of mass by dilution of PV substance ([Haynes and McIntyre, 1987](#)). This is consistent with the isentropic map of ε_I shown in [Saffin et al. \(2016\)](#) (their Fig. 2c) where net negative tendencies are seen in the troughs where $q=2$ is displaced from $q_{adv}=2$.

4.4.5 Parametrized Physical Processes

The combined effect of parametrized physical processes is to produce a dipole in PV tendencies with positive PV tendencies in the stratosphere and negative PV tendencies in the troposphere and zero net change at the 2-PVU surface (Fig. 4.2b and e), but this dipole is much weaker in ridges than troughs. These processes are now considered separately.

The largest contribution to the PV tendencies comes from the long-wave radiation which produces net positive PV tendencies at the tropopause and is about twice as strong in troughs as in ridges (Fig. 4.2c and f). Since the long-wave radiation is dependent on the humidity contrast and the absolute vorticity ([Forster and Wirth, 2000](#)), the stronger magnitude in troughs would be expected. Figure 4.6 shows variables from the analyses as a function of distance from the 2-PVU tropopause in ridges and troughs. Both the contrast in specific humidity (Fig. 4.6a) and the magnitude of the vertical component of the absolute vorticity (Fig. 4.6b) are approximately twice as strong in troughs as in ridges.

The contrast of the long-wave radiation PV tracer across the tropopause is also much stronger in troughs than ridges (Fig. 4.3c and f) which is due to the net PV tendencies being more symmetric across the tropopause in ridges than in troughs (Fig. 4.2c and f). The asymmetry of the net PV tendencies in troughs is likely due to the increased amount of clouds in troughs compared to ridges (Fig. 4.6c and d). As described in section 4.2, cloud-top cooling results in a sharp spike in diabatic cooling and, as a result, a dipole of PV tendencies. When composited over many clouds with varying distance from the tropopause this will show an enhanced gradient. [Cavallo and Hakim \(2009\)](#) showed that cloud-top cooling was a key process for intensifying tropopause polar vortices. The composites of PV tendencies relative to tropopause polar vortices from [Cavallo and Hakim \(2009\)](#) (their Fig. 9) show similar tendencies to those seen for our composite over troughs (Fig. 4.2) with net positive tendencies across the tropopause and negative tendencies further below the tropopause.

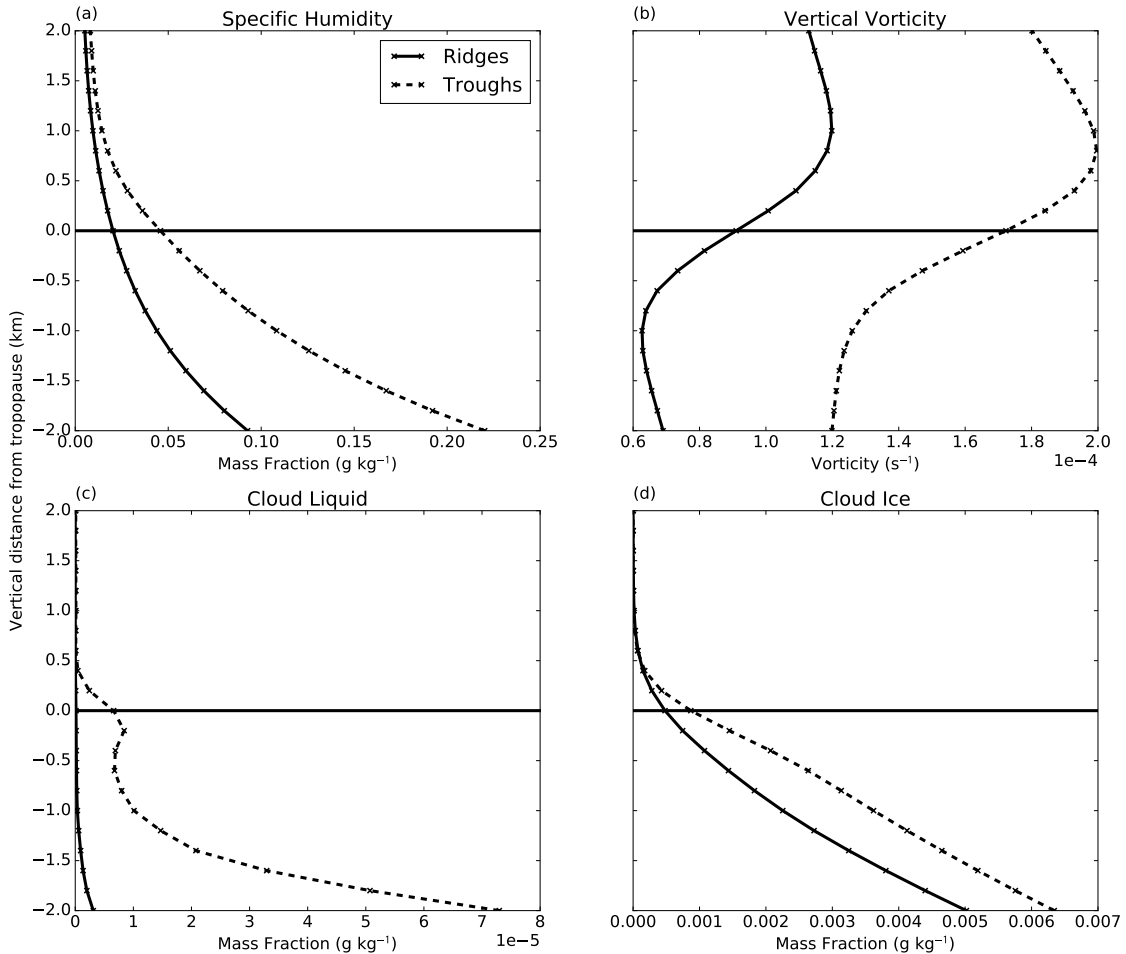


Figure 4.6: The mean of variables as a function of distance from the 2-PVU tropopause in ridges and troughs from Met Office analyses at 00 UTC over the three-month winter-season forecast period. (a) Specific humidity, (b) vertical component of absolute vorticity, (c) mass fraction of cloud liquid and (d) mass fraction of cloud ice.

Short-wave radiation produces negative PV tendencies above the tropopause (Fig. 4.2c and f) which act to reduce the PV gradient with a clear diurnal cycle visible (Fig. 4.3c and f) since the forecasts use a limited area domain. In both ridges and troughs, short-wave radiation reduces the PV gradient during the daytime by producing negative tendencies in PV above the tropopause. Negative PV tendencies indicate a negative heating gradient in the lower stratosphere which is most likely due to the variation in water vapour. Radiative heating due to ozone might be expected to have a large effect as positive PV tendencies below a heating maxima. Strongly positive values of the short-wave radiation PV tracer are seen at higher altitudes, but too far from the tropopause to affect the composites in

Figs. 4.2 and 4.3.

The microphysics PV tracer shows a net negative PV accumulation below the tropopause in both ridges and troughs (Fig. 4.3c and f), consistent with the negative PV tendencies from ascent above the maxima in latent heating. The association of the turbulent-mixing PV tracer to vertical transport is less clear. Chagnon *et al.* (2013) associated negative values of the turbulent-mixing PV tracer with transport of tracer from the boundary-layer by a WCB. Ventilation of the boundary layer is dominated by WCBs (Sinclair *et al.*, 2008) so we might expect to see a signature of WCB transport to the tropopause in the turbulent-mixing PV tracer; however, we see an effect at short lead times, so it is important to distinguish between the effects of parametrized mixing at the tropopause-levels and long-range transport from the boundary-layer.

The diagnosed impact of processes related to WCBs depends on the length of the forecast. Figure 4.7a and b show the tropopause relative mean of the microphysics PV tracer as a function of lead time. The microphysics PV tracer shows net negative values in both ridges and troughs at short lead times because air is sampled in the region of negative PV tendencies above the latent heating maxima. At longer lead times ridges and troughs show quite different behaviour: in ridges the values of the microphysics PV tracer are consistently negative whereas in troughs the negative values of the microphysics PV tracer are gradually replaced with positive values. This is because the outflow of WCBs, where the net change in PV will be negative or zero, is typically associated with ridges whereas in troughs, where the tropopause is lower, we will be compositing over air masses that are still ascending or have been affected by latent heating that is not associated with WCBs.

The turbulent mixing parametrization is having a systematic effect on the tropopause within the first six hours in both ridges and troughs which is unlikely to be from WCBs (Fig. 4.7c and d). The strongest negative tendencies are just below tropopause level and near zero further below indicating that they are not being advected from lower levels. There is a small hint of negative tendencies increasing from lower levels with lead time, but the dominant process is turbulent mixing at tropopause levels.

Convection has almost zero effect in ridges but shows net negative tendencies in troughs. This makes sense since the tropopause is lower in troughs and so we expect stronger convective transport in troughs. The reverse is true for gravity-wave drag with

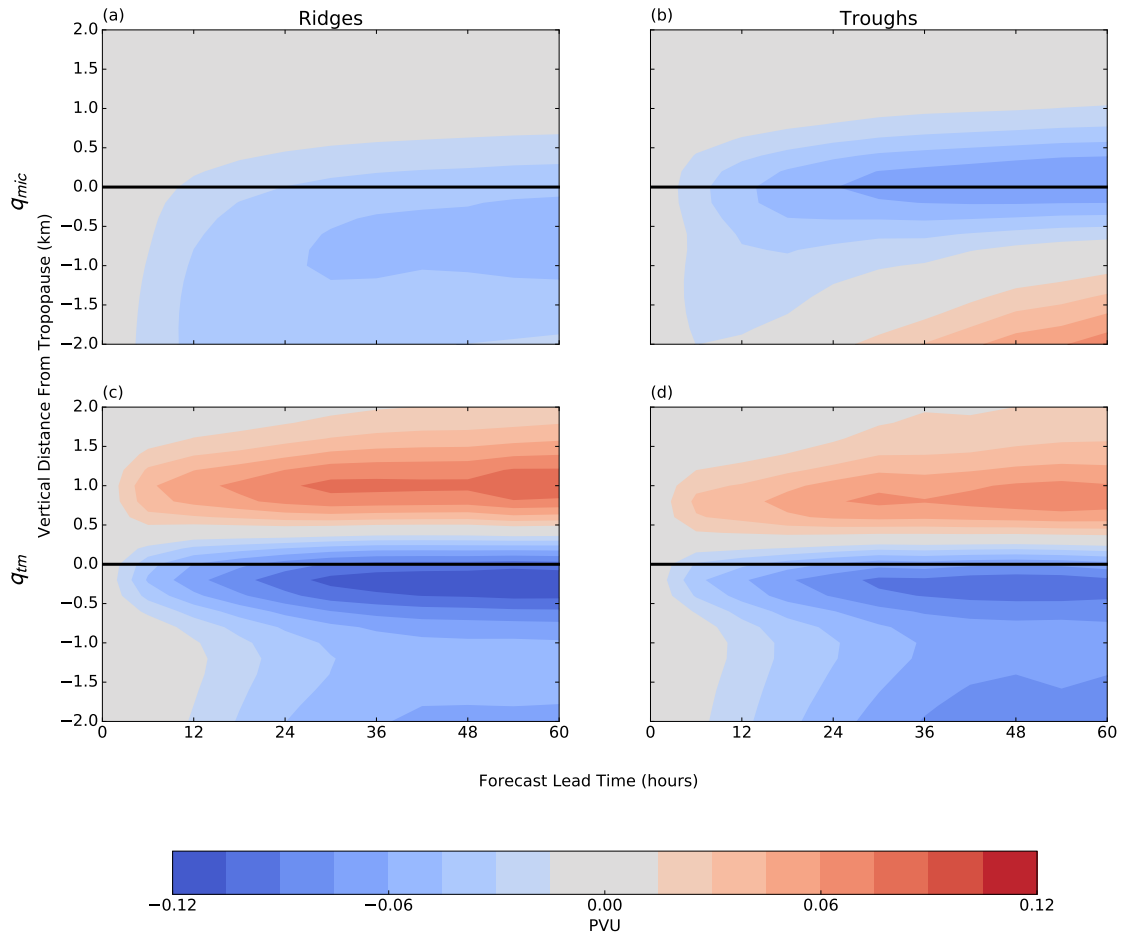


Figure 4.7: Microphysics (a and b) and turbulent mixing (c and d) PV tracers as a function of forecast lead time in ridges (a and c) and troughs (b and d). Values shown are the mean from the three-months of forecasts relative to the 2-PVU surface.

roughly net zero effect in troughs (Fig 4.2f) and a net positive in ridges (Fig 4.2c); however, this net positive is small and could be an artifact of large negative tendencies from gravity-wave drag causing the tropopause to be diagnosed too high which is then masked out in the composites (section 4.3).

4.5 Conclusions

Gray *et al.* (2014) showed that the tropopause PV gradient reduces with forecast lead time in NWP models; however, the source of model error remained unclear. In this study the systematic effects of individual model processes in maintaining the sharpness of the extratropical tropopause have been quantified by integrating PV tracers over a set of 92

forecasts with the MetUM. Since PV is conserved for adiabatic and frictionless flow ([Ertel, 1942](#)), PV tracers can accumulate tendencies of PV from individual model processes following the resolved flow. This can be advantageous when compared to calculating Eulerian initial tendencies ([Klinker and Sardeshmukh, 1992; Rodwell and Palmer, 2007](#)) by avoiding large cancellations in tendencies due to advection as will be the case near the tropopause. This study demonstrates that PV tracers can be a useful alternative to the initial tendencies method for quantifying the systematic behaviour of individual model processes.

Composites of PV tracers have been produced relative to the 2-PVU tropopause separately for ridges and troughs, diagnosed as anomalies of θ on the 2-PVU tropopause. Rossby waves are associated with meridional displacements of PV contours on isentropic surfaces which can be associated with an anomaly of θ on the 2-PVU tropopause.

The key results from this study are

1. The vertical PV contrast across the tropopause reduces relative to analyses with forecast lead time consistent with a smoothing of the isentropic PV gradient ([Gray et al., 2014](#)).
2. On the timescales of the forecasts, the advection scheme of the model gives an exponential decay of the tropopause PV contrast to a finite value with a timescale of 20-24 hours.
3. A key component of the PV budget is the dynamics-tracer inconsistency which quantifies the difference between the evolution of PV in the dynamical core and the evolution of PV through tracer advection ([Saffin et al., 2016](#)).
 - (a) The locations of the maxima in dynamics-tracer inconsistency are different when composited relative to the 2-PVU surface of the advection-only PV tracer rather than PV indicating that dynamics-tracer inconsistency is having a direct effect on mass transport across the tropopause causing the $q=2$ and $q_{adv}=2$ surfaces to separate.
 - (b) The dynamics-tracer inconsistency shows net negative tendencies near the tropopause level indicating a net transfer of mass from the stratosphere to the troposphere. This is consistent with numerical mixing removing small-scale

stratospheric filaments and could be related to vortex stripping ([Ambaum, 1997](#)).

4. Parametrized physical processes act to sharpen the tropopause by producing a dipole in PV tendencies across the tropopause with near zero net tendency at the tropopause, consistent with the results of [Chagnon et al. \(2013\)](#) and [Chagnon and Gray \(2015\)](#) from individual case studies.
 - (a) Radiative cooling produces net positive tendencies across and above the tropopause due to the gradient of water vapour across the tropopause. The stronger water vapour gradient and absolute vorticity in troughs compared to ridges results in a stronger net positive PV tendency. The positive PV tendencies due to radiative cooling have a stronger gradient across the tropopause in troughs than in ridges which can be explained by the increased frequency of clouds acting to sharpen the vertical cooling gradient ([Cau et al., 2005](#)).
 - (b) The microphysics PV tracer accumulates negative PV below the tropopause at short lead times associated with latent heating in WCBs.
 - (c) The turbulent-mixing PV tracer accumulates negative PV at the tropopause and positive PV above the tropopause. At short lead times the majority of the turbulent mixing PV tracer seen at tropopause levels accumulates locally rather than by the long-range transport from the boundary layer seen at longer timescales.

The open question now is what changes should be made to NWP models to improve the representation of the tropopause PV gradient? The work in this paper provides a framework for testing such changes. Here, a limited area domain has been used to give a resolution comparable to current global models at a lower computational cost; however, the inflow of air from the lateral boundaries results in an uncertainty in the behaviour of the tropopause as the PV tracers can not trace air prior to inflow. The recommendation for repeating this analysis to investigate model changes would be to use a global model but fewer forecasts.

An obvious first step would be to investigate changing model resolution. [Gray et al. \(2014\)](#) showed a reduction of PV gradient in day 10 of the ECMWF forecasts associated with a reduction in the horizontal resolution of the model. In this study a less dramatic

reduction in tropopause sharpness than [Gray *et al.* \(2014\)](#) is seen which is most likely because we have a higher resolution limited area domain (0.11° here compared to a range between $0.28 - 1.4^\circ$ for the forecasts analysed by [Gray *et al.* \(2014\)](#)). It would be useful to know if the model is accurately representing poorly resolved mixing processes. Varying the resolution of the forecasts should help identify errors arising from non-conservation of PV by the dynamical core and parametrized turbulence, both of which have been shown to be important processes at tropopause levels.

The magnitude of the systematic forecast error has been shown to be comparable to the tendencies due to the parametrized physical processes so it is plausible that realistic modifications to the model parametrization schemes could significantly reduce the error rather than more difficult measures such as increasing resolution or redesigning the dynamical core. It would be expected that modifying the microphysics and/or convection schemes to enhance the latent heating driven ascent in WCBs would have a large impact on the tropopause. It is useful to consider how changes to WCBs would affect the PV tracers. The simplest effect would be to directly enhance the negative PV tendencies below the tropopause at short lead times. Increased transport of moisture and cloud formation at tropopause levels would also modify the response of radiative tendencies. We did not find any significant errors in forecast of water vapour or clouds near the tropopause when compared with analyses (not shown) which suggests the WCB transport in the forecasts is adequate; however, this raises the question of how much we trust the analyses. ECMWF analyses have been shown to have a moist bias in the lower stratosphere ([Dyroff *et al.*, 2015](#)) and the ERA-Interim reanalyses have been shown to have insufficient cloud and a low cloud-top bias in WCBs ([Hawcroft *et al.*, 2016](#)). It is possible that an initial bias in the analyses is maintained through the forecasts leading to an underestimation of the effects of WCBs and long-wave radiation on the tropopause.

It is useful to associate systematic differences between forecasts and analyses with observations which is difficult for PV. The strength of the TIL ([Birner *et al.*, 2002](#)) is a useful measure of tropopause sharpness that can be obtained from observations. It is notable that studies on the processes affecting the TIL find similar results to studies on the processes affecting the tropopause PV gradient (e.g. [Chagnon *et al.* \(2013\)](#) and [Kunkel *et al.* \(2016\)](#)). Since static stability is proportional to the vertical gradient in θ , we would expect a region of enhanced static stability above the tropopause to be

associated with a positive PV anomaly and a stronger PV gradient. Pilch Kedzierski *et al.* (2016) showed that, without data assimilation, the TIL region in the ECMWF NWP model tends towards a weaker static stability which is probably associated with the decline in PV gradient shown by Gray *et al.* (2014); however, further work is needed to associate these two features. The recent North Atlantic Waveguide and Downstream Impact Experiment (NAWDEX) field campaign also provides an opportunity to compare observations and analyses of tropopause structure.

Chapter 5

Potential Vorticity Structure Near Lower Tropospheric Air Mass Boundaries

5.1 Introduction

Baroclinic instability can be described as the interaction between an upper-level Rossby wave on the tropopause and a low-level Rossby wave dominated by its θ signature near the lower boundary (Bretherton, 1966a). Surface friction acts to reduce baroclinic growth rates (Valdes and Hoskins, 1988). In terms of PV, friction can have large effects on the atmosphere through net sources and sinks of mass-weighted PV within the boundary layer (Haynes and McIntyre, 1987; Cooper *et al.*, 1992). Surface friction has been shown to result in positive PV anomalies in cyclones (Stoelinga, 1996) which reduce the cyclone growth rate by reducing coupling between upper and lower-level Rossby waves due to an increase in static stability (Adamson *et al.*, 2006). This “baroclinic mechanism” requires the contribution of Ekman pumping to shape the positive PV anomaly into one associated with static stability (Boutle *et al.*, 2015).

It is unclear whether boundary-layer parametrizations correctly represent the baroclinic mechanism or are simply tuned to produce the correct effect on cyclones through compensating errors (Boutle *et al.*, 2015). Parametrizations of boundary-layer turbulence are complex (e.g. Lock *et al.* (2000); see section 2.1.2.4) and require diagnosing different boundary-layer regimes to decide which type of semi-empirical turbulent-mixing profile to apply. Boundary-layer types, similar to those parametrized, can be determined from observations (Harvey *et al.*, 2013). The challenge for boundary-layer parametrizations is to reproduce the correct boundary-layer regimes, as determined from observations, while also producing the correct PV tendencies for affecting cyclone growth rates. In this chapter, the systematic PV tendencies affecting the boundary layer are quantified and methods for separating different regimes are explored.

The structure of this chapter is as follows. In section 5.2 ground-relative composites of PV tracers from the winter-season forecasts are presented to give an overview of the systematic effects of physical processes in the atmosphere. In section 5.3 a closer look is taken at surface processes by compositing relative to the top of the boundary layer. Section 5.4 explores using front-relative composites motivated by a change in behaviour of the PV tracers between the cold and warm sectors identified in section 5.3. The conclusions from this chapter are summarised in section 5.5.

5.2 Ground-relative Composites

Figure 5.1 shows the mean of the PV tracers as a function of height from the winter-season forecasts. The compositing method is the same as in section 4.4.1, but with height used as the vertical coordinate with a 1-km spacing. The lowest height shown is 1 km because the lowest model levels are dominated by large cancellations between processes which will be discussed in the following section. The signature of the tropopause is smoothed out by averaging in this way: there is a continuous increase in PV above 8 km with no localised sharp PV gradient (Fig. 5.1a). The net effects of diabatic processes are small compared to absolute values of PV: the profile of the advection-only tracer is almost identical to PV (Fig. 5.1a).

Figure. 5.1b shows the net effect of non-conservative processes ($q - q_{adv}$) and the partitioning into the following: parametrized physical processes ($\sum q_{phys}$), dynamics-tracer inconsistency (ε_I) and the budget residual (ε_r). The residual is small throughout the troposphere, but is increasingly positive above 13 km where it becomes comparable to other physical processes. This large residual is likely due to not properly accounting for the pressure solver in the PV budget as discussed in chapter 3. The net effect of the physics parametrizations is to accumulate positive PV tendencies near the surface and in the lower troposphere, negative PV tendencies in the upper troposphere, positive tendencies near tropopause levels and negative tendencies further up into the stratosphere. Dynamics-tracer inconsistency accumulates net negative PV tendencies everywhere which results in the positive PV accumulation diagnosed by $q - q_{adv}$ being much weaker than $\sum q_{phys}$. The net positive PV at tropopause levels in $\sum q_{phys}$ is roughly zero in $q - q_{adv}$ and the positive PV near the surface in $\sum q_{phys}$ actually becomes a net negative in $q - q_{adv}$.

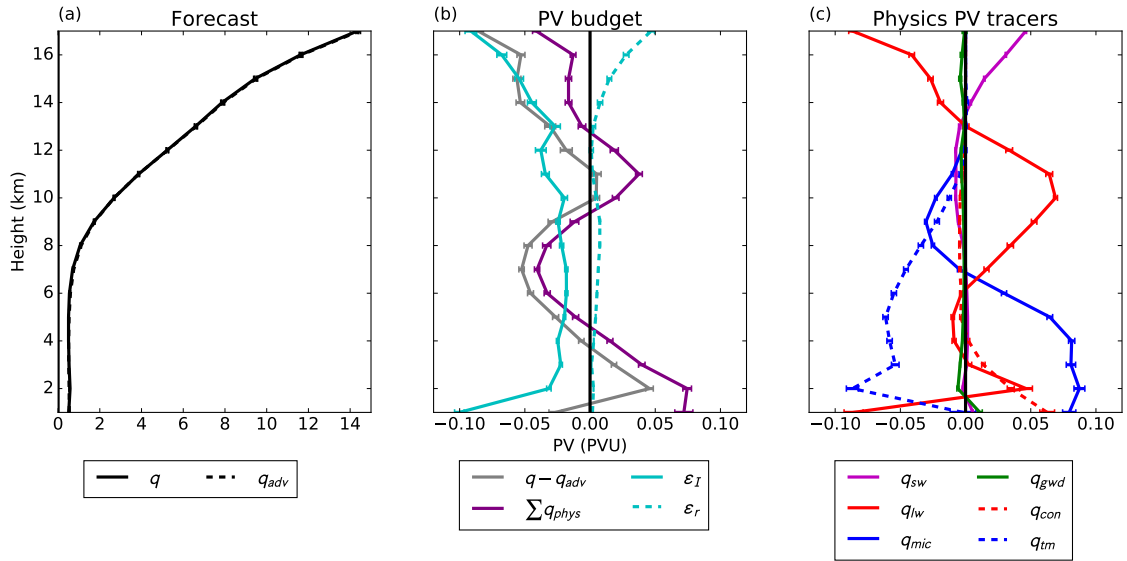


Figure 5.1: PV interpolated to height above mean sea level. Lines show the mean and error bars show the standard error on the mean for the 92 winter-season forecasts at 24-hours lead time. (a) Forecast values for PV (q) and the advection-only PV tracer (q_{adv}). (b) Difference ($q - q_{adv}$) and the contributing processes: parametrized physical processes ($\sum q_{phys}$), dynamics-tracer inconsistency (ε_I) and a residual (ε_r). (c) Contributions to $\sum q_{phys}$ from the individual physics tracers: short-wave radiation (q_{sw}), long-wave radiation (q_{lw}), microphysics (q_{mic}), gravity-wave drag (q_{gwd}), convection (q_{con}) and boundary-layer (q_{tbl}).

In the previous chapters it has been shown that the dynamics-tracer inconsistency can produce localised positive PV tendencies (Fig. 3.1) and net positive PV tendencies relative to the tropopause (Fig. 4.2); however, on height levels the average is always negative. Since non-conservative processes can produce no net tendencies in mass-weighted PV away from the boundaries (Haynes and McIntyre, 1987) a net negative dynamics-tracer inconsistency indicates either that tracer advection is increasing PV or the dynamical-core decreases PV at the upper and lower boundaries which is advected through the domain. Figure 5.2 shows the accumulated PV tendencies of the dominant processes from Fig. 5.1 as a function of forecast lead time. The strongest accumulations of dynamics-tracer inconsistency are at the boundaries of the composite with an increasing effect away from the boundaries with forecast lead time (Fig. 5.2b), although note that the boundaries of the composite (1 and 17 km) are not the same as the boundaries of the domain (0 and 80 km). In contrast, $q - q_{adv}$ largely shows a steady accumulation of PV tendencies

on each height level (Fig. 5.2a). This suggests that the dynamical core results in a net decrease in PV at the surface such that the net effect on PV is negative when averaged over height levels.

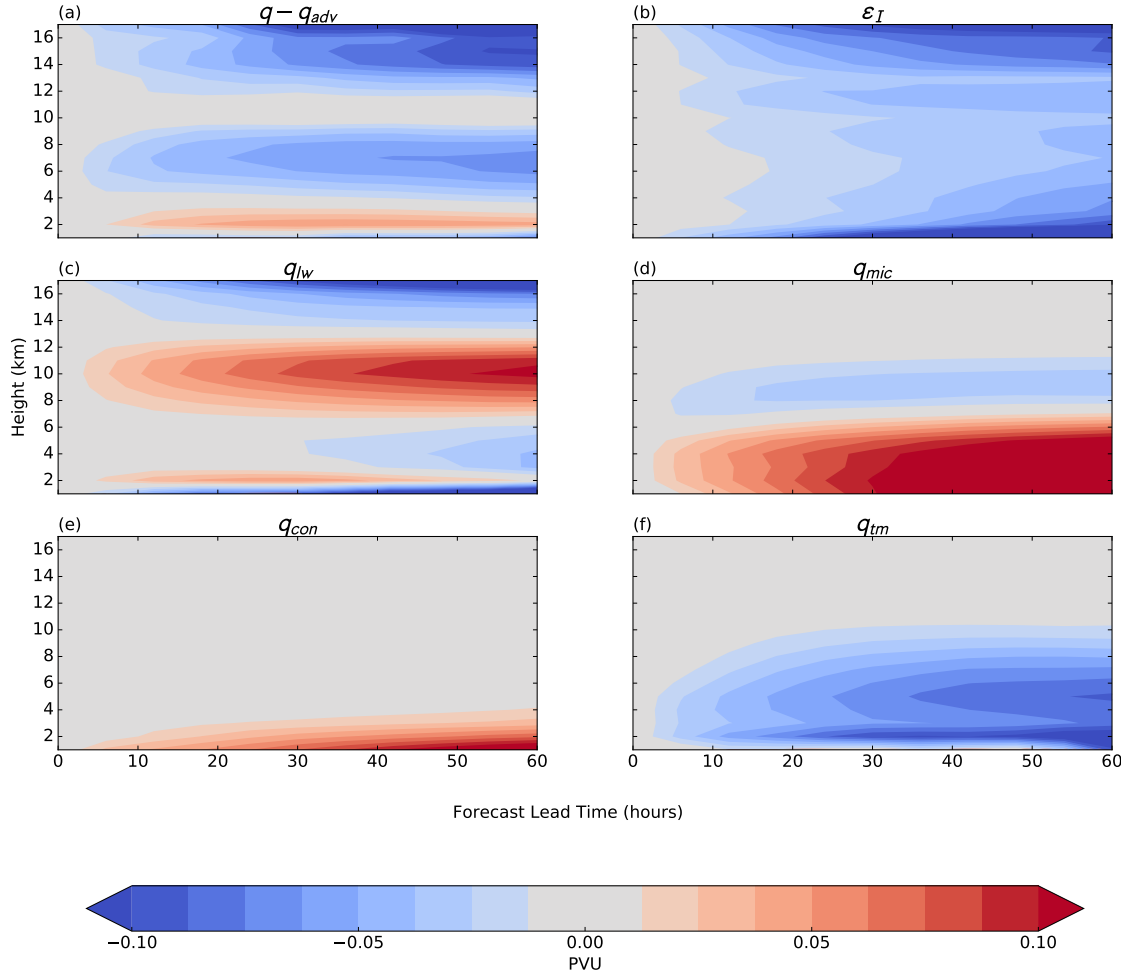


Figure 5.2: Dominant contributions to PV changes from the composites in Fig. 5.1 as a function of lead time for the 92 winter-season forecasts.

Figure 5.1c shows the contributions to $\sum q_{phys}$ from individual parametrized physical processes. Each of the parametrized physical processes gives systematic PV tendencies as a function of height with the exception of gravity-wave drag. Gravity-wave drag gives close to zero net effect on all height levels. This makes sense because gravity-wave drag acts on the horizontal winds on height levels: gravity-wave drag can produce large changes in PV but cancelling positive and negative changes over an individual height level.

The PV tracer for long-wave radiation accumulates positive PV from 6-13 km consistent with the decrease in humidity across the tropopause and presence of clouds further

below the tropopause. The PV tracer for short-wave radiation accumulates small negative PV over a similar height range which is also consistent with the water vapour decrease across the tropopause. Both the long-wave and short-wave radiation PV tracers show a change in sign at 13 km. Above 13 km the effects of short-wave heating from ozone in the stratosphere dominate the PV tendencies and there is an associated increase in long-wave cooling. A dipole in PV tendencies is expected across the maxima in short-wave heating from ozone with a dipole of the opposite sign from the long-wave cooling response. There are positive PV tendencies from short-wave radiation and negative from long-wave radiation at the top of Fig. 5.1 indicating that the vertical extent of the composites in Fig. 5.1 (17 km) is below the maxima in short-wave heating from ozone. Near the surface there is a peak in positive PV accumulation from long-wave radiation followed by negative below. Over time the negative tendencies dominate (Fig. 5.2c). This indicates that long-wave radiation results in net negative tendencies at the surface; however, long-wave radiation is generally expected to produce net positive PV tendencies by producing a mass flux into initially massless isentropic layers below the surface ([Cooper *et al.*, 1992](#)). This will be discussed further in the following section.

The PV tracer for microphysics accumulates positive PV in the lower troposphere and negative PV in the upper troposphere. This is consistent with a mid-level latent heating maxima. The change in sign in microphysics PV accumulation is at a similar height level to a change in sign for long-wave radiation. This is reasonable given the level of maximum latent heating will also be associated with increased cloud amounts. The zero point in PV accumulation from microphysics moves up with lead time because it is directly associated with ascending air masses (Fig. 5.2d). It is notable that the net positive PV tendencies accumulated by the microphysics PV tracer are much larger than the accumulated negative PV tendencies. From the impermeability theorem ([Haynes and McIntyre, 1987](#)), an isolated region of latent heating would be expected to produce roughly equal positive and negative PV anomalies; however, the composites are produced from many forecasts over a limited-area domain so this is not the case. Since the negative PV anomalies are associated with the top of diabatically enhanced ascent, they will also, on average, experience stronger horizontal winds and be advected out of the limited-area domain more rapidly. Therefore, the net positive PV tendencies accumulated by the microphysics PV tracer will be diagnosed as stronger than the accumulated negative PV

tendencies.

The PV tracer for convection accumulates positive PV tendencies at lower levels and small negative tendencies above. The negative PV accumulation is weaker because it is spread over many height levels and will also be associated with stronger horizontal winds, similarly to the microphysics PV tracer.

The PV tracer for turbulent mixing accumulates net negative PV in the lower troposphere. Similarly to the dynamics-tracer inconsistency, turbulent-mixing can produce localised positive PV tendencies and net positive PV tendencies above the tropopause, but net decreases in PV near the boundaries cancel out these effects when compositing on height levels. Unlike dynamics-tracer inconsistency, the minima is above the surface (Figs. 5.1c and 5.2f). This indicates that the net negative PV in the troposphere produced by turbulent mixing is related to positive PV tendencies at the surface not included in the composite. This will be shown in the following section.

5.3 The Boundary Layer

In the previous section many of the model processes showed distinct change in PV tendency near the surface. In this section the effects of different processes are investigated by compositing relative to the boundary-layer top. For further description of how the height and type of boundary layer are diagnosed see section 2.1.2.4. Figure 5.3 shows the diagnostics of boundary-layer height and type for the IOP5 and IOP8 case studies at 24-hours lead time. Note that the colourscale is saturated and some points can have diagnosed boundary-layer depths of >5 km. There is a lot of structure in the fields of boundary-layer height and type. The deepest boundary layers are just ahead of cold fronts trailing from low-pressure centres. These deep boundary layers are largely associated with gridpoints diagnosed as shear dominated. A coherent band of low boundary-layer heights (<0.5 km) can be seen in both case studies associated with the cold fronts. The frontal regions are fairly noisy with some points diagnosed as deep (>2.5 km) as well. The cold sector regions behind the cold front are distinctive as large regions of cumulus-capped boundary layers with intermediate ($\approx 1 - 2$ km) depths. Despite the distinctive structures in the boundary-layer height and type, the fields are very noisy and therefore would not be useful for dividing the domain into regions using an automated method.

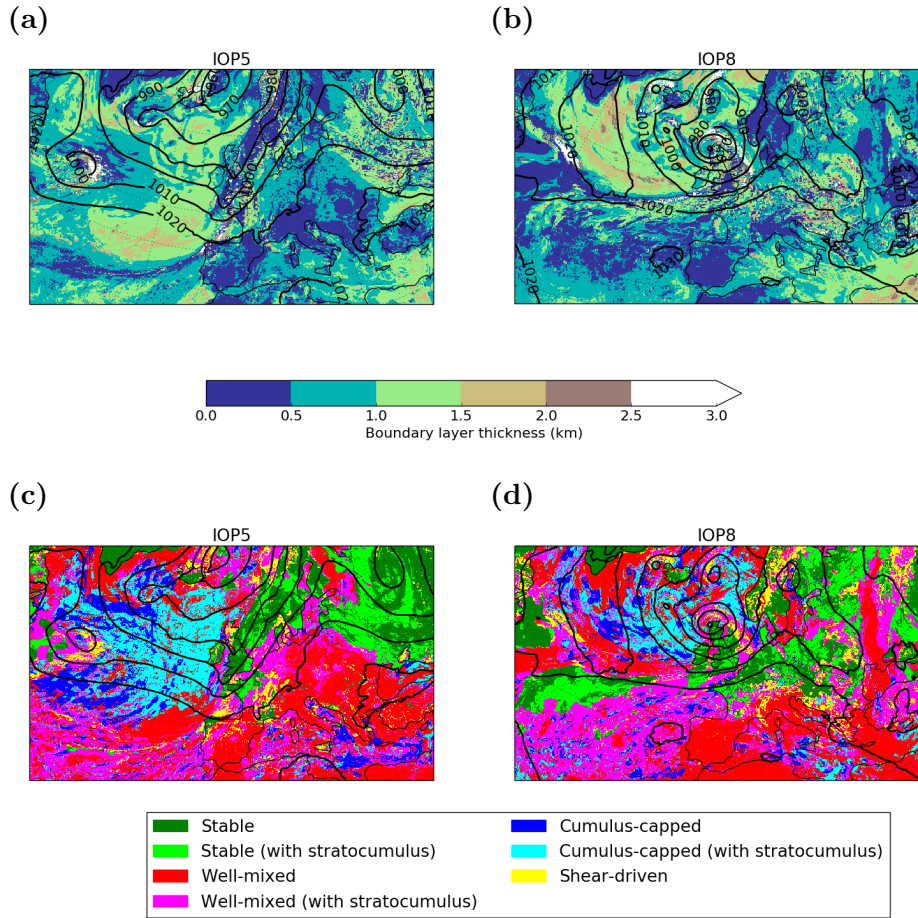


Figure 5.3: The diagnosed boundary-layer height (top panels) and boundary-layer type (bottom panels) from the MetUM turbulent-mixing scheme for forecasts run for the IOP5 (left panels) and IOP8 (right panels) case studies at 24-hours lead time. Black contours show the sea-level pressure.

To give an overview of processes occurring within and above the boundary layer, composites have been produced relative to the height of the boundary-layer top over the winter season forecasts (Figure 5.4). The compositing method is the same as in section 4.4.1, but with vertical distance from the top of the boundary layer used as the vertical coordinate with a 250-m spacing. For gridpoints with boundary-layer heights less than 1-km, points below ground are not included in the composites. There are large differences between the profiles of PV and advection-only PV (Fig. 5.4a). There is a distinct maximum in PV at the boundary-layer top that has mostly been removed from the advection-only PV tracer by this lead time (24 hours): the PV maximum at the top of the boundary layer is depleted by the advection scheme and maintained by diabatic processes. Within the

boundary layer, PV is, on average, less than the advection-only PV tracer. This indicates there is significant mixing across the boundary-layer top. Since the composites are close to the boundary, the only way for the advection-only PV tracer to increase within the boundary layer is through initially higher-valued PV air being mixed into the boundary layer. An important difference here, when compared to the tropopause-relative composites, is that the boundary-layer top does not act like a material surface. This means that it is difficult to distinguish whether the non-conservative processes reduce the initially higher-valued PV air before or after being mixed into the boundary layer; however, given the large contrast in profiles across the boundary-layer top the reduction is most likely dominated by processes occurring within the boundary layer.

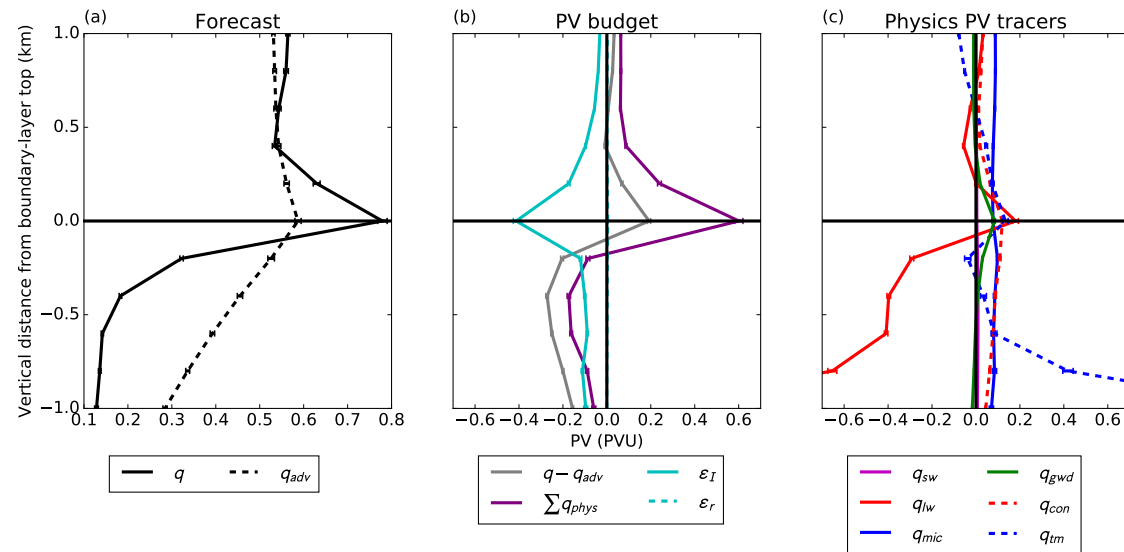


Figure 5.4: Composite average of PV as a function of distance from the diagnosed boundary-layer top. Lines show the mean and error bars show the standard error on the mean for the 92 winter-season forecasts at 24-hours lead time. (a) Forecast values for PV (q) and the advection-only PV tracer (q_{adv}). (b) Difference ($q - q_{adv}$) and the contributing processes: parametrized physical processes ($\sum q_{phys}$), dynamics-tracer inconsistency (ε_I) and a residual (ε_r). Note that ε_r is plotted but hard to see because it is negligible. (c) Contributions to $\sum q_{phys}$ from the individual physics tracers: short-wave radiation (q_{sw}), long-wave radiation (q_{lw}), microphysics (q_{mic}), gravity-wave drag (q_{gwd}), convection (q_{con}) and boundary-layer (q_{bl}).

Figure 5.4b shows the net effect of non-conservative processes ($q - q_{adv}$) relative to the boundary-layer top and the partitioning into the following: parametrized physical

processes ($\sum q_{phys}$), dynamics-tracer inconsistency (ε_I) and a residual (ε_r). The positive peak at the boundary-layer top is a result of the parametrized physical processes with a large negative cancellation from the dynamics-tracer inconsistency. Within the boundary layer, the net negative PV tendency is a result of similar contributions from parametrized physical processes and dynamics-tracer inconsistency.

Figure 5.4c shows the contributions to $\sum q_{phys}$ from individual parametrized physical processes relative to the boundary-layer top. The dominant processes in the boundary-layer are long-wave radiation and turbulent mixing which accumulate large net negative and positive PV tendencies respectively. Note that the two lines go off the x-axis scale shown in Fig 5.4c with the net accumulated PV tendencies approaching ± 1 PVU at 1 km below the boundary-layer top. The two terms largely cancel out with long-wave radiation giving slightly larger negative PV accumulation yielding a net negative PV accumulation of 0.1–0.2 PVU for the combined effects of the parametrized physical processes (Fig. 5.4b).

The cancellation between long-wave radiation and turbulent mixing below the top of the boundary layer appears to be generated at the surface. Figure 5.5 shows PV tracers on the bottom model θ -level at 24-hours lead time for the IOP5 case study and Fig. 5.6 shows the same for the IOP8 case study. There are large opposing PV accumulations from long-wave radiation and turbulent mixing in both case studies in the same regions as the cumulus capped boundary layers in the cold sector (Fig. 5.3c and d). Note the colourscale of ± 20 PVU is saturated at many gridpoints with some gridpoints approaching ≈ 1000 PVU. The two terms cancel out with much less net effect (Figs. 5.5a and 5.6a). The signs of the long-wave radiation and turbulent mixing are reversed in the warm sector. This is particularly pronounced for the low-pressure centres near the western boundary in both case studies.

Figure 5.7 shows PV tracers along the cross section AB in Fig. 5.5. This cross section was chosen to cut across the front and show the contrast between the cold and warm sectors. The front can be seen as the region of sloped θ_e contours in the centre of the cross section. On the cold side of the front the large cancellation between long-wave radiation and turbulent mixing can be seen at low levels. This cancellation is largely confined to the lowest model levels within the boundary layer consistent with the cancellation being diagnosed below the boundary-layer top over the winter-season forecasts (Fig. 5.4c). Figure 5.8 shows PV tracers along the cross section AB in Fig. 5.6. This cross section

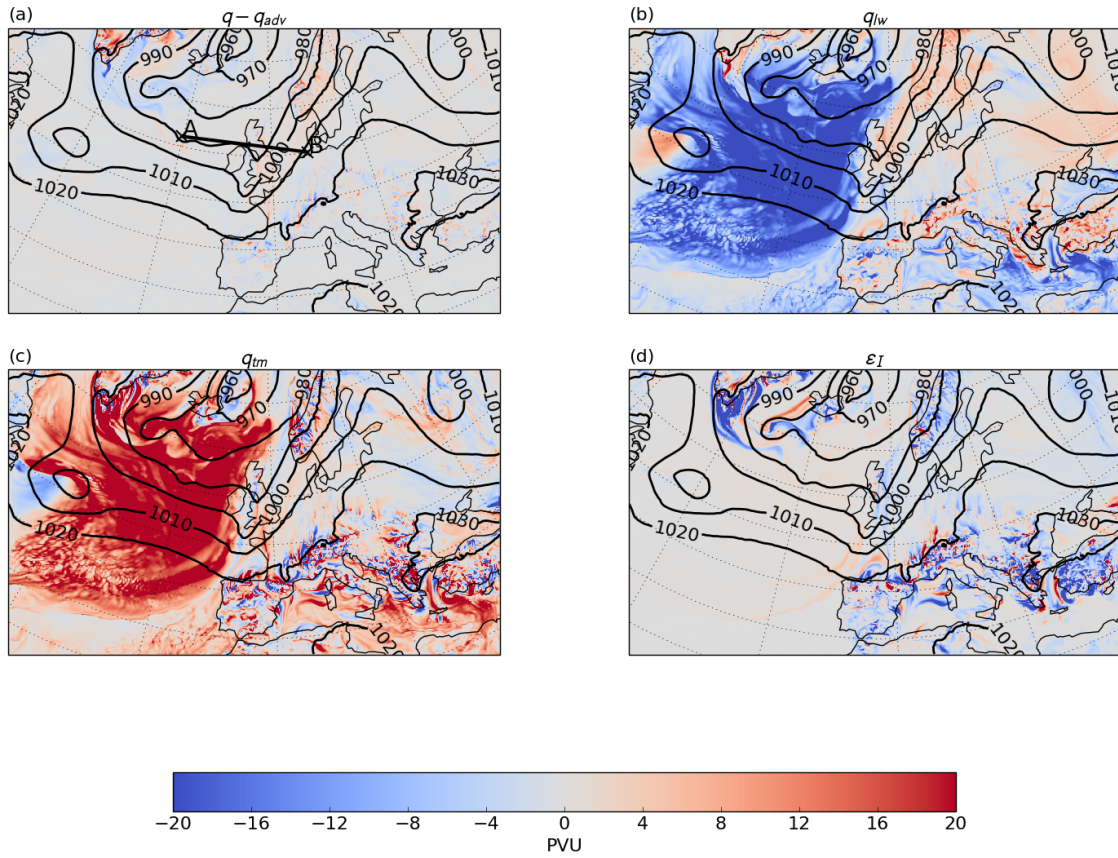


Figure 5.5: PV tracers on the bottom model θ -level for the forecast run for the IOP5 case study at 24-hours lead time (12 UTC on 29 November 2011). Contours show the mean sea-level pressure. (a) Total minus advection-only PV ($q - q_{adv}$). (b) Long-wave radiation PV tracer (q_{lw}). (c) Turbulent-mixing PV tracer (q_{tm}). (d) Dynamics-tracer inconsistency (ε_I).

was also chosen to show the contrast between the cold and warm sectors, but across the cyclone centre which is more complex than across the front in the previous cross section due to the wrapping up of the front. In this case, a region with a large cancellation between long-wave radiation and turbulent mixing can be seen up to ≈ 6 km near the cyclone centre due to the large resolved vertical winds advecting air out of the boundary layer.

The expectation from cooling at the surface is an increase in PV (Cooper *et al.*, 1992). Long-wave radiation only modifies θ , but gives negative PV tendencies at the surface. The structure of the long-wave radiation PV tracer in the cold sector can be explained by the cooling rate increasing rapidly with height in the lowest model levels

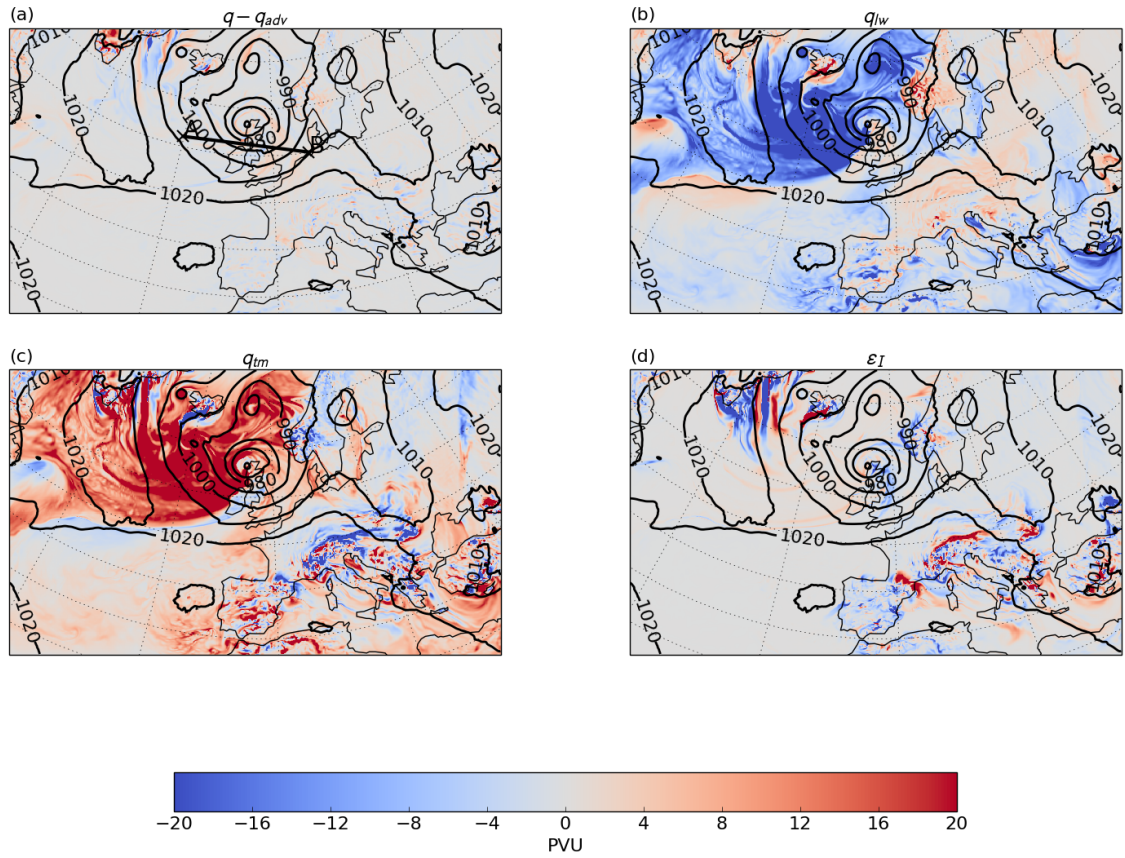


Figure 5.6: Same as Fig. 5.5, but for the forecast run for the IOP8 case study at 24-hours lead time (12 UTC on 8 December 2011).

such that the maxima in long-wave cooling is above the surface and decreases slightly to a constant cooling rate above. In this case there would be a PV decrease below the cooling maxima and a smaller increase above such as seen in Figs. 5.7b and 5.8b. Since the cancellation with the PV tendencies from the turbulent-mixing scheme is so close to zero it is likely that it is occurring within a single timestep. In this case the turbulent mixing, which occurs after long-wave radiation in a single timestep, acts to smooth out the θ profile which has been modified by long-wave radiation. For this to result in an increase in PV the vertical gradient of θ would have to be negative such that a smoothing of the θ profile is an increase in $\frac{\partial\theta}{\partial z}$ and therefore an increase in PV. Figure 5.9 shows the average θ profiles for each of the boundary-layer types. The cumulus-capped boundary layers, which were more likely to be associated with the cold sectors, have the strongest negative gradients of θ . This would explain why the cancellation is reversed in the warm sector: if the gradient of θ is positive in the warm-sector following long-wave radiation,

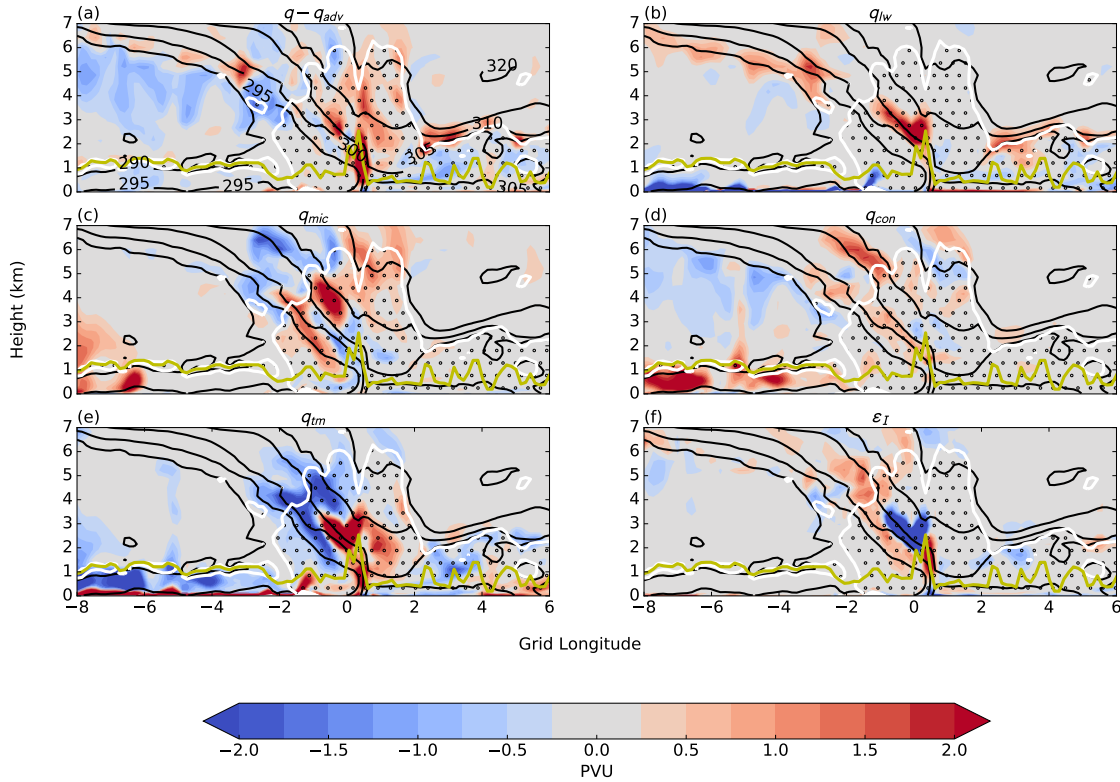


Figure 5.7: Cross section through AB in Fig. 5.5. Black contours show θ_e . The white contour and black dots indicates where the gridbox average relative humidity exceeds 80%. The yellow line shows the diagnosed boundary-layer height. (a) Total minus advection-only PV ($q - q_{adv}$). (b) Long-wave radiation PV tracer (q_{lw}). (c) Microphysics PV tracer (q_{mic}). (d) Convection PV tracer (q_{con}). (e) Turbulent-mixing PV tracer (q_{tm}). (f) Dynamics-tracer inconsistency (ε_I).

turbulent mixing near the surface will result in negative PV tendencies. In this case the long-wave radiative cooling would be largest at the surface.

Since turbulent mixing is more of a local process than radiation, it is expected that PV tendencies will generally occur in localised dipoles. This can be seen in Figs. 5.7e and 5.8e where the large positive PV accumulation near the surface is generally associated with negative PV accumulation above. These areas of negative PV accumulation are generally cancelled out by the convection PV tracer (Figs. 5.7d and 5.8d), although this is less clear in the centre of the front (Fig. 5.7) and near the cyclone centre (Fig. 5.8) where there are other processes occurring and stronger advective mixing. In a single timestep, convection occurs prior to turbulent mixing so it will be turbulent mixing that cancels out the effects

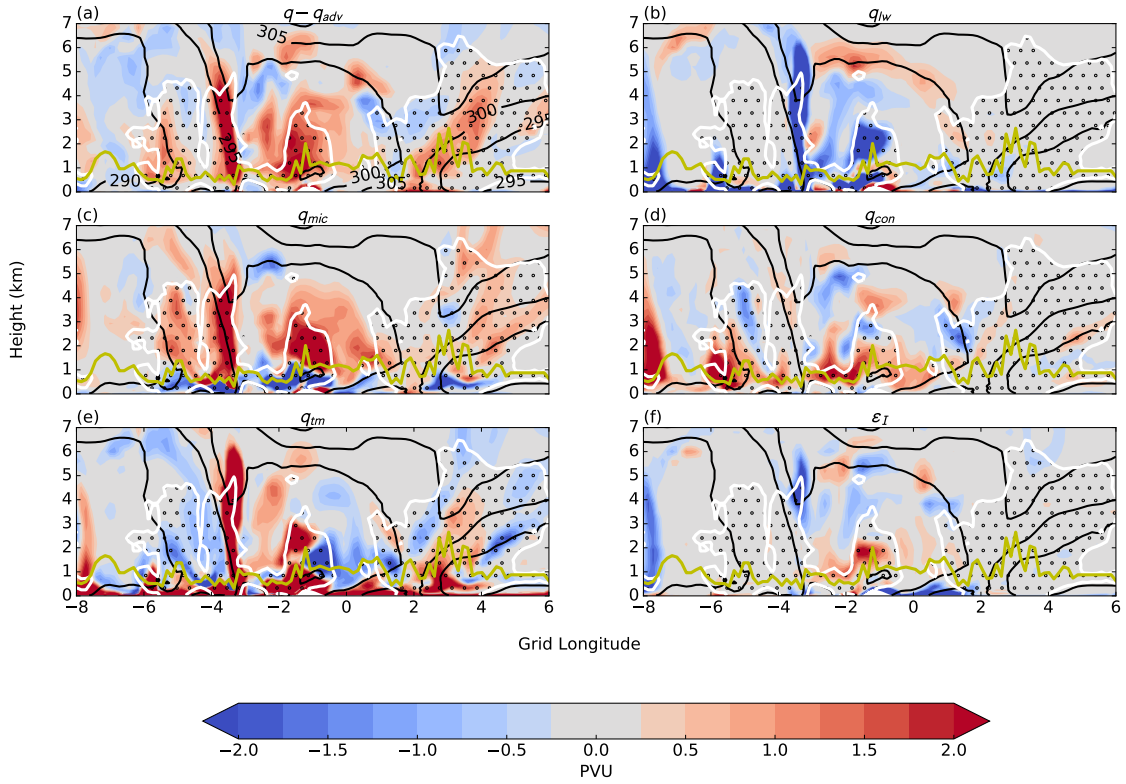


Figure 5.8: Same as Fig. 5.7, but for the cross-section through AB in Fig. 5.6.

of convection. The two processes are not completely separable since the diagnosis of the convective region is a part of the boundary-layer diagnosis. If this is occurring over a single timestep then the order of events would be as follows:

1. The profile of long-wave cooling results in a strongly negative θ gradient near the surface.
2. The boundary layer in this region is diagnosed as unstable with a convective region above (e.g. Fig. 5.3).
3. Convective mixing increases PV near the boundary-layer top and reduces PV above.
4. Turbulent mixing acts to restore the boundary-layer θ profile to be approximately the same as at the beginning of the timestep.

The net effect is that PV is decreased in the convectively unstable region above the boundary layer with little change within the boundary layer. This makes sense as the fast parametrized processes, convection and turbulent mixing, are designed to remove instabilities and move the model state towards an equilibrium.

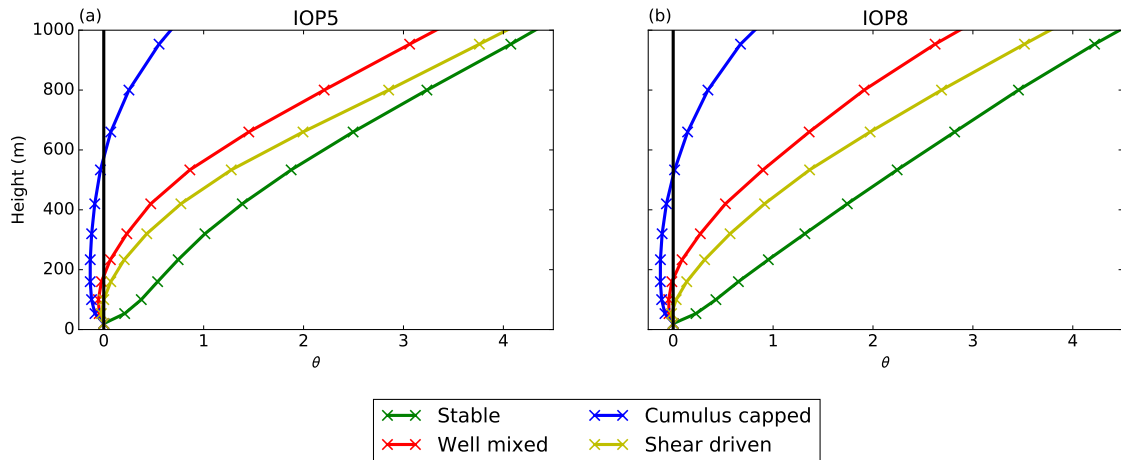


Figure 5.9: The average of θ as a function of model-level height for the (a) IOP5 and (b) IOP8 case studies at 24-hours lead time for different types of boundary layer. θ is plotted as the difference from the lowest model-level value. Note that the boundary-layer types with stratocumulus have been grouped with boundary-layer types without stratocumulus.

The peak in positive PV accumulation at the top of the boundary layer is a result of a combination of different parametrized physical processes: convection, gravity-wave drag, long-wave radiation and turbulent mixing all have a maxima at the boundary-layer top (Fig. 5.4c). The other physical processes, microphysics and short-wave radiation, do not produce much structure across the boundary layer. Microphysics accumulates similar positive PV tendencies regardless of whether the air is in the boundary layer or not. The PV tendencies from short-wave radiation near the boundary layer are negligible compared with the other parametrized physical processes.

The peak in positive PV accumulation at the boundary-layer top from convection can be explained as a part of the response to long-wave radiation at the surface in the cold sector, but this does not explain the maxima from other physical processes at the boundary-layer top. There are large positive PV tendencies from turbulent mixing; however, if this was part of the response to long-wave radiation then there would be cancelling negative PV tendencies from long-wave radiation at the boundary-layer top rather than net positive (Fig. 5.4c).

Figures 5.10 and 5.11 show PV tracers interpolated to the height of the diagnosed boundary-layer top for the IOP5 and IOP8 respectively to give an overview of where different processes are affecting the boundary-layer top. As expected, the positive values

of the convection PV tracer are located in the cold sector (Figs 5.10d and 5.11d) with cancelling negative values in the turbulent-mixing PV tracer (Figs 5.10c and 5.11c).

The remaining processes which have a positive peak at the boundary-layer top appear be dominated by large local values associated with high orography (Figs. 5.10, 5.10b, c, e and f). In both case studies, dynamics-tracer inconsistency is largely cancelling out the effects of the other three processes, although there are still some net PV changes (Figs. 5.10a and 5.10a). This explains the large cancellation between the parametrized physical processes ($\sum q_{phys}$) and dynamics-tracer inconsistency (ε_I) seen at the boundary-layer top with a smaller positive net PV change ($q - q_{adv}$) (Fig. 5.4b). A potential issue with these PV tendencies is that the calculation of PV does not properly account for terrain-following coordinates. In this case, large values of dynamics-tracer inconsistency would be expected. This is because the dynamical core will “see” and update the PV related to terrain-following coordinates, but the tracer-advection scheme is given the diagnosed PV which does not account for terrain-following coordinates; therefore, an inconsistency between the dynamical core and tracer advection is inevitable if terrain-following coordinates are not properly accounted for.

5.4 Fronts

In the previous section, substantial differences in the accumulated effects of parametrized physical processes between the cold and warm sectors of cyclones were identified. In this section a front-relative framework is investigated for compositing PV tracers separately in warm and cold sectors. The automated front detection algorithm of [Hewson \(1998\)](#), based on gradients of θ_w , has been used to produce climatologies of fronts (e.g. [Berry et al. \(2011\)](#)); however, at higher resolutions, such as in the simulations in this thesis, small-scale features lead to the front detection algorithm being unreliable. This has been noted by [Jenkner et al. \(2010\)](#) who used the detection method of [Hewson and Titley \(2010\)](#) on smoothed fields of θ_e and tuned the frontal strength parameter to the higher resolution data. In this section the front in the IOP5 case study is investigated, rather than using an automated front detection method over the winter-season forecasts.

In the previous section, the frontal region in the IOP5 case study could be seen as sloped contours of θ_e . In this section a value of $\theta_e=300$ K from the centre of the frontal

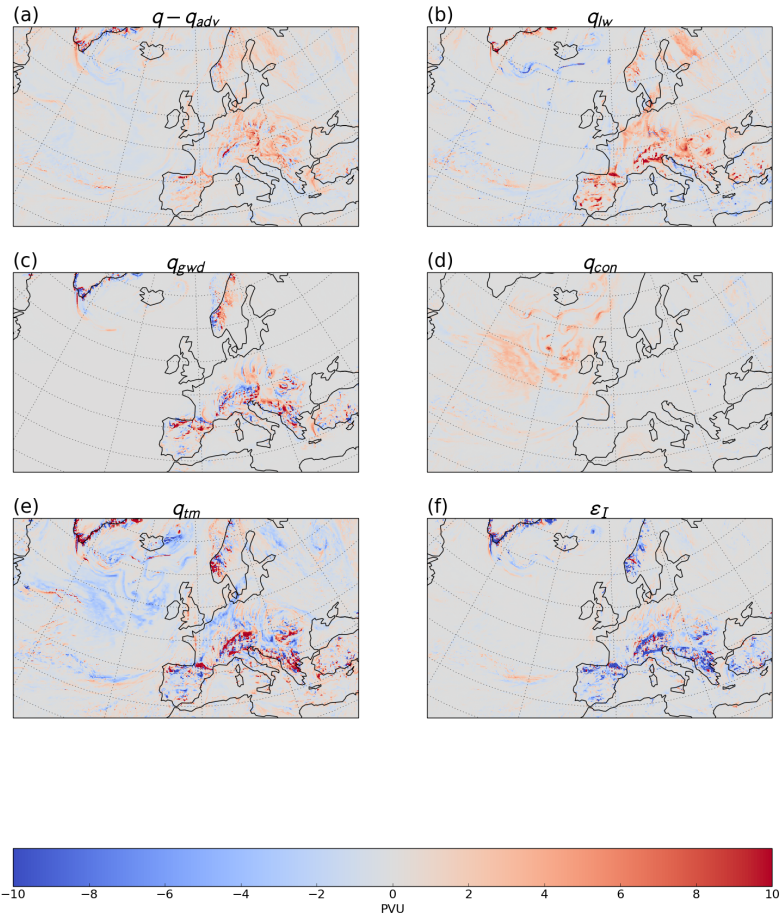


Figure 5.10: PV tracers interpolated to the height of the top of the boundary layer for the forecast run for the IOP5 case study at 24-hours lead time (12 UTC on 29 November 2011). (a) Total minus advection-only PV ($q - q_{adv}$). (b) Long-wave radiation PV tracer (q_{lw}). (c) Gravity-wave drag PV tracer (q_{mic}). (d) Convection PV tracer (q_{con}). (e) Turbulent-mixing PV tracer (q_{tm}). (f) Dynamics-tracer inconsistency (ε_I)

region is used to identify the frontal surface. Figure 5.12 shows θ_e for the IOP5 case study. The colourscale is centered on $\theta_e=300$ K to distinguish between the cold and warm sectors. The cross sections show that a value of $\theta_e=300$ K is consistent along the length of the front. The warm sector is narrow: there are low-level areas of $\theta_e<300$ K on the warm side of the front (Figure 5.12d). The vertical extent of the frontal region, where the $\theta_e=300$ K contour is steepest, varies along the front between 5–7 km.

The region shown by the dashed box in Fig. 5.12 is selected to produce a composite in the front region. The mass-weighted average of PV tracers in the gridboxes in this region are taken binned by the gridbox pressure every 25 hPa. Figure 5.13 shows the composite

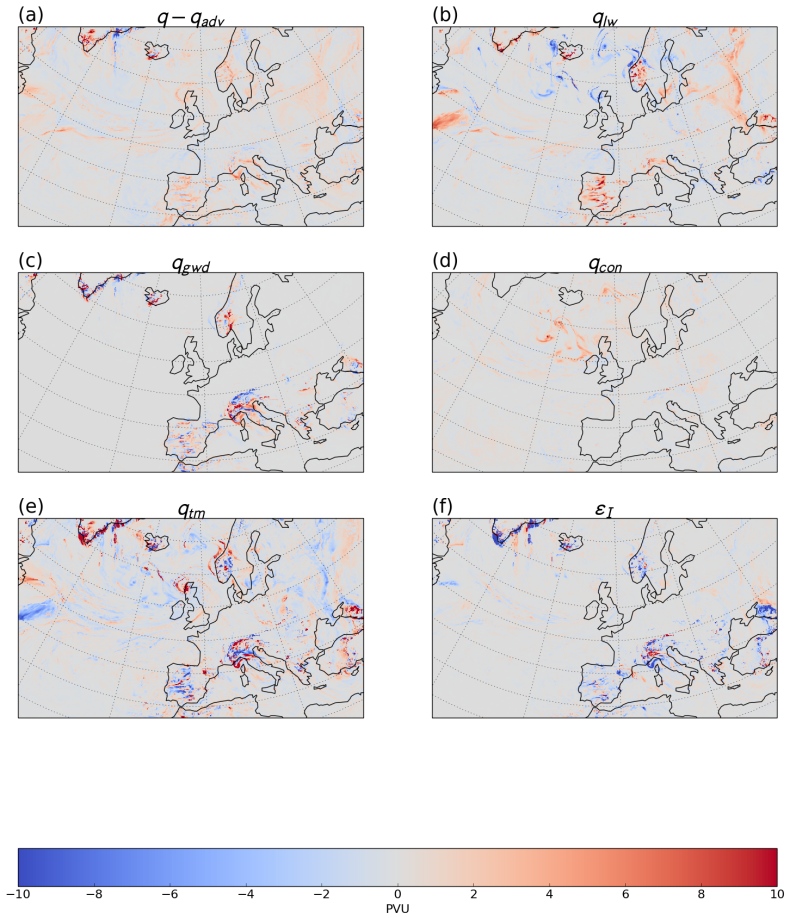


Figure 5.11: Same as Fig. 5.10 but for the forecast run for the IOP8 case study at 24-hours lead time (12 UTC on 8 December 2011).

over the region shown in Fig. 5.12a for the warm ($\theta_e > 300$ K) and cold ($\theta_e < 300$ K) sectors separately. The vertical PV structure is different between the cold and warm sectors. The cold sector has roughly constant PV up to ≈ 550 hPa, where the average PV over the cold sector increases associated with the upper-level trough, and the warm sector has a mid-level PV maxima. [Vannière et al. \(2016\)](#) showed that the low-level cold-sector region could be identified by its negative PV. The negative PV in the cold sector is below the composite in Fig. 5.13 so would not be useful for separating the cold and warm sectors due to the sloped frontal surface.

Figures 5.13b and e show the net effect of non-conservative processes ($q - q_{adv}$) and the partitioning into the following: parametrized physical processes ($\sum q_{phys}$), dynamics-tracer inconsistency (ε_I) and a residual (ε_r) for the warm and cold sectors respectively. In both the warm and cold sectors the net effects of dynamics-tracer inconsistency and the

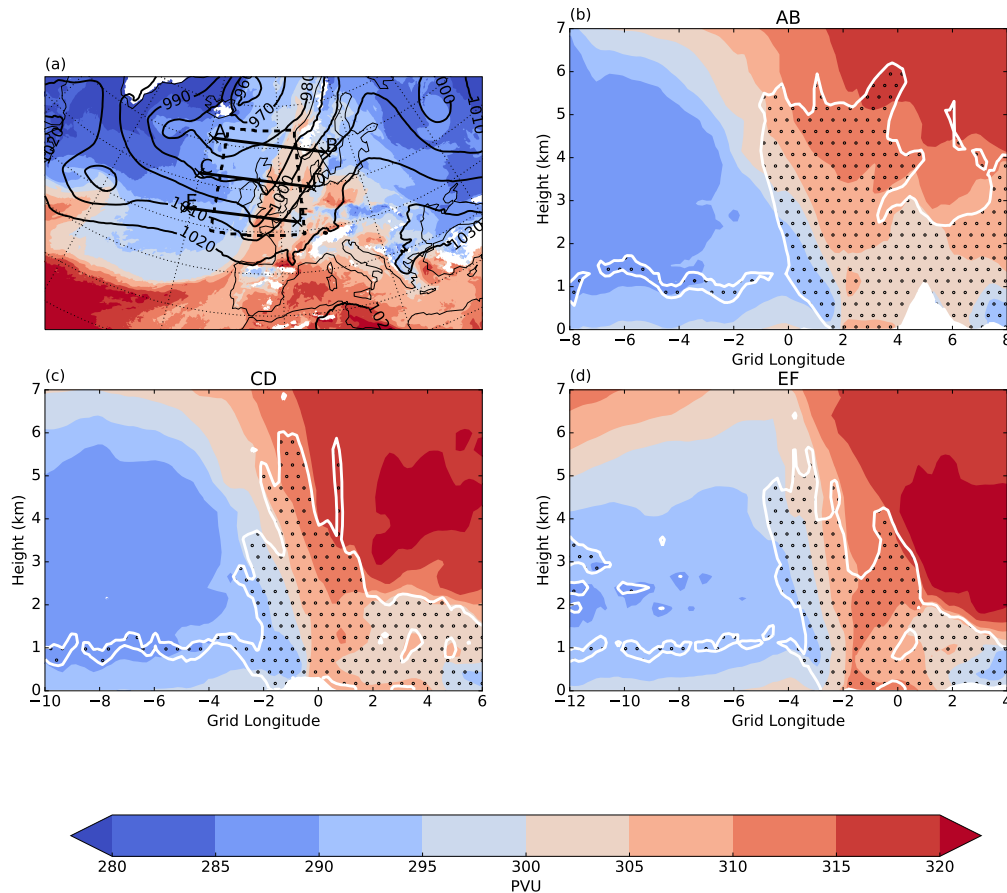


Figure 5.12: θ_e for the forecast run for the IOP5 case study at 24-hours lead time (12 UTC on 29 November 2011). (a) 900 hPa map and cross-sections through (b) AB, (c) CD and (d) EF on (a). Contours on (a) show mean sea-level pressure every 10 hPa. The white contour and black dots on (b, c, d) indicate where the gridbox average relative humidity exceeds 80%.

residual PV are small with the parametrized physical processes providing the dominant contribution to $q - q_{adv}$. It is somewhat surprising that the net effect of dynamics-tracer inconsistency is so small in the sharp gradient region of the front; however, the dynamics-tracer inconsistency does accumulate large local positive and negative tendencies (Fig. 5.7f). The net effects of parametrized physical processes are different between warm and cold sectors: net positive PV tendencies are accumulated in the warm sector which peak at ≈ 750 hPa whereas net negative PV tendencies are accumulated in the cold sector which peak higher up, at ≈ 600 hPa. Below, PV tracers are shown on three different pressure levels, 900, 750 and 600 hPa, to identify the different physical processes contributing to PV changes.

Figures 5.13c and f show the contributions to $\sum q_{phys}$ from individual parametrized physical processes for the warm and cold sectors respectively. Note that the x-axis is different to that in Figs. 5.13b and e. The cancellation between convection and turbulent-mixing is maximised at ≈ 900 hPa in the cold sector, with a smaller, and opposite, cancellation between long-wave radiation and turbulent-mixing in the warm sector. Figure 5.14 shows PV tracers at 900 hPa zoomed in on the region of the front. The large cancellation between convection and turbulent-mixing can be seen on the cold side of the front (Figs. 5.14d and e). The region of the cancellation has much larger scale than the front and extends further west than the composite region. The positive PV tendencies from turbulent mixing identified in the warm sector at this level are mostly confined to being along the front (Figs. 5.14e). The cancelling negative PV tendencies from long-wave radiation are more large scale and spread over the warm sector indicating that the two processes are not related in this region. Note that the region of positive long-wave radiation PV tracer cancelled by the turbulent-mixing PV tracer over France is diagnosed as being in cold sector because $\theta_e < 300$ K. The negative PV tendencies due to long-wave radiation at this level are most likely associated with the cloudy ascending warm conveyor belt region.

The positive diabatic PV accumulation in the warm sector peaks at ≈ 750 hPa. Figure 5.15 shows PV tracers at 750 hPa zoomed in on the region of the front. The positive PV accumulation at this level is associated with long-wave radiation displaced from the front and turbulent mixing local to the front (Fig. 5.15b and e). The positive PV associated with long-wave radiation is coaligned with the edge of the cloudy region rather than being directly associated with the front. In the warm sector, turbulent mixing produces positive and negative PV tendencies which cancel in the composite leading to long-wave radiation being diagnosed as the dominant contribution to the positive PV tendencies (Fig. 5.13c). The net negative diabatic PV in the cold sector at this pressure level is associated with convection consistent with the response to long-wave cooling discussed in the previous section. There is also positive PV accumulated by the convection PV tracer at this level in the cold sector with cancelling negative PV accumulated by the turbulent-mixing PV tracer. This region is where the cumulus-capped boundary layer is deeper (Figs. 5.3a and b) resulting in the cancellation between convection and turbulent mixing at the boundary-layer top occurring at higher levels.

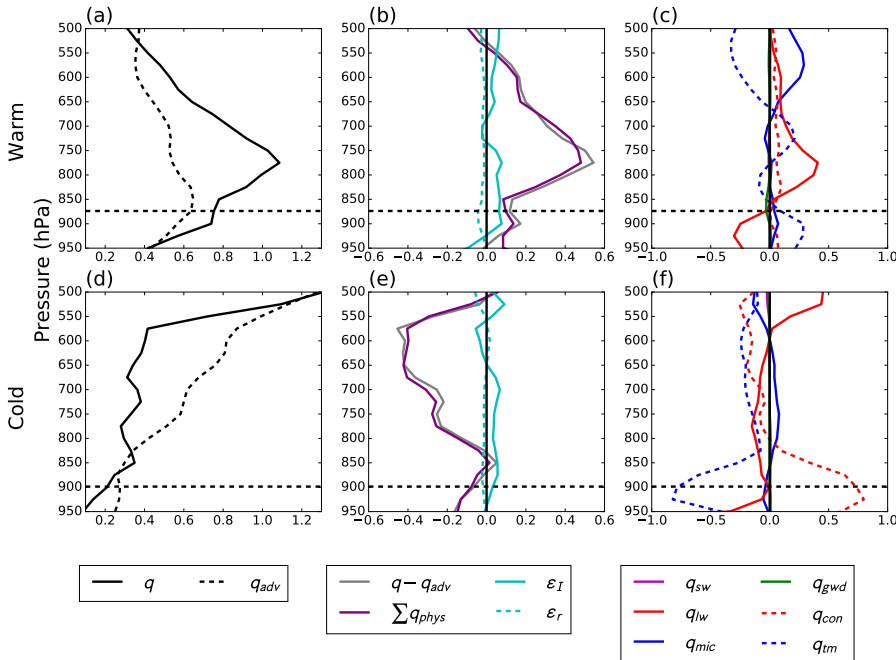


Figure 5.13: Front-relative composites for the forecast run for the IOP5 case study at 24-hours lead time (12 UTC on 29 November 2011). Composites are in the region shown in Fig. 5.12a for regions designated as (a,b,c) warm sector ($\theta_e > 300$ K) and (d,e,f) cold sector ($\theta_e < 300$ K) separately. The dashed lines show the average pressure level of the boundary-layer top. (a) and (d) show the forecast values for PV (q) and the advection-only PV tracer (q_{adv}). (b) and (e) show the difference ($q - q_{adv}$) and the contributing processes: parametrized physical processes ($\sum q_{phys}$), dynamics-tracer inconsistency (ε_I) and a residual (ε_r). (c) and (f) show the contributions to $\sum q_{phys}$ from the individual physics tracers: short-wave radiation (q_{sw}), long-wave radiation (q_{lw}), microphysics (q_{mic}), gravity-wave drag (q_{gwd}), convection (q_{con}) and boundary layer (q_{bl}).

The negative diabatic PV accumulation in the cold sector peaks at ≈ 600 hPa. Figure 5.16 shows PV tracers at 600 hPa zoomed in on the region of the front. Similarly to at 750 hPa, there is a large region of negative PV accumulation from convection, but with additional contributions from microphysics and turbulent mixing across the front. The microphysics has accumulated net positive PV tendencies in the warm sector and net negative PV tendencies in the cold sector at this level (Fig. 5.13c and f) which is evident in Fig. 5.16c; however, the positive and negative values of the microphysics are close to the front and so the overall contributions in each sector will be sensitive to the diagnosis of the frontal surface. The diagnosis of the effects of turbulent mixing will be

similarly sensitive to the diagnosis of the frontal surface. The turbulent-mixing PV tracer has accumulated net negative PV tendencies at this level across the $\theta_e=300$ K surface. The effects of turbulent mixing within the front are better visualised by the cross section (Fig. 5.7e) where it can be seen that the turbulent mixing has resulted in a dipole of PV along the frontal surface that is not clearly a part of the warm or cold sector.

5.5 Conclusions

The effects of parametrized physical processes across air mass boundaries in the lower troposphere, the boundary-layer top and fronts, have been quantified. Ground-relative composites over the set of 92 winter-season forecasts have been produced to give an overview of the systematic effects of physical processes in the atmosphere. Air-mass boundaries are smoothed out in the composites relative to fixed locations. By compositing relative to air-mass boundaries the effects of physical processes acting in different regimes can be identified. It is still unclear whether turbulence parametrizations correctly represent the processes generating PV anomalies in the boundary layer ([Boutle et al., 2015](#)); therefore, diagnosing the effects of parametrized physical processes on the boundary layer is important for better understanding the role of model errors. Previous studies of PV tendencies in the boundary layer have focused on individual case studies (e.g. [Stoelinga \(1996\)](#)) or idealised simulations (e.g. [Adamson et al. \(2006\)](#); [Plant and Belcher \(2007\)](#)). Here, the systematic effects of different physical processes in the boundary layer have been quantified.

Boundary-layer relative composites show that there is a net PV decrease in air within the boundary layer relative to the advection-only PV tracer indicating that initially higher-PV air is being mixed into the boundary layer where the PV is then decreased. The diagnosed PV tendencies within the boundary layer are dominated by a large cancellation between negative PV tendencies due to long-wave radiation and positive PV tendencies due to turbulent mixing. The cancellation is located in the cold sectors. In the cold sector regions the cumulus convection scheme is active with a large cancellation between negative PV tendencies from the turbulent-mixing scheme and positive PV tendencies from the convection scheme near the boundary-layer top and negative PV tendencies from the convection scheme above the boundary-layer top. The net effect of long-wave radiation, convection and turbulent-mixing in the cold sector is to reduce PV above the boundary

layer with little overall change within the boundary layer.

A PV maximum at boundary-layer top, associated with diabatic processes, is also identified in the boundary-layer relative composites. Long-wave radiation, convection, gravity-wave drag and turbulent-mixing PV tracers all have maxima at the boundary-layer top. Long-wave radiation, gravity-wave drag and turbulent-mixing have strong positives over high orography which is largely cancelled by dynamics-tracer inconsistency. This cancellation is likely an artifact of the PV calculation not accounting for terrain-following coordinates. The maximum in PV accumulated by the convection PV tracer at boundary-layer top is associated with a cancelling negative PV accumulation from the turbulent-mixing PV tracer as part of the response to long-wave cooling in the cold sector discussed above.

Front-relative composites can be used to separate cold and warm sectors. A front relative composite for the IOP5 case study was produced by manually identifying a surface of constant θ_e as the frontal surface. There was a net positive diabatic PV accumulation on the warm side of the front with a maximum at ≈ 750 hPa associated with gradients of long-wave cooling at the cloud edge which was displaced from the front itself. There was a net negative PV accumulation on the cold side of the front with a maximum at ≈ 600 hPa associated with cumulus convection in the cold sector in response to long-wave cooling at the surface (discussed above). The effects of the microphysics and turbulent-mixing schemes are more local to the front rather than being distinctly separated into the cold and warm sectors so composites over many fronts would be required to identify systematic effects. Climatologies of fronts can be produced from objective front identification methods based on thermal gradients ([Hewson, 1998](#); [Berry *et al.*, 2011](#)); however, at high resolution, such as used in this thesis, smoothing of the initial fields and tuning of parameters are required to avoid diagnosing noise as fronts ([Jenkner *et al.*, 2010](#)). A combination of the concept of a front as a surface of constant θ_e and objective front identification methods, which could diagnose the optimal θ_e value, could prove useful for assessing the systematic effects of processes on fronts in high-resolution data.

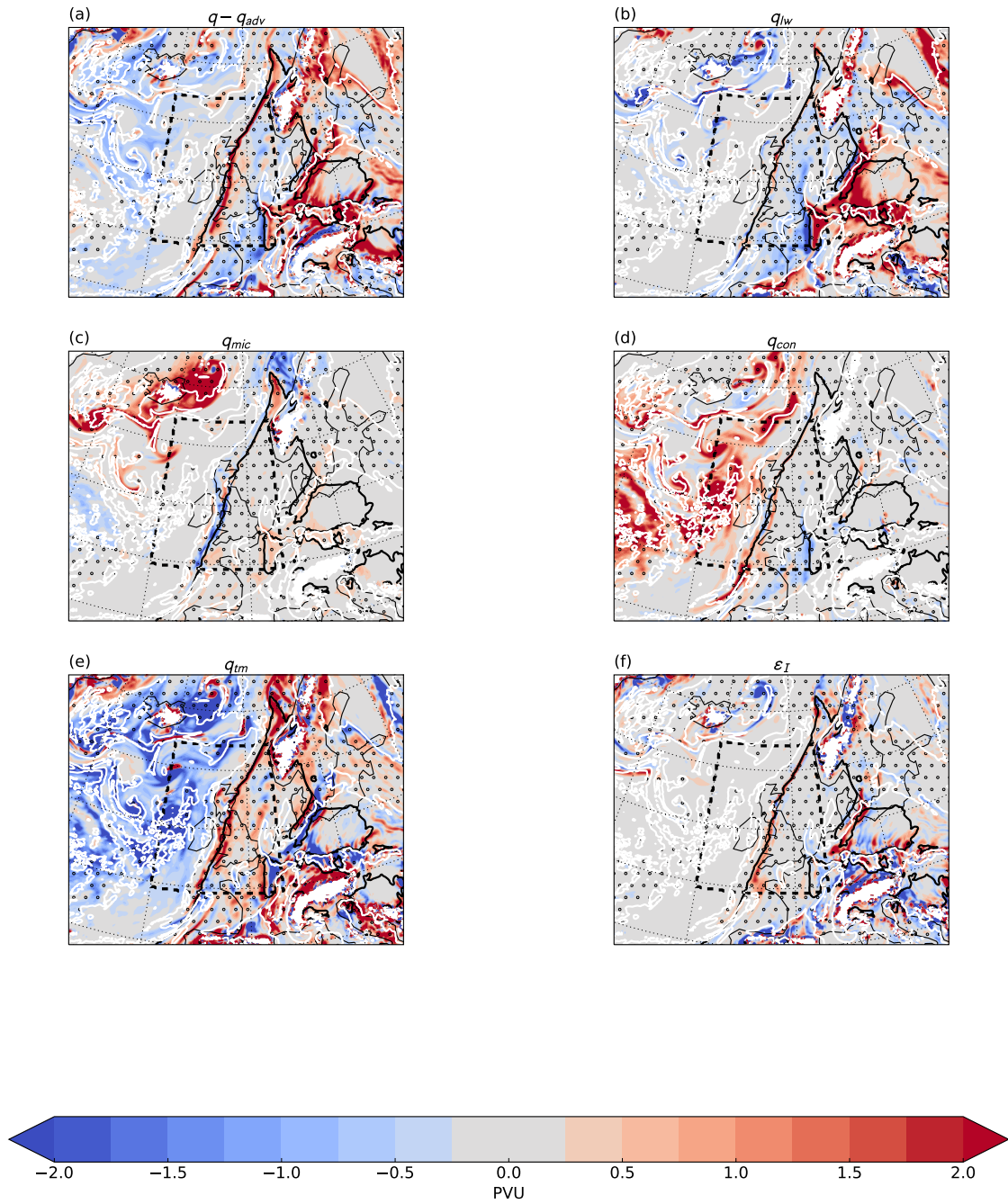


Figure 5.14: PV tracers at 900 hPa for the forecast run for the IOP5 case study at 24-hours lead time (12 UTC on 29 November 2011). Contour shows $\theta_e=300$ K. The white contour and black dots indicates where the gridbox average relative humidity exceeds 80%. (a) Total minus advection-only PV ($q - q_{adv}$). (b) Long-wave radiation PV tracer (q_{lw}). (c) Microphysics PV tracer (q_{mic}). (d) Convection PV tracer (q_{con}). (e) Turbulent-mixing PV tracer (q_{tm}). (f) Dynamics-tracer inconsistency (ε_I). Note that the colourscale is saturated for many gridpoints in each plot.

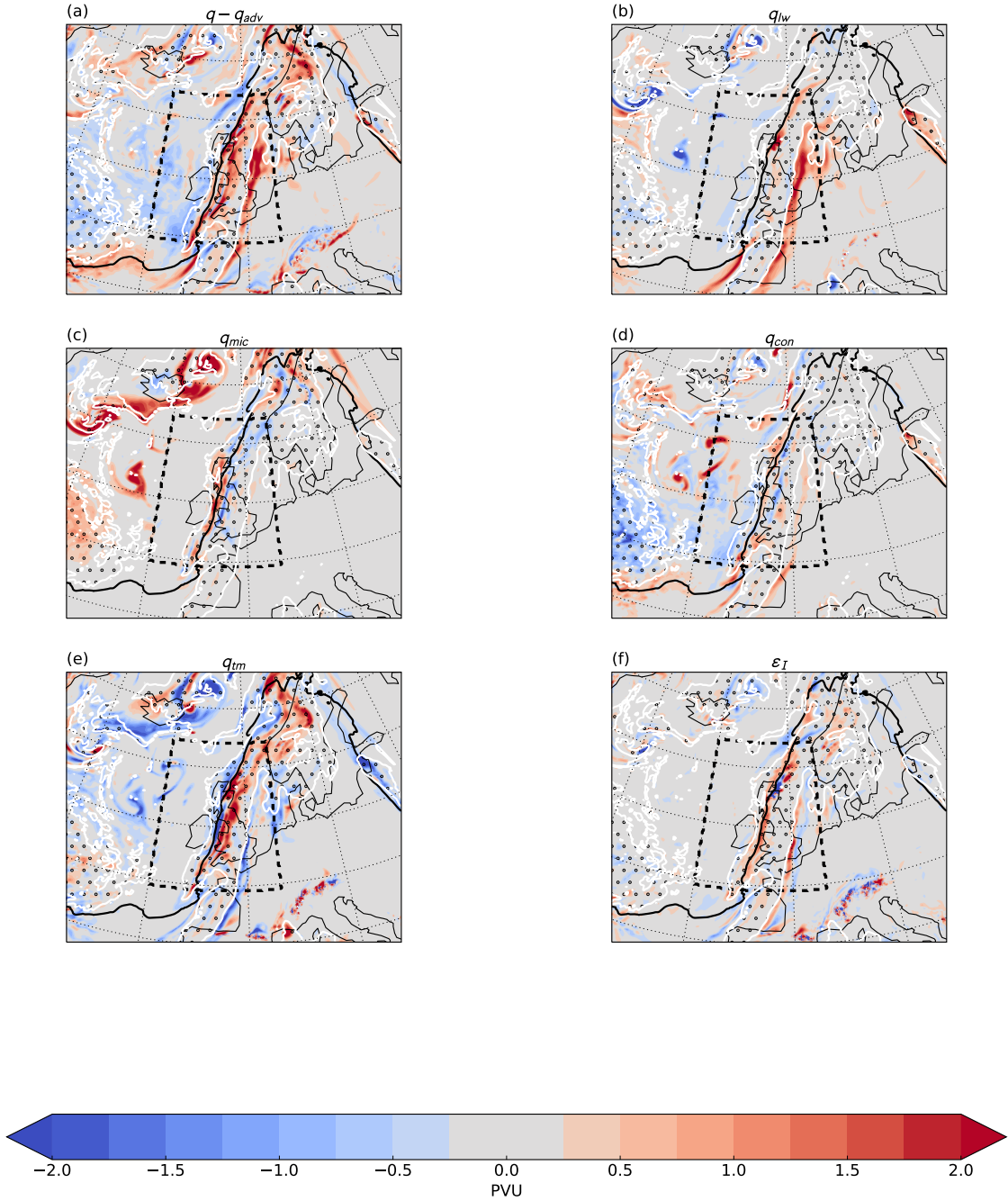


Figure 5.15: Same as Fig. 5.14, but at 750 hPa.

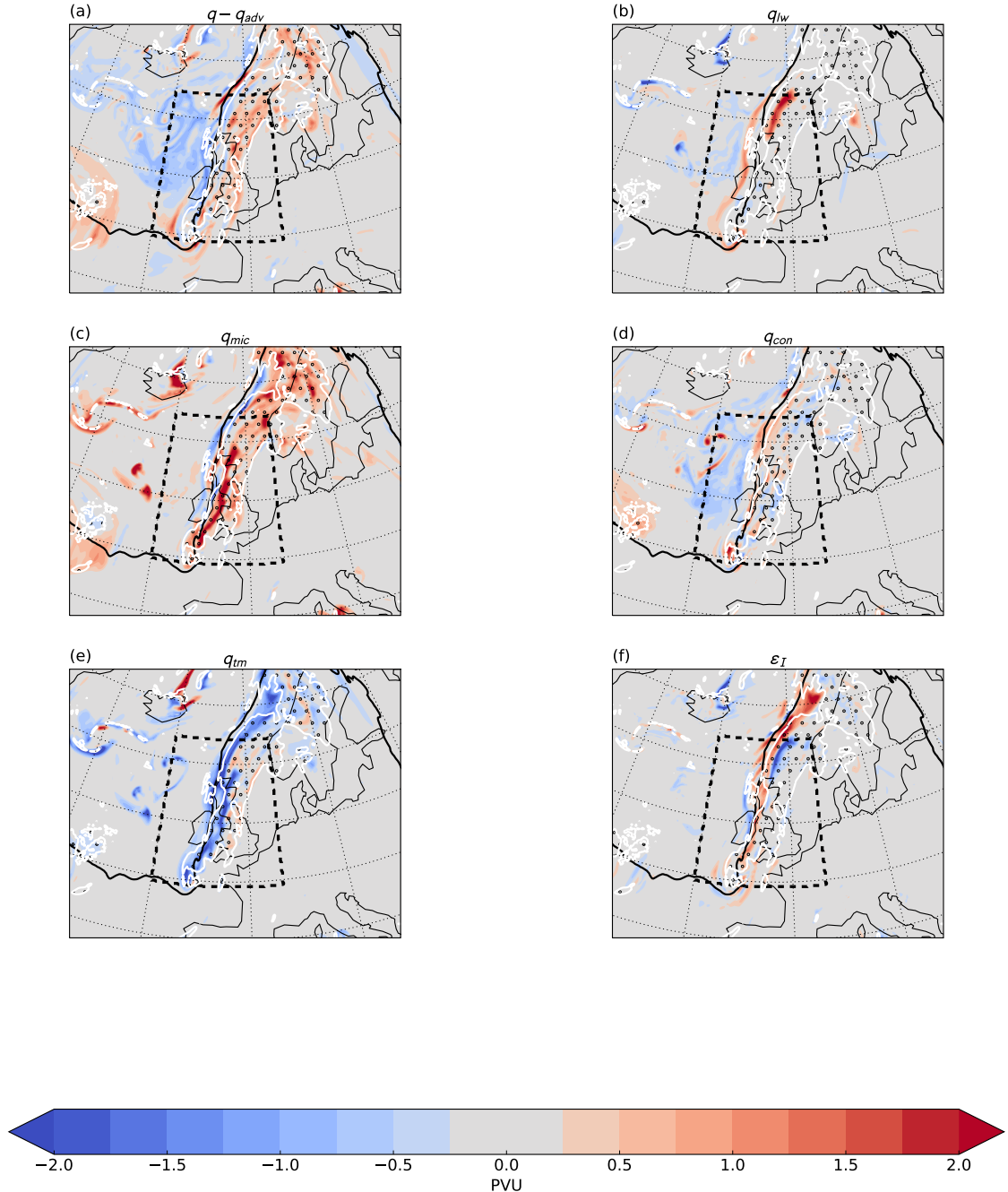


Figure 5.16: Same as Fig. 5.14, but at 600 hPa.

Chapter 6

Conclusions

6.1 Conclusions

The overarching scientific question this thesis aims address is **what changes should be made to a numerical model to reduce systematic forecast errors?** To answer this question, PV tracer diagnostics in the MetUM have been used to quantify the effects of different model processes and better understand how they affect features in the atmosphere. Each work chapter in this thesis relates to one of the research questions, introduced in chapter 1, and the key conclusions from each are discussed below. For more detailed discussion of the results see the conclusions section in the respective chapters.

1. What are the sources of PV non-conservation in numerical models?

For the PV tracers to be used to link forecast errors with the processes responsible they must accurately quantify the sources of PV non-conservation. Previously, the formulation of the PV tracers did not account for non-conservation of PV by the dynamical core. This was shown in Chapter 3 to result in a residual in the PV tracers of the same order of magnitude as the dominant parametrized physics tracers. This residual results in an uncertainty in the effects of parametrized physical processes diagnosed by the PV tracers. A dynamics-tracer inconsistency diagnostic was derived from an exact budget of PV, in terms of the PV tracers, and implemented in the MetUM. The dynamics-tracer inconsistency was shown to reduce the residual in the PV tracers by an order of magnitude and to be largely a result of non-conservation of PV by the dynamical core.

The dynamics-tracer diagnostic is based on the study of [Whitehead *et al.* \(2015\)](#) where the inconsistency between dynamical cores and tracer-advection schemes were quantified in terms of PV for idealised simulations. [Whitehead *et al.* \(2015\)](#) showed there were significant differences in the diagnosed inconsistency for different dynamical cores and tracer-advection schemes. Although [Whitehead *et al.* \(2015\)](#) argued that the inconsistency should be reduced, zero dynamics-tracer inconsistency is not necessarily a desirable

feature of a dynamical core. Conservation of PV at the model grid scale will effectively block the turbulent cascade to subgrid scales (Thuburn, 2008). The dynamics-tracer inconsistency can be thought of as quantifying how small-scale mixing results in a different behaviour in PV compared to tracer advection; however, there is also a contribution of model error. PV is not a prognostic variable in the MetUM: it is diagnosed as the non-linear combination of multiple prognostic variables. Therefore, stepping forward several prognostic equations and diagnosing PV will inevitably result in non-conservation.

The residual in the PV tracers was previously a large limitation on the use of PV tracers: the residual represented an uncertainty in the diagnosed accumulation from parametrized physical processes since its origin was not identified. By attributing the majority of the residual to dynamics-tracer inconsistency the uncertainty in the effects of parametrized physical processes has been reduced. This not only allows the PV tracers to be used in future studies with increased certainty, but also adds weight to previous studies that have used PV tracers to quantify the effects of parametrized physical processes. The results of chapter 3 show that the dynamical core dissipation should be considered alongside parametrized physical processes and enables comparison of the dynamical core behaviour in a realistic forecast context.

2. Why does tropopause sharpness reduce with forecast lead time?

Recent work has shown that the sharpness of the extratropical tropopause declines with lead time in operational numerical weather prediction models (Gray *et al.*, 2014), indicating an imbalance between processes acting to sharpen and smooth the tropopause. In Chapter 4 the systematic effects of different processes affecting the sharpness of the tropopause were quantified.

The effects of different processes on the tropopause were discussed in terms of the known mechanisms affecting tropopause sharpness. A sharp tropopause PV gradient can be formed and maintained by vortex stripping on an isentropic surface combined with radiative relaxation maintaining a PV contrast between the equator and pole (Ambaum, 1997; Haynes *et al.*, 2001). In the atmosphere, diabatic processes can contribute directly to an enhanced tropopause PV gradient through long-wave cooling (Forster and Wirth, 2000; Cavallo and Hakim, 2009) and latent heating in warm conveyor belts (Chagnon *et al.*, 2013). The net result is that the advection scheme results in an exponential decay of tropopause PV gradient towards a finite value with a timescale of 20-24 hours, con-

sistent with timescales associated with chaotic advection ([Methven and Hoskins, 1999](#)), and the net effect of parametrized physical processes is to partially counteract this decline by enhancing the tropopause PV gradient. The results extend those of [Chagnon et al. \(2013\)](#) and [Chagnon and Gray \(2015\)](#) who showed that diabatic processes result in dipoles of diabatically-generated PV enhancing the tropopause PV gradient in individual case studies. Here, the diabatic PV dipole was shown to be a systematic feature of the midlatitude tropopause over many forecasts.

An objective diagnostic to separate ridges and troughs was introduced and used to produce separate composites of the PV tracers relative to the tropopause. The forecast error in tropopause PV gradient was shown to be larger in ridges associated with a more rapid reduction in PV gradient by the advection scheme and a weaker effect of long-wave radiation on the tropopause in ridges; however, more work is needed to directly associate these processes with model error.

3. What are the systematic effects of parametrized physical processes across other air-mass boundaries?

In chapter [5](#) the effects of different processes on air-mass boundaries in the lower atmosphere, specifically the boundary-layer top and fronts, were investigated. Ground-relative composites were also produced to give an overview of the systematic effects of physical processes in the atmospheric column.

The PV tracers have been used previously to show that turbulent mixing results in a positive PV anomaly near a cyclone centre ([Stoelinga, 1996](#)) which results in a decrease in cyclone strength by reducing coupling between upper and lower-level Rossby waves ([Adamson et al., 2006](#)). These previous results have been limited to individual case studies and idealised simulations. In this thesis, the systematic effects of different processes modifying PV has been quantified.

In the simulations in this thesis, the contribution of turbulent mixing to positive PV anomalies in the boundary layer is less clear. The diagnosed PV accumulation within the boundary layer is dominated by a cancellation between long-wave radiation and turbulent-mixing. The cancellation is largely confined to cold sectors where long-wave cooling produces negative PV tendencies at the surface which are subsequently cancelled out by the turbulent-mixing scheme. There is also an associated cancellation between positive PV tendencies from cumulus convection and negative PV tendencies from the

turbulent-mixing scheme. Overall, there is very little net change in PV in the boundary layer and a decrease in PV above the boundary layer in the region of convection that is attributed to the convection scheme. The parametrization schemes are representing a dynamic equilibrium: the boundary layer is continually destabilised by radiative cooling which drives turbulent mixing and convection. This demonstrates a limitation in separating “initial tendencies” into individual processes because all three processes are responsible for the negative PV tendencies; however, the PV tracers do give insight into how the model represents this dynamic equilibrium.

Composites were produced relative to the boundary-layer top. A PV maximum was identified at the boundary-layer top associated with positive PV tendencies from various physical processes. Some of the contributing processes (long-wave radiation, gravity-wave drag and turbulent mixing) are associated with large diagnosed PV tendencies over high orography that are largely cancelled by the diagnosed dynamics-tracer inconsistency. This result is most likely due to the PV calculation in the PV tracers diagnostics not properly accounting for terrain-following coordinates.

A front-relative composite for a case study was produced manually by identifying a surface of constant θ_e as the frontal surface. A net negative PV tendency in the cold sector maximises at around 600 hPa associated with cumulus convection and a net positive PV tendency in the warm sector maximises at around 750 hPa associated with gradients in long-wave radiation at the edge of the cloudy region. The effects of the microphysics and turbulent-mixing schemes acted more locally to the front rather than being distinctly separated into the cold and warm sectors.

In summary, the PV tracer diagnostics have been put forward as a potentially insightful diagnostic for linking forecast errors with the processes responsible. The “dynamics-tracer inconsistency” was shown to be an important component of the PV budget if the PV tracers were to be used to diagnose the effects of different processes (chapter 3). The systematic effects of different model processes on the tropopause sharpness (chapter 4), which is systematically underrepresented in numerical weather prediction models ([Gray et al., 2014](#)), and on the boundary layer (chapter 5), which is typically represented with overly-simplified parametrizations in numerical weather prediction models ([Boutle et al., 2015](#)), have been quantified. The work in this thesis provides the groundwork for various future studies which will, I hope, contribute to the continual reduction of forecast errors.

6.2 Future work

Four open science questions arising from the work in this thesis have been identified.

1. What is the typical magnitude and structure of dynamics-tracer inconsistency in other models?

In chapter 3 a dynamics-tracer inconsistency diagnostic was derived and implemented in the MetUM. Unlike the PV tracers for parametrized physical processes, dynamics-tracer inconsistency is not clearly linked to a physical process occurring in the atmosphere and is potentially more sensitive to model formulation. The dynamics-tracer inconsistency also quantifies how small-scale mixing results in a different behaviour in PV compared to tracer advection. Comparisons of the dynamics-tracer inconsistency diagnostic between different models, with different dynamical cores, and different resolutions could help distinguish the effects of small-scale mixing from model specific dissipation and potentially model error. A simple comparison could be done with MetUM: the current version of the MetUM has the “ENDGame” dynamical core (Wood *et al.*, 2014) which differs from the “New Dynamics” dynamical core used in the simulations in this thesis (Davies *et al.*, 2005).

2. What changes to numerical models would reduce the forecast error in tropopause sharpness?

In chapter 4 the dominant processes affecting the tropopause sharpness were quantified. The processes were discussed in terms of the mechanisms affecting the tropopause sharpness to better understand what changes might improve the model error in tropopause sharpness. Some of the potential changes are discussed in the conclusions of chapter 4. The results of chapter 4 provide a framework for assessing the effects of changes to the model on the sharpness of the tropopause by checking whether changes to model processes improve the maintenance of the tropopause PV gradient and quantifying how this is achieved.

3. How do lateral boundary conditions affect the sharpness of the tropopause?

The simulations in this thesis have used a limited area domain to allow for higher resolution at lower computational cost. In chapter 4 the tropopause PV contrast was shown to decrease systematically with forecast lead time, consistent with Gray *et al.* (2014); however, the effect of the advection scheme on the tropopause sharpness is not separated from the effects of the boundary conditions. One way to remove this ambiguity would be to repeat the simulations for a global domain. An alternative, that complements the PV

tracer diagnostics, would be to implement a Lagrangian tracer that tracks air from the lateral boundaries. This way composites could be produced over air that started within the domain and air that has come through the lateral boundaries. This approach could also be used with the PV tracers for investigating features other than the tropopause.

4. What are the systematic effects of parametrized physical processes across fronts?

In chapter 5 the effects of different processes relative to a front were quantified for an individual case study. The composite showed distinct differences in processes acting on the warm and cold sides of the front; however, composites over many fronts are required to identify the systematic effects of different processes within the model. Climatologies of fronts can be produced from objective front identification methods based on thermal gradients ([Hewson, 1998](#); [Berry *et al.*, 2011](#)); however, at high resolution, such as used in this thesis, smoothing of the initial fields and tuning of parameters is required to avoid diagnosing noise as fronts ([Jenkner *et al.*, 2010](#)). By describing a front as a surface of constant θ_e , an objective front identification method could be used to simply find the optimal value of θ_e and the systematic effects of physical processes relative to frontal surfaces could be identified even at higher resolutions.

Bibliography

- Adamson DS, Belcher SE, Hoskins BJ, Plant RS. 2006. Boundary-layer friction in mid-latitude cyclones. *Q. J. R. Meteorol. Soc.* **132**(614): 101–124.
- Ahmadi-Givi F, Craig GC, Plant RS. 2004. The dynamics of a midlatitude cyclone with very strong latent-heat release. *Q. J. R. Meteorol. Soc.* **130**(596): 295–323.
- Ambaum MHP. 1997. Isentropic formation of the tropopause. *J. Atmos. Sci.* **54**: 555–568.
- Ambaum MHP, Novak L. 2014. A nonlinear oscillator describing storm track variability. *Q. J. R. Meteorol. Soc.* **140**(685): 2680–2684.
- Appenzeller C, Davies HC. 1992. Structure of stratospheric intrusions into the troposphere. *Nature* **358**(6387): 570–572.
- Arakawa A, Lamb VR. 1977. Computational design of the basic dynamical processes of the UCLA general circulation model. *Methods Comput. Phys.* **17**: 173–265.
- Baker LH, Martínez-Alvarado O, Methven J, Knippertz P. 2013. Flying through extratropical cyclone Friedhelm. *Weather* **68**(1): 9–13.
- Bauer P, Thorpe A, Brunet G. 2015. The quiet revolution of numerical weather prediction. *Nature* **525**(7567).
- Berry G, Reeder MJ, Jakob C. 2011. A global climatology of atmospheric fronts. *Geophys. Res. Lett.* **38**(4): 1–5.
- Birkett HR, Thorpe AJ. 1997. Superposing semi-geostrophic potential-vorticity anomalies. *Q. J. R. Meteorol. Soc.* **123**(543): 2157–2163.
- Birner T, Dörnbrack A, Schumann U. 2002. How sharp is the tropopause at midlatitudes? *Geophys. Res. Lett.* **29**(14): 44–45.

BIBLIOGRAPHY

- Bishop CH, Thorpe AJ. 1994. Potential vorticity and the electrostatics analogy: Quasi-geostrophic theory. *Q. J. R. Meteorol. Soc.* **120**(517): 713–731.
- Bjerknes J, Solberg H. 1922. *Life cycle of cyclones and the polar front theory of atmospheric circulation*. Grondahl.
- Bony S, Stevens B, Frierson DMW, Jakob C, Kageyama M, Pincus R, Shepherd TG, Sherwood SC, Siebesma AP, Sobel AH, Watanabe M, Webb MJ. 2015. Clouds, circulation and climate sensitivity. *Nat. Geosci.* **8**(4): 261–268.
- Boutle IA, Belcher SE, Plant RS. 2015. Friction in mid-latitude cyclones: an Ekman-PV mechanism. *Atmos. Sci. Lett.* **16**(2): 103–109.
- Bretherton FP. 1966a. Baroclinic instability and the short wavelength cut-off in terms of potential vorticity. *Q. J. R. Meteorol. Soc.* **92**(393): 335–345.
- Bretherton FP. 1966b. Critical layer instability in baroclinic flows. *Q. J. R. Meteorol. Soc.* **92**(393): 325–334.
- Brown AR, Beare RJ, Edwards JM, Lock AP, Keogh SJ, Milton SF, Walters DN. 2008. Upgrades to the Boundary-Layer Scheme in the Met Office Numerical Weather Prediction Model. *Boundary-Layer Meteorol.* **128**(1): 117–132.
- Browning KA. 2004. The sting at the end of the tail: Damaging winds associated with extratropical cyclones. *Q. J. R. Meteorol. Soc.* **130**(597): 375–399.
- Buizza R, Leutbecher M. 2015. The forecast skill horizon. *Q. J. R. Meteorol. Soc.* **141**(693): 3366–3382.
- Carlson TN. 1980. Airflow Through Midlatitude Cyclones and the Comma Cloud Pattern. *Mon. Weather Rev.* **108**(10): 1498–1509.
- Cau P, Methven J, Hoskins B. 2005. Representation of dry tropical layers and their origins in ERA-40 data. *J. Geophys. Res. Atmos.* **110**(D6).
- Cavallo SM, Hakim GJ. 2009. Potential Vorticity Diagnosis of a Tropopause Polar Cyclone. *Mon. Weather Rev.* **137**(4): 1358–1371.

- Chagnon JM, Gray SL. 2015. A Diabatically Generated Potential Vorticity Structure near the Extratropical Tropopause in Three Simulated Extratropical Cyclones. *Mon. Weather Rev.* **143**(6): 2337–2347.
- Chagnon JM, Gray SL, Methven J. 2013. Diabatic processes modifying potential vorticity in a north atlantic cyclone. *Q. J. R. Meteorol. Soc.* **139**(674): 1270–1282.
- Charney J. 1955. The Use of the Primitive Equations of Motion in Numerical Prediction. *Tellus* **7**(1): 22–26.
- Charney JG. 1947. The Dynamics of Long Waves in a Baroclinic Westerly Current. *J. Meteorol.* **4**(5): 136–162.
- Charney JG, Phillips NA. 1953. Numerical Integration of the Quasi-Geostrophic Equations for Barotropic and Simple Baroclinic Flows. *J. Meteorol.* **10**(2): 71–99.
- Charney JG, Stern ME. 1962. On the Stability of Internal Baroclinic Jets in a Rotating Atmosphere. *J. Atmos. Sci.* **19**(2): 159–172.
- Clark MR, Parker DJ. 2014. On the Mesoscale Structure of Surface Wind and Pressure Fields near Tornadic and Nontornadic Cold Fronts. *Mon. Weather Rev.* **142**(10): 3560–3585.
- Clayton AM, Lorenc AC, Barker DM. 2013. Operational implementation of a hybrid ensemble/4D-Var global data assimilation system at the Met Office. *Q. J. R. Meteorol. Soc.* **139**(675): 1445–1461.
- Cooper IM, Thorpe AJ, Bishop CH. 1992. The role of diffusive effects on potential vorticity in fronts. *Q. J. R. Meteorol. Soc.* **118**: 629–647.
- Coronel B, Ricard D, Rivière G, Arbogast P. 2015. Role of Moist Processes in the Tracks of Idealized Midlatitude Surface Cyclones. *J. Atmos. Sci.* **72**(8): 2979–2996.
- Davies HC, Rossa AM. 1998. PV Frontogenesis and Upper-Tropospheric Fronts. *Mon. Weather Rev.* **126**(6): 1528–1539.
- Davies LA, Brown AR. 2001. Assessment of which scales of orography can be credibly resolved in a numerical model. *Q. J. R. Meteorol. Soc.* **127**(574): 1225–1237.

BIBLIOGRAPHY

- Davies T. 2014. Lateral boundary conditions for limited area models. *Q. J. R. Meteorol. Soc.* **140**: 185–196.
- Davies T, Cullen MJP, Malcolm AJ, Mawson MH, Staniforth A, White AA, Wood N. 2005. A new dynamical core for the Met Office’s global and regional modelling of the atmosphere. *Q. J. R. Meteorol. Soc.* **131**(608): 1759–1782.
- Davis CA, Emanuel KA. 1991. Potential Vorticity Diagnostics of Cyclogenesis. *Mon. Weather Rev.* **119**(8): 1929–1953.
- Davis CA, Stoelinga MT, Kuo YH. 1993. The Integrated Effect of Condensation in Numerical Simulations of Extratropical Cyclogenesis. *Mon. Weather Rev.* **121**(8): 2309–2330.
- Dearden C, Connolly PJ, Lloyd G, Crosier J, Bower KN, Choularton TW, Vaughan G. 2014. Diabatic heating and cooling rates derived from in-situ microphysics measurements: A case study of a wintertime UK cold front. *Mon. Weather Rev.* **142**(9): 3100–3125.
- Dee DP, Uppala SM, Simmons AJ, Berrisford P, Poli P, Kobayashi S, Andrae U, Balmaseda MA, Balsamo G, Bauer P, Bechtold P, Beljaars ACM, van de Berg L, Bidlot J, Bormann N, Delsol C, Dragani R, Fuentes M, Geer AJ, Haimberger L, Healy SB, Hersbach H, Hólm EV, Isaksen L, Kållberg P, Köhler M, Matricardi M, McNally AP, Monge-Sanz BM, Morcrette JJ, Park BK, Peubey C, de Rosnay P, Tavolato C, Thépaut JN, Vitart F. 2011. The ERA-Interim reanalysis: configuration and performance of the data assimilation system. *Q. J. R. Meteorol. Soc.* **137**(656): 553–597.
- Deveson ACL, Browning KA, Hewson TD. 2002. A classification of FASTEX cyclones using a height-attributable quasi-geostrophic vertical-motion diagnostic. *Q. J. R. Meteorol. Soc.* **128**(579): 93–117.
- Diamantakis M, Davies T, Wood N. 2007. An iterative time-stepping scheme for the Met Office’s semi-implicit semi-Lagrangian non-hydrostatic model. *Q. J. R. Meteorol. Soc.* **133**(625): 997–1011.
- Durran DR, Gingrich M. 2014. Atmospheric Predictability: Why Butterflies Are Not of Practical Importance. *J. Atmos. Sci.* **71**(7): 2476–2488.

- Dyroff C, Zahn A, Christner E, Forbes R, Tompkins AM, van Velthoven PFJ. 2015. Comparison of ECMWF analysis and forecast humidity data with CARIBIC upper troposphere and lower stratosphere observations. *Q. J. R. Meteorol. Soc.* **141**(688): 833–844.
- Eady ET. 1949. Long Waves and Cyclone Waves. *Tellus A* **1**(3): 33–52.
- Edwards JM, Slingo A. 1995. Studies with a flexible new radiation code. I: Choosing a configuration for a large-scale model. *Q. J. R. Meteorol. Soc.* **122**(531): 689–719.
- Ertel H. 1942. Ein neuer hydrodynamischer Wirbelsatz. *Meteorol. Zeitschrift* **59**: 277 – 281.
- Ferreira AP, Castanheira JM, Gimeno L. 2016. Water vapour stratification and dynamical warming behind the sharpness of the Earth’s midlatitude tropopause. *Q. J. R. Meteorol. Soc.* **142**(695): 957–970.
- Fink AH, Pohle S, Pinto JG, Knippertz P. 2012. Diagnosing the influence of diabatic processes on the explosive deepening of extratropical cyclones. *Geophys. Res. Lett.* **39**(7).
- Forster C, Wirth V. 2000. Radiative decay of idealized stratospheric filaments in the troposphere. *J. Geophys. Res. Atmos.* **105**(D8): 10 169–10 184.
- Grams CM, Wernli H, Böttcher M, Čampa J, Corsmeier U, Jones SC, Keller JH, Lenz CJ, Wiegand L. 2011. The key role of diabatic processes in modifying the upper-tropospheric wave guide: A North Atlantic case-study. *Q. J. R. Meteorol. Soc.* **137**(661): 2174–2193.
- Grant ALM. 2001. Cloud-base fluxes in the cumulus-capped boundary layer. *Q. J. R. Meteorol. Soc.* **127**(572): 407–421.
- Gray SL. 2006. Mechanisms of midlatitude cross-tropopause transport using a potential vorticity budget approach. *J. Geophys. Res. Atmos.* **111**(17): 1–14.
- Gray SL, Dunning CM, Methven J, Masato G, Chagnon JM. 2014. Systematic model forecast error in Rossby wave structure. *Geophys. Res. Lett.* **41**(8): 2979–2987.
- Grazzini F, Vitart F. 2015. Atmospheric predictability and Rossby wave packets. *Q. J. R. Meteorol. Soc.* **141**(692): 2793–2802.

BIBLIOGRAPHY

- Green JSA, Ludlam FH, McIlveen JFR. 1966. Isentropic relative-flow analysis and the parcel theory. *Q. J. R. Meteorol. Soc.* **92**(392): 210–219.
- Gregory D, Kershaw R, Inness PM. 1997. Parametrization of momentum transport by convection. II: Tests in single-column and general circulation models. *Q. J. R. Meteorol. Soc.* **123**(541): 1153–1183.
- Gregory D, Rowntree PR. 1990. A Mass Flux Convection Scheme with Representation of Cloud Ensemble Characteristics and Stability-Dependent Closure. *Mon. Weather Rev.* **118**(7): 1483–1506.
- Harrold TW. 1973. Mechanisms influencing the distribution of precipitation within baroclinic disturbances. *Q. J. R. Meteorol. Soc.* **99**(420): 232–251.
- Hart NCG, Gray SL, Clark PA. 2015. Detection of Coherent Airstreams Using Cluster Analysis: Application to an Extratropical Cyclone. *Mon. Weather Rev.* **143**(9): 3518–3531.
- Harvey BJ, Methven J, Ambaum MHP. 2016. Rossby wave propagation on potential vorticity fronts with finite width. *J. Fluid Mech.* **794**: 775–797.
- Harvey NJ, Hogan RJ, Dacre HF. 2013. A method to diagnose boundary-layer type using Doppler lidar. *Q. J. R. Meteorol. Soc.* **139**(676): 1681–1693.
- Hawcroft M, Dacre H, Forbes R, Hodges K, Shaffrey L, Stein T. 2016. Using satellite and reanalysis data to evaluate the representation of latent heating in extratropical cyclones in a climate model. *Clim. Dyn.* : 1–24.
- Hawcroft MK, Shaffrey LC, Hodges KI, Dacre HF. 2012. How much Northern Hemisphere precipitation is associated with extratropical cyclones? *Geophys. Res. Lett.* **39**(24): L24809.
- Haynes P, Anglade J. 1997. The Vertical-Scale Cascade in Atmospheric Tracers due to Large-Scale Differential Advection. *J. Atmos. Sci.* **54**(9): 1121–1136.
- Haynes P, Scinocca J, Greenslade M. 2001. Formation and maintenance of the extratropical tropopause by baroclinic eddies. *Geophys. Res. Lett.* **28**(22): 4179–4182.

- Haynes PH, McIntyre ME. 1987. On the Evolution of Vorticity and Potential Vorticity in the Presence of Diabatic Heating and Frictional or Other Forces. *J. Atmos. Sci.* **44**(5): 828–841.
- Haynes PH, McIntyre ME. 1990. On the Conservation and Impermeability Theorems for Potential Vorticity. *J. Atmos. Sci.* **47**(16): 2021–2031.
- Heifetz E, Methven J, Hoskins BJ, Bishop CH. 2004a. The counter-propagating Rossby-wave perspective on baroclinic instability. I: Mathematical Basis. *Q. J. R. Meteorol. Soc.* **130**(596): 211–231.
- Heifetz E, Methven J, Hoskins BJ, Bishop CH. 2004b. The counter-propagating Rossby-wave perspective on baroclinic instability. II: Application to the Charney model. *Q. J. R. Meteorol. Soc.* **130**: 233–258.
- Hewson TD. 1998. Objective fronts. *Meteorol. Appl.* **5**(1): 37–65.
- Hewson TD, Titley Ha. 2010. Objective identification, typing and tracking of the complete life-cycles of cyclonic features at high spatial resolution. *Meteorol. Appl.* **17**(3): 355–381.
- Hoskins B, Berrisford P. 1988. A Potential Vorticity Perspective of the Storm of 15-16 October 1987. *Weather* **43**(3): 122–129.
- Hoskins BJ, Ambrizzi T. 1993. Rossby Wave Propagation on a Realistic Longitudinally Varying Flow. *J. Atmos. Sci.* **50**(12): 1661–1671.
- Hoskins BJ, Hodges KI. 2002. New Perspectives on the Northern Hemisphere Winter Storm Tracks. *J. Atmos. Sci.* **59**(6): 1041–1061.
- Hoskins BJ, James IN. 2014. Rotation in the atmosphere. In: *Fluid Dyn. Midlatitude Atmos.*, John Wiley & Sons, Ltd, pp. 125–148, doi:10.1002/9781118526002.ch8.
- Hoskins BJ, McIntyre ME, Robertson AW. 1985. On the use and significance of isentropic potential vorticity maps. *Q. J. R. Meteorol. Soc.* **111**(470): 877–946.
- Jenkner J, Sprenger M, Schwenk I, Schwierz C, Dierer S, Leuenberger D. 2010. Detection and climatology of fronts in a high-resolution model reanalysis over the Alps. *Meteorol. Appl.* **17**(1): 1–18.

BIBLIOGRAPHY

- Joly A, Thorpe AJ. 1990. Frontal instability generated by tropospheric potential vorticity anomalies. *Q. J. R. Meteorol. Soc.* **116**(493): 525–560.
- Jones E, Oliphant T, Peterson P, Others. 2017. SciPy: Open source scientific tools for Python. URL <http://www.scipy.org/>.
- Joos H, Wernli H. 2012. Influence of microphysical processes on the potential vorticity development in a warm conveyor belt: a case-study with the limited-area model COSMO. *Q. J. R. Meteorol. Soc.* **138**(663): 407–418.
- Kendon M, McCarthy M. 2015. The UK’s wet and stormy winter of 2013/2014. *Weather* **70**(2): 40–47.
- Klinker E, Sardeshmukh PD. 1992. The Diagnosis of Mechanical Dissipation in the Atmosphere from Large-Scale Balance Requirements. *J. Atmos. Sci.* **49**(7): 608–627.
- Kunkel D, Hoor P, Wirth V. 2014. Can inertia-gravity waves persistently alter the tropopause inversion layer? *Geophys. Res. Lett.* **41**(22): 7822–7829.
- Kunkel D, Hoor P, Wirth V. 2016. The tropopause inversion layer in baroclinic life-cycle experiments: the role of diabatic processes. *Atmos. Chem. Phys.* **16**(2): 541–560.
- Lamarque JF, Hess PG. 1994. Cross-Tropopause Mass Exchange and Potential Vorticity Budget in a Simulated Tropopause Folding. *J. Atmos. Sci.* **51**(15): 2246–2269.
- Lean HW, Clark PA, Dixon M, Roberts NM, Fitch A, Forbes R, Halliwell C. 2008. Characteristics of High-Resolution Versions of the Met Office Unified Model for Forecasting Convection over the United Kingdom. *Mon. Weather Rev.* **136**(9): 3408–3424.
- Legras B, Dritschel D. 1993. Vortex stripping and the generation of high vorticity gradients in two-dimensional flows. *Appl. Sci. Res.* **51**(1): 445–455.
- Lloyd G, Dearden C, Choularton TW, Crosier J, Bower KN. 2014. Observations of the Origin and Distribution of Ice in Cold, Warm, and Occluded Frontal Systems during the DIAMET Campaign. *Mon. Weather Rev.* **142**(11): 4230–4255.
- Lock AP. 1998. The parametrization of entrainment in cloudy boundary layers. *Q. J. R. Meteorol. Soc.* **124**(552): 2729–2753.

- Lock AP, Brown AR, Bush MR, Martin GM, Smith RNB. 2000. A New Boundary Layer Mixing Scheme. Part I: Scheme Description and Single-Column Model Tests. *Mon. Weather Rev.* **128**(9): 3187–3199.
- Lock AP, Edwards JM, Boutle IA. 2015. Unified Model Documentation Paper 024 The Parametrization of Boundary Layer Processes. Technical report.
- Lorenc AC. 1986. Analysis methods for numerical weather prediction. *Q. J. R. Meteorol. Soc.* **112**(474): 1177–1194.
- Lorenz EN. 1963. Deterministic Nonperiodic Flow. *J. Atmos. Sci.* **20**(2): 130–141.
- Lorenz EN. 1969. The predictability of a flow which possesses many scales of motion. *Tellus* **21**(3): 289–307.
- Madonna E, Wernli H, Joos H, Martius O. 2014. Warm Conveyor Belts in the ERA-Interim Dataset (1979–2010). Part I: Climatology and Potential Vorticity Evolution. *J. Clim.* **27**(1): 3–26.
- Martínez-Alvarado O, Baker LH, Gray SL, Methven J, Plant RS. 2014a. Distinguishing the Cold Conveyor Belt and Sting Jet Airstreams in an Intense Extratropical Cyclone. *J. Clim.* **142**(8): 2571–2595.
- Martínez-Alvarado O, Joos H, Chagnon JM, Boettcher M, Gray SL, Plant RS, Methven J, Wernli H. 2014b. The dichotomous structure of the warm conveyor belt. *Q. J. R. Meteorol. Soc.* **140**(683): 1809–1824.
- Martínez-Alvarado O, Plant RS. 2014. Parametrized diabatic processes in numerical simulations of an extratropical cyclone. *Q. J. R. Meteorol. Soc.* **140**(682): 1742–1755.
- Martius O, Schwierz C, Davies HC. 2010. Tropopause-Level Waveguides. *J. Atmos. Sci.* **67**(3): 866–879.
- McFarlane NA. 1987. The Effect of Orographically Excited Gravity Wave Drag on the General Circulation of the Lower Stratosphere and Troposphere. *J. Atmos. Sci.* **44**(14): 1775–1800.
- McIntyre ME, Norton Wa. 2000. Potential Vorticity Inversion on a Hemisphere. *J. Atmos. Sci.* **57**(9): 1214–1235.

BIBLIOGRAPHY

- Methven J. 2015. Potential vorticity in warm conveyor belt outflow. *Q. J. R. Meteorol. Soc.* **141**(689): 1065–1071.
- Methven J, Berrisford P. 2015. The slowly evolving background state of the atmosphere. *Q. J. R. Meteorol. Soc.* **141**(691): 2237–2258.
- Methven J, Hoskins B. 1999. The Advection of High-Resolution Tracers by Low-Resolution Winds. *J. Atmos. Sci.* **56**(18): 3262–3285.
- Methven J, Hoskins BJ, Heifetz E, Bishop CH. 2005. The counter-propagating Rossby-wave perspective on baroclinic instability. Part IV: Nonlinear life cycles. *Q. J. R. Meteorol. Soc.* **131**(608): 1425–1440.
- Mohebalhojeh AR, McIntyre ME. 2007. Local Mass Conservation and Velocity Splitting in PV-Based Balanced Models. Part I: The Hyperbalance Equations. *J. Atmos. Sci.* **64**(6): 1782–1793.
- Nastrom GD, Gage KS. 1985. A Climatology of Atmospheric Wavenumber Spectra of Wind and Temperature Observed by Commercial Aircraft. *J. Atmos. Sci.* **42**(9): 950–960.
- Nielsen-Gammon JW. 2001. A visualization of the global dynamic tropopause. *Bull. Am. Meteorol. Soc.* **82**(6): 1151–1167.
- Novak L, Ambaum MHP, Tailleux R. 2015. The Life Cycle of the North Atlantic Storm Track. *J. Atmos. Sci.* **72**(2): 821–833.
- Oruba L, Lapeyre G, Rivière G. 2013. On the Poleward Motion of Midlatitude Cyclones in a Baroclinic Meandering Jet. *J. Atmos. Sci.* **70**(8): 2629–2649.
- Palmer TN, Doblas-Reyes FJ, Weisheimer A, Rodwell MJ. 2008. Toward Seamless Prediction: Calibration of Climate Change Projections Using Seasonal Forecasts. *Bull. Am. Meteorol. Soc.* **89**(4): 459–470.
- Pelly JL, Hoskins BJ. 2003. A New Perspective on Blocking. *J. Atmos. Sci.* **60**(5): 743–755.
- Petterssen S, Smebye SJ. 1971. On the development of extratropical cyclones. *Q. J. R. Meteorol. Soc.* **97**(414): 457–482.

- Pfahl S, Schwierz C, Croci-Maspoli M, Grams CM, Wernli H. 2015. Importance of latent heat release in ascending air streams for atmospheric blocking. *Nat. Geosci.* **8**(8): 610–614.
- Pfahl S, Wernli H. 2012a. Quantifying the relevance of atmospheric blocking for co-located temperature extremes in the Northern Hemisphere on (sub-)daily time scales. *Geophys. Res. Lett.* **39**(12).
- Pfahl S, Wernli H. 2012b. Quantifying the Relevance of Cyclones for Precipitation Extremes. *J. Clim.* **25**(19): 6770–6780.
- Pilch Kedzierski R, Neef L, Matthes K. 2016. Tropopause sharpening by data assimilation. *Geophys. Res. Lett.* **43**(15): 8298–8305.
- Plant RS, Belcher SE. 2007. Numerical Simulation of Baroclinic Waves with a Parameterized Boundary Layer. *J. Atmos. Sci.* **64**(12): 4383–4399.
- Plant RS, Craig GC, Gray SL. 2003. On a threefold classification of extratropical cyclogenesis. *Q. J. R. Meteorol. Soc.* **129**(594): 2989–3012.
- Priestley MDK, Pinto JG, Dacre HF, Shaffrey LC. 2017. Rossby wave breaking, the upper level jet, and serial clustering of extratropical cyclones in western Europe. *Geophys. Res. Lett.* **44**(1): 514–521.
- Randel WJ, Wu F, Forster P. 2007. The Extratropical Tropopause Inversion Layer: Global Observations with GPS Data, and a Radiative Forcing Mechanism. *J. Atmos. Sci.* **64**(12): 4489–4496.
- Raveh-Rubin S. 2017. Dry Intrusions: Lagrangian Climatology and Dynamical Impact on the Planetary Boundary Layer. *J. Clim.* **30**(17): 6661–6682.
- Rawlins F, Ballard SP, Bovis KJ, Clayton AM, Li D, Inverarity GW, Lorenc AC, Payne TJ. 2007. The Met Office global four-dimensional variational data assimilation scheme. *Q. J. R. Meteorol. Soc.* **133**(623): 347–362.
- Reed RJ. 1955. A Study of a Characteristic Type of Upper-Level Frontogenesis. *J. Meteorol.* **12**: 226–237.
- Rex DF. 1950. Blocking Action in the Middle Troposphere and its Effect upon Regional Climate. I. An Aerological Study of Blocking Action. *Tellus* **2**(3): 196–211.

BIBLIOGRAPHY

- Riemer M, Jones SC. 2010. The downstream impact of tropical cyclones on a developing baroclinic wave in idealized scenarios of extratropical transition. *Q. J. R. Meteorol. Soc.* **136**(648): 617–637.
- Rivière G, Arbogast P, Lapeyre G, Maynard K. 2012. A potential vorticity perspective on the motion of a mid-latitude winter storm. *Geophys. Res. Lett.* **39**(12).
- Rodwell MJ, Lang STK, Ingleby NB, Bormann N, Hólm E, Rabier F, Richardson DS, Yamaguchi M. 2016. Reliability in ensemble data assimilation. *Q. J. R. Meteorol. Soc.* **142**(694): 443–454.
- Rodwell MJ, Magnusson L, Bauer P, Bechtold P, Bonavita M, Cardinali C, Diamantakis M, Earnshaw P, Garcia-Mendez A, Isaksen L, Källén E, Klocke D, Lopez P, McNally T, Persson A, Prates F, Wedi N. 2013. Characteristics of occasional poor medium-range weather forecasts for Europe. *Bull. Am. Meteorol. Soc.* **94**(9): 1393–1405.
- Rodwell MJ, Palmer TN. 2007. Using numerical weather prediction to assess climate models. *Q. J. R. Meteorol. Soc.* **133**(622): 129–146.
- Rossa MA, Wernli H, Davies CH. 2000. Growth and Decay of an Extra-Tropical Cyclone's PV-Tower. *Meteorol. Atmos. Phys.* **73**(3): 139–156.
- Rossby CG. 1940. Planetary flow patterns in the atmosphere. *Q. J. R. Meteorol. Soc.* **66**: 68–87.
- Rotunno R, Snyder C. 2008. A Generalization of Lorenz's Model for the Predictability of Flows with Many Scales of Motion. *J. Atmos. Sci.* **65**(3): 1063–1076.
- Saffin L, Methven J, Gray SL. 2016. The non-conservation of potential vorticity by a dynamical core compared with the effects of parametrized physical processes. *Q. J. R. Meteorol. Soc.* **142**(696): 1265–1275.
- Saffin L, Methven J, Gray SL, Williams KD. 2017. Maintaining tropopause sharpness in numerical weather prediction models **In Review**.
- Sanders F, Gyakum JR. 1980. Synoptic-Dynamic Climatology of the Bomb. *Mon. Weather Rev.* **108**(10): 1589–1606.

- Scaife AA, Butchart N, Warner CD, Swinbank R. 2002. Impact of a Spectral Gravity Wave Parameterization on the Stratosphere in the Met Office Unified Model. *J. Atmos. Sci.* **59**(9): 1473–1489.
- Schär C, Davies HC. 1990. An Instability of Mature Cold Fronts. *J. Atmos. Sci.* **47**(8): 929–950.
- Schemm S, Wernli H, Papritz L. 2013. Warm Conveyor Belts in Idealized Moist Baroclinic Wave Simulations. *J. Atmos. Sci.* **70**(2): 627–652.
- Schultz DM, Vaughan G. 2010. Occluded Fronts and the Occlusion Process: A Fresh Look at Conventional Wisdom. *Bull. Am. Meteorol. Soc.* **92**(4): 443–466.
- Schwierz C, Dirren S, Davies HC. 2004. Forced Waves on a Zonally Aligned Jet Stream. *J. Atmos. Sci.* **61**(1): 73–87.
- Shapiro MA, Keyser D. 1990. Fronts, Jet Streams and the Tropopause. *Extratropical Cyclones Erik Palmen Meml. Vol.* : 167–189.
- Sinclair VA, Gray SL, Belcher SE. 2008. Boundary-layer ventilation by baroclinic life cycles. *Q. J. R. Meteorol. Soc.* **134**(635): 1409–1424.
- Smith RNB. 1990. A scheme for predicting layer clouds and their water content in a general circulation model. *Q. J. R. Meteorol. Soc.* **116**(492): 435–460.
- Son SW, Polvani LM. 2007. Dynamical formation of an extra-tropical tropopause inversion layer in a relatively simple general circulation model. *Geophys. Res. Lett.* **34**(17).
- Sprenger M, Wernli H. 2015. The Lagrangian analysis tool LAGRANTO version 2.0. *Geosci. Model Dev.* **8**: 1893–1943.
- Stoelinga MT. 1996. A Potential Vorticity-Based Study of the Role of Diabatic Heating and Friction in a Numerically Simulated Baroclinic Cyclone. *Mon. Weather Rev.* **124**(5): 849–874.
- Stratton RA, Willett MR, Derbyshire S, Wong R, Whithall M. 2015. Unified Model Documentation Paper 027 Convection Schemes .
- Tamarin T, Kaspi Y. 2016. The Poleward Motion of Extratropical Cyclones from a Potential Vorticity Tendency Analysis. *J. Atmos. Sci.* **73**(4): 1687–1707.

BIBLIOGRAPHY

- Thorncroft CD, Hoskins BJ, McIntyre ME. 1993. Two paradigms of baroclinic-wave life-cycle behaviour. *Q. J. R. Meteorol. Soc.* **119**(509): 17–55.
- Thorpe AJ, Bishop CH. 1995. Potential vorticity and the electrostatics analogy: Ertel–Rossby formulation. *Q. J. R. Meteorol. Soc.* **121**(1964): 1477–1495.
- Thuburn J. 2008. Some conservation issues for the dynamical cores of NWP and climate models. *J. Comput. Phys.* **227**(7): 3715–3730.
- Tibaldi S, Molteni F. 1990. On the operational predictability of blocking. *Tellus A* **42**(3): 343–365.
- Valdes PJ, Hoskins BJ. 1988. Baroclinic Instability of the Zonally Averaged Flow with Boundary Layer Damping. *J. Atmos. Sci.* **45**(10): 1584–1593.
- Vallis GK. 1996. Potential vorticity inversion and balanced equations of motion for rotating and stratified flows. *Q. J. R. Meteorol. Soc.* **122**: 291–322.
- Vallis GK. 2006. *Atmospheric and Oceanic Fluid Dynamics*. Cambridge University Press, 8 edn, ISBN 978-0-521-84969-2.
- Vannière B, Czaja A, Dacre H, Woollings T, Parfitt R. 2016. A potential vorticity signature for the cold sector of winter extratropical cyclones. *Q. J. R. Meteorol. Soc.* **142**(694): 432–442.
- Vaughan G, Methven J, Anderson D, Antonescu B, Baker LH, Baker TP, Ballard SP, Bower KN, Brown PRA, Chagnon JM, Choularton TW, Chylik J, Connolly PJ, Cook PA, Cotton RJ, Crosier J, Dearden C, Dorsey JR, Frame THA, Gallagher MW, Goodliff M, Gray SL, Harvey BJ, Knippertz P, Lean HW, Li D, Lloyd G, Martínez-Alvarado O, Nicol J, Norris J, Öström E, Owen J, Parker DJ, Plant RS, Renfrew IA, Roberts NM, Rosenberg P, Rudd AC, Schultz DM, Taylor JP, Trzeciak T, Tubbs R, Vance AK, van Leeuwen PJ, Wellpott A, Woolley A. 2015. Cloud Banding and Winds in Intense European Cyclones: Results from the DIAMET Project. *Bull. Am. Meteorol. Soc.* **96**(2): 249–265.
- Visram AR, Cotter CJ, Cullen MJP. 2014. A framework for evaluating model error using asymptotic convergence in the Eady model. *Q. J. R. Meteorol. Soc.* **140**(682): 1629–1639.

- Walters DN, Best MJ, Bushell AC, Copsey D, Edwards JM, Falloon PD, Harris CM, Lock AP, Manners JC, Morcrette CJ, Roberts MJ, Stratton RA, Webster S, Wilkinson JM, Willett MR, Boutle IA, Earnshaw PD, Hill PG, MacLachlan C, Martin GM, Moufouma-Okia W, Palmer MD, Petch JC, Rooney GG, Scaife AA, Williams KD. 2011. The Met Office Unified Model Global Atmosphere 3.0/3.1 and JULES Global Land 3.0/3.1 configurations. *Geosci. Model Dev.* **4**(4): 919–941.
- Wang SM, Geller MA. 2016. Baroclinic mixing of potential vorticity as the principal sharpening mechanism for the extratropical Tropopause Inversion Layer. *Earth Sp. Sci.* **3**(9): 362–369.
- Warner CD, McIntyre ME. 1996. On the Propagation and Dissipation of Gravity Wave Spectra through a Realistic Middle Atmosphere. *J. Atmos. Sci.* **53**(22): 3213–3235.
- Warner CD, McIntyre ME. 1999. Toward an ultra-simple spectral gravity wave parameterization for general circulation models. *Earth, Planets Sp.* **51**(7-8): 475–484.
- Webster S, Brown AR, Cameron DR, PJones C. 2003. Improvements to the representation of orography in the Met Office Unified Model. *Q. J. R. Meteorol. Soc.* **129**(591): 1989–2010.
- Wernli H, Davies HC. 1997. A lagrangian-based analysis of extratropical cyclones. I: The method and some applications. *Q. J. R. Meteorol. Soc.* **123**(538): 467–489.
- White AA, Hoskins BJ, Roulstone I, Staniforth A. 2005. Consistent approximate models of the global atmosphere: shallow, deep, hydrostatic, quasi-hydrostatic and non-hydrostatic. *Q. J. R. Meteorol. Soc.* **131**(609): 2081–2107.
- Whitehead JP, Jablonowski C, Kent J, Rood RB. 2015. Potential vorticity: Measuring consistency between GCM dynamical cores and tracer advection schemes. *Q. J. R. Meteorol. Soc.* **141**(688): 739–751.
- Wilcox LJ, Hoskins BJ, Shine KP. 2012. A global blended tropopause based on ERA data. Part I: Climatology. *Q. J. R. Meteorol. Soc.* **138**(664): 561–575.
- Wilson DR, Ballard SP. 1999. A microphysically based precipitation scheme for the UK meteorological office unified model. *Q. J. R. Meteorol. Soc.* **125**(557): 1607–1636.

BIBLIOGRAPHY

- Wirth V. 2001. Cyclone-Anticyclone Asymmetry Concerning the Height of the Thermal and the Dynamical Tropopause. *J. Atmos. Sci.* **58**(1): 26–37.
- Wood N, Staniforth A, White A, Allen T, Diamantakis M, Gross M, Melvin T, Smith C, Vosper S, Zerroukat M, Thuburn J. 2014. An inherently mass-conserving semi-implicit semi-Lagrangian discretization of the deep-atmosphere global non-hydrostatic equations. *Q. J. R. Meteorol. Soc.* **140**(682): 1505–1520.
- Young MV, Monk GA, Browning KA. 1987. Interpretation of satellite imagery of a rapidly deepening cyclone. *Q. J. R. Meteorol. Soc.* **113**(478): 1089–1115.
- Zhang K, Wan H, Wang B, Zhang M. 2008. Consistency problem with tracer advection in the Atmospheric Model GAMIL. *Adv. Atmos. Sci.* **25**(2): 306–318.